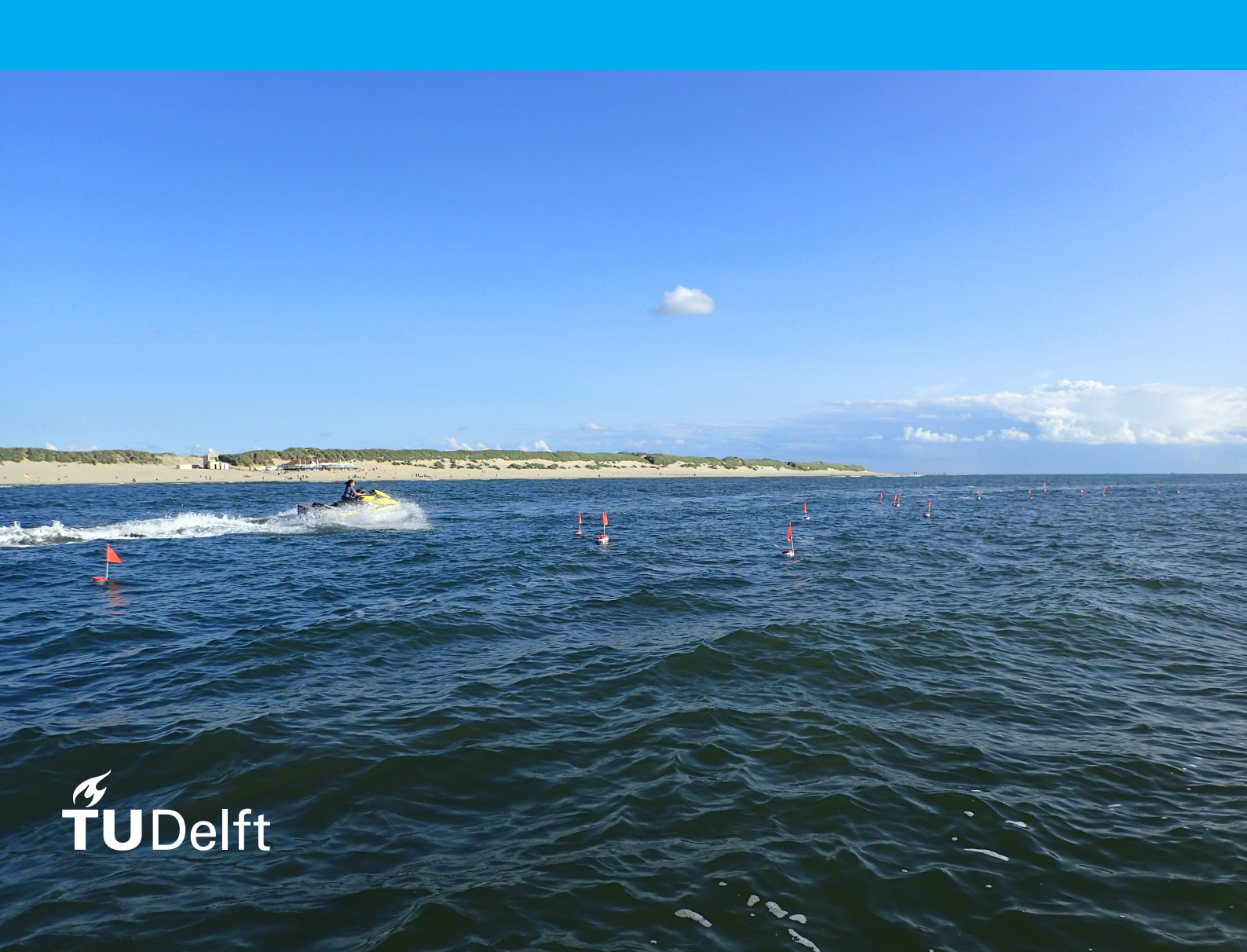
## **Master Thesis**

# The effects of currents on wave nonlinearities

M.J.P. van de Ven



## Master Thesis

## The effects of currents on wave nonlinearities

by

M.J.P. van de Ven

to obtain the degree of Master of Science at the Delft University of Technology, to be defended publicly on Tuesday July 10, 2018 at 10:00 AM.

Student number: 4063201

Project duration: July 10, 2017 – July 10, 2018

Thesis committee: Prof. dr. ir. A. J. H. M. Reniers TU Delft

Dr. Ir. M. F. S. Tissier TU Delft, chair

Dr. Ir. M. A. de Schipper TU Delft Ir. F. P. de Wit TU Delft

An electronic version of this thesis is available at http://repository.tudelft.nl/.



### **Abstract**

This study investigates nonlinear wave shape and the near-bed velocity influenced in the vicinity of a tidal inlet for the SEdiment supply At the WAdden Sea ebb-tidal Delta project. Wave nonlinearities occur when waves encounter a flow. An opposing flow leads to waves with higher peaks and reduced wave length. During a following flow, the waves tend to flatten and the wave length increases. High peak and flat troughs is a condition referred to as wave skewness. Wave asymmetry entails a pitched forward wave shape, with a steep front face and a gentle rear face. These wave nonlinearities contribute to sediment transport. Literature shows that skewness and asymmetry are widely studied in the nearshore zone. However, nonlinearities in deeper water and under influence of flow are not well understood. The goal of the present study is to determine whether a flow contributes to higher wave non-linearities in the ebb-tidal delta northwest of Ameland.

The study uses data collected during the SEAWAD field campaign. Over the course of 42 days, five frames and eight pressure sensors were deployed in the ebb-tidal delta northwest of Ameland. The analysis examines data from Acoustic Doppler Velocimeter (ADV) and Acoustic Doppler Current Profiler (ADCP) on frames in 5 m and 8 m water depth, and pressure sensors located around the frames.

The results consists of three parts; 1) a general overview of the surface elevation skewness and velocity skewness over the measured period; 2) the correlation between the sea-surface elevation skewness and the near-bed velocity non-linearities; and 3) the contribution of a flow to the sea surface elevation non-linearities and near-bed velocity nonlinearities.

Findings show that wave nonlinearities occur in the vicinity of an ebb-tidal delta. The variations in the velocity skewness seem to vary with the tide. Only the driving mechanism behind this variation is not clear. The wave asymmetry shows little variation over each tidal cycle. Larger significant wave height and peak period contributes to higher skewness and higher asymmetry. Second, there is a significant correlation between the sea-surface elevation skewness and the near-bed velocity skewness. The observed correlation increases with an increasing wave period. Wave skewness is affect by a flow. In a following flow, the sea surface elevation skewness values are larger than in an opposing flow for the same Ursell number. The velocity skewness shows the same behavior, only this trend is less distinct.

## **Preface**

This thesis is written in completion of the Master Hydraulic Engineering of the faculty Civil Engineering and Geosciences at Delft University of Technology.

I would like to thank my committee their enthusiasm, input and fruitful discussions throughout my research. In particular, Marion Tissier and Floris de Wit for the opportunity to let me join the SEAWAD field campaign, which was definitely the highlight of my studies. Moreover, the daily input and great knowledge about waves by Marion was inspiring. Thanks to Floris for the all the effort and his sharp comments during the research. I also would like to thank Matthieu de Schipper for his always honest and constructive comments. Furthermore, I would like to thank Ad Reniers for his valuable feedback and interesting suggestions on my research. Lastly, I want express my gratitude to my parents for their unconditional support throughout my studies.

M.J.P. van de Ven Delft, June 2018

## Nomenclature

#### **List of Abbreviations**

**ADCP** Acoustic Doppler Current Profiler

**ADV** Acoustic Doppler Velocimeter

**ECEF** Earth-Centered Earth-Fixed

ENU East, North, UP

NAP Nieuw Amsterdams Peil

SEAWAD SEdiment supply At the WAdden Sea ebb-tidal Delta

SNR Signal to Noise Ratio

#### **List of Symbols**

 $\beta_c$  velocity leaning index

 $\hat{p}_{wave}$  wave induced pressure correction

 $\hat{u}_0$  orbital velocity

μ shallowness parameter

 $\omega$  wave frequency in stationary frame of reference

 $\phi$  wave form parameter

Ψ phase

 $\sigma$  dimensionless steepness

 $\sigma$  wave frequency in moving frame of reference

 $\zeta_H$  hydrostatic surface elevation

 $As_{\eta}$  sea surface elevation asymmetry

 $As_u$  velocity asymmetry

B dimensionless nonlinearity

c wave speed

 $c_0$  deep water wave speed

viii Preface

$c_g$	group celerity
E	wave energy per unit horizontal area
f	dimensionless factor of the skewness index
g	gravitational acceleration
h	water depth
$H_s$	significant wave height
K	attenuation correction factor
k	wave number
$K_H$	transformation ratio of the mean wave height under influence of a non-uniform current
L	wave length
$p_{wave}$	wave induced pressure
r	skewness index
$R_a$	acceleration skewness coefficient
$R_u$	velocity skewness coefficient
$S_{\eta\eta}(\omega)$	) spectral density function in case of zero current
$S_{ER}$	spectral equilibrium range
$S_s$	wave steepness
$S_{uu}$	spectral density under influence of a current
$S_x$	radiation stress
$Sk_{\eta}$	sea surface elevation skewness
$Sk_u$	velocity skewness
T	significant wave period
$T_c$	zero-crossing period
$T_{z}$	intrinsic period
U	uniform current velocity
$U_n$	current in the wave direction
$U_r$	Ursell number
$U_w$	velocity amplitude

## Contents

1	Intro	duction	1
	1.1	Background Information	
	1.2	Research Question	2
	1.3	Research Approach	2
	1.4	Report Structure	2
_	1 !4	Davies.	_
2		rature Review	3
	2.1	Effect of Currents on Waves	
	2.2	Effect of Waves on Currents	
	2.3	Wave Pressure to Sea Surface Elevation	
		2.3.1 Linear wave theory	
		2.3.2 Nonlinear Wave Theory	7
	2.4	Wave Shape Characterization and Parameterization	7
		2.4.1 Characterization of waves	7
		2.4.2 Parameterization of the wave shape	
	2.5	Velocity under Waves	
		2.5.1 Free-stream velocity	
		2.5.2 Wave bottom boundary velocity	
	2.6	Change of Wave Spectra in Presence of Current	
	2.0	Change of wave Spectra in Presence of Current	
3	Field	d Experiment 1	3
	3.1	Field Site	3
	3.2	Instruments and Settings	4
		3.2.1 Frames and instruments	
		3.2.2 Setting Instruments	
	3.3	Environmental Conditions	
	0.0	3.3.1 Wind	
		3.3.2 Waves	
		3.3.3 Tides	
		3.3.4 Currents	1
4	Data	Processing 1	9
	4.1	Pressure Correction	9
		4.1.1 Air pressure correction	
		4.1.2 Pressure attenuation	
	4.2	Velocity Signal Correction	
	4.2		
		4.2.1 Correlation, noise and Spikes	
	4.0	4.2.2 Orientation to ENU	
		Wave Spectra	
	4.4	Currents	
	4.5	Conclusion	2
5	Way	e Nonlinearity on Ebb Tidal Shoal	23
•	5.1	Overview	
	5.2	Sea Surface Elevation Skewness and Asymmetry	
	5.3	Velocity Skewness and Asymmetry	
	5.4	Correlation Sea Surface Elevation and Velocity Skewness	
	5.5		
		5.5.1 Directional spreading on wave skewness	
		5.5.2 Currents on wave skewness	5
		5.5.3 Local wave parameters on wave skewness	39

<u>X</u> Contents

6	6.1	Link to Literature	41 42 42 43 45
7	7.1	Conclusions & Recommendations  Conclusion	47 47 48 48
Lis	t of	Figures	49
Lis	t of	Tables	53
	ferer		55
A			59
<b>A</b>		Linear Wave Theory	59
В		Coordinates frames and pressure sensors	63
С		Correlation	
D	D.2 D.3	Linear reconstruction of the surface elevation  Non-linear reconstruction of the surface elevation  D.2.1 Influence on the wave spectra  D.2.2 Influence on skewness and asymmetry  Influence of current on wave spectra  Conclusion	74 74 75 77
E	E.3 E.4 E.5 E.6 E.7	Overall results	82 84 84 85 87

1

## Introduction

This chapter presents background information and explains why the project was carried out. A basic explanation of nonlinear wave shape in the vicinity of a tidal inlet is presented. Furthermore, the research question and research goal are given. Finally, the structure of the report is described.

#### 1.1. Background Information

The Dutch coast is a flood-prone zone that is affected by wind, waves and currents. Those wind, waves and currents are causing a retreat of the coastline. In order to mitigate further retreat of the coastline, soft solutions such as nourishments are applied. The goal of nourishment is to keep sediment volumes the same or even increase them. A reduction of the sediment volume in the ebb-tidal delta and north side of the Wadden Islands is noted. This reduction is caused by the export of sediment into the Wadden Sea basin. With upcoming challenges like sea level rise and land subsidence, nourishment is needed to maintain the ebb-tidal delta and the north side coast of the Wadden Islands.

The ebb-tidal delta of the Wadden Sea area is subject to different factors that influence the sediment budget. On the one hand, waves generated on the North Sea cause an increase in sediment stirring. On the other hand, tidal currents transport the sediments to the area. The combination of these two factors contribute to the sediment budget in the Wadden Sea area.

In the case of the Ameland inlet, there is a phase lag between water levels on the Wadden Sea and North Sea. This causes an ebb or flood flow on the ebb-tidal delta. The Wadden Sea estuary fills during flood and empties during ebb at the North Sea. During ebb on the North Sea, this results in a strong flow directed outward from the estuary. The reverse occurs during flood flow.

When the strong outward flow occurs in combination with high waves from the North Sea, there is an interaction between the tidal flow and waves. This interaction has several consequences on the wave transformation and sediment transport. The flows affects wave shape. During a following flow, waves tend to flatten, with lower heights and longer troughs, while in case of an opposing flow, waves tend to steepen. The deforming wave shape causes changes in the near-bed velocities. This ultimately contributes to the sediment transport in the ebb-tidal delta.

This report explains the results of the SEAWAD field experiments. The SEAWAD project aims to gain insight into the morphological and ecological behavior of a mega-nourishment near the Wadden Sea area. In order to apply a nourishment, it is crucial to understand the interaction between the tidal flow and waves. In this thesis, the hydrodynamical aspects of the wave and tidal flow are examined.

2 1. Introduction

#### 1.2. Research Question

As discussed in Section 1.1 the hydrodynamical interaction between waves and currents is of importance for the sediment transport in an ebb-tidal area. The aim of this project is to analyze how a tidal flow influences the nonlinear wave shape and therefore the corresponding near-bed velocity.

This gives the following research question:

## How is the nonlinear wave shape influenced in the vicinity of the Ameland tidal inlet?

The research question contains the following subquestions:

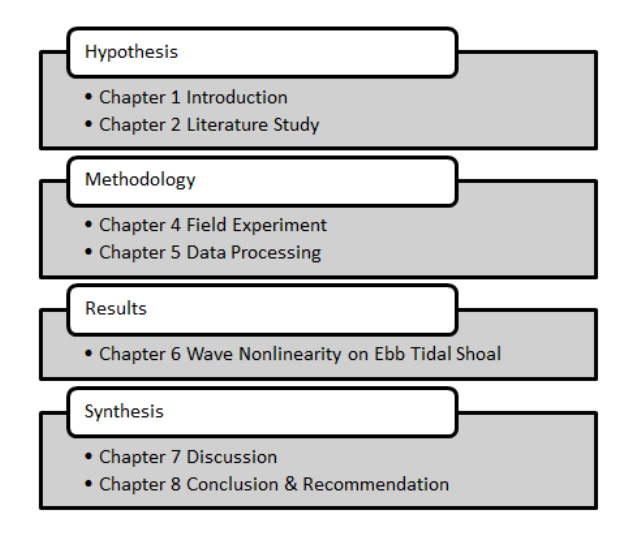
- Are wave nonlinearities influenced by the tidal flow on an ebb-tidal shoal?
- What is the correlation between sea surface elevation skewness and velocity skewness in the presence of a tidal flow?
- What is the relationship between skewness and asymmetry with respect to the Ursell number in the case of tidal flow?

#### 1.3. Research Approach

To answer these questions, we analyzed the hydrodynamic data gathered during the SEAWAD field campaign. These measurements are taken with pressure sensors, the Acoustic Doppler Velocimeter (ADV) the Acoustic Doppler Current Profiler (ADCP) and AquadoppHR. To reduce the scope, this research focuses only on wave shape that could influence sediment transport.

#### 1.4. Report Structure

This report presents the results of the analysis of the wave nonlinearities with the data obtained during the SEAWAD field campaign. The outline of the report is as follows.



Chapter 2 contains a literature review of the wave-current interaction. A description of the fieldwork is given in Chapter 3. The data processing is discussed in Chapter 4. Chapter 5 shows the results of the wave nonlinearity on ebb-tidal delta. These results will be further discussed in Chapter 6. Finally, the conclusion and recommendations are given in Chapter 7.

## Literature Review

In this chapter, the theoretical background of the wave-current interaction is discussed.

In seas, different types of currents can occur, such as tidal currents, major ocean currents, currents related to wind action, currents generated by waves, and internal waves. In this literature review, only tidal currents are discussed. Tidal currents in the direction of the waves are called following or positive currents, while currents in the opposing direction of the waves are called opposing or negative currents.

#### 2.1. Effect of Currents on Waves

In an environment such as a coastal area, energy is generated by tides, surges, and wind waves. Changes in surges, tides, and mean water depth affect the wind waves. Tides and surges can be seen as long waves with periods of several hours. Short wind waves, however, have a period of several several seconds (Wolf, 1999). The wave-current interaction influences the wave kinematics and wave dynamics. Wave kinematics refers to changes in frequency and wave number due to shoaling and refraction in the absence of a source and sink. Wave dynamics refers to changes in wave height, the wave action conservation, and the effect of wind input and dissipation.

How the wave kinematics and wave dynamics are influenced by currents is described through a number of mechanisms. The different mechanisms are:

• **Current-induced refraction**, or the change of wave direction due to a following or opposing tidal flow. This phenomenon is the same as depth-induced refraction, as the wave rays propagate toward the area with lower speed. The rate of direction change due to the depth and current-induced refraction is:

$$c_{\theta,ref,depth+current} = -\frac{c_g}{c} \frac{\partial c}{\partial m} - \frac{\partial U_n}{\partial m}$$
 (2.1)

The first term represents the depth-induced refraction, dependent on  $c_g$  [m/s] group wave speed and the wave speed c, and the second term the current-induced refraction, dependent on  $U_n$ , the current in the wave direction (Holthuijsen, 2007).

• **Amplitude change**, for an opposing current, the amplitude of a wave will increase, but for a following current, the wave shape tends to flatten. To give a measure of the amplitude change of waves under influence of a current, Longuet-Higgins (1961) assumed, with linear wave theory, that the effect of the current variation on the wave energy is caused by the rate of strain against the radiation stress, as shown in Equation 2.2.

$$\frac{\partial}{\partial x}[E(c_g + U)] + S_x \frac{\partial U}{\partial x} = 0$$
 (2.2)

4 2. Literature Review

In this equation, E is the wave energy per unit horizontal area,  $S_x$  the radiation stress and  $c_a$  the group velocity of the waves.

This results in the amplification factor of the wave, shown in Equation 2.3.

$$\frac{a}{a_0} = \left[ \frac{c_0(c_0 + 2U_0)}{c(c + 2U)} \right]^{\frac{1}{2}}$$
 (2.3)

Here  $c_0$  is the deep water no-current wave speed, and c the wave speed relative to the current. The uniform current velocity is denoted by U. The values for a case with U=0 are  $a_0$  and  $c_0$ . This relation is described by the line in Figure 2.1. At the critical point  $-0.5c_g=U$  the amplification factor goes to infinity. This means that after this point, waves tend to break and linear wave theory is no longer applicable.

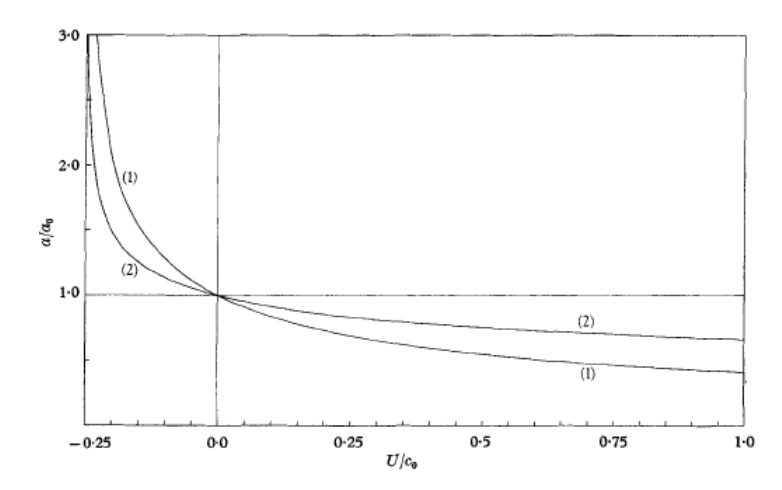


Figure 2.1: Wave-current amplification factor  $a/a_0$  the wave height compared to the deep-water wave height as a function of U in the direction of the wave propagation. Case (1) is with vertical upwelling from below, Case (2) is with horizontal inflow from the sides. Longuet-Higgins and Stewart (1961)

#### · Doppler shift

Consider a two dimensional wave moving on a depth-uniform current. The moving frame of reference is the current. The equation and solution for surface gravity waves are identical to a case without current, so linear wave theory can be applied. Consider  $\omega$  the wave frequency in a stationary frame of reference, and  $\sigma$  as the wave frequency in the moving frame of reference. Using these, the phase speed of the wave in the moving frame of reference can be related to the phase speed in a stationary frame of reference, as presented in Equation 2.4 (Chawla & Kirby, 1998).

$$\frac{\omega}{k} = \frac{\sigma}{k} + U \quad or \quad \omega - kU = \sigma \tag{2.4}$$

Here, k and U are respectively the wavenumber and the current speed. The intrinsic frequency  $\sigma$  depends on the linear wave theory, as described in Appendix A, used to obtain the dispersion relationship, as shown in Equation 2.5.

$$\sigma^2 = gk \tanh(kh) \tag{2.5}$$

The influence of shear current on dispersion relations is explained. As the shape of the sheared flow influences dispersion relations. The assumptions for this theory, developed by Kirby and Chen (1989), are that there is a weak current, so  $|U(z)|/c \ll 1$ , and linear waves. This gives a solution for arbitrary velocity profile as follows:

$$\tilde{U} = \frac{2k}{\sinh(2kh)} \int_{-h}^{0} U(z) \cosh(2k(h+z)) dz$$
 (2.6)

From this equation can be seen that if the depth goes from 0 to infinity the expression changes to that, shown in Equation 2.7. If  $kh > \infty$  Equation 2.7 states that the weighted depth-averaged velocity decreases exponentially with the depth. This agrees with the theory that the influence of waves on a current beneath L/2 is minimal.

$$\tilde{U} = 2k \int_{-\infty}^{0} U(z)e^{2kz}dz \tag{2.7}$$

• **Modulation of absolute frequency**. Waves in water bodies with a constant depth and current keep their relative frequency. However, if the depth or current changes, the frequency will vary as well. The rate of frequency change can be denoted as  $d\sigma/dt = c_{\sigma}$ , in a moving frame of reference with the energy moving along the wave ray, (Holthuijsen, 2007), is given by Equation 2.8.

$$\frac{d\sigma}{dt} = c_{\sigma} = \frac{\partial\sigma}{\partial h} \left( \frac{\partial h}{\partial t} + U \frac{\partial d}{\partial t} \right) - c_{g} k \frac{\partial U_{n}}{\partial n}$$
 (2.8)

The first term on the left side of the equation is the frequency change. The first term on the right is the depth variation in time. The term in the brackets is the effect of the current bodily moving the wave across a horizontally varying bottom. The second term on the right side represents the effect of the wave moving with a horizontally varying current. The corresponding variation in absolute frequency  $\omega$  and wave number k follow directly from the variation in relative frequency  $\sigma$  (Holthuijsen, 2007)

• **Wave steepening** Waves on an opposing current tend to steepen, with a shorter wave length and increase in wave height, due to wave action conservation, as described in Appendix A. The steepness of a wave is determined by the wave height  $H_s$  divided by the wave length L (Wolf & Prandle, 1999).

$$S_s = \frac{2\pi H_s}{gT_z^2} \tag{2.9}$$

The steepness is determined by the significant wave height  $H_s$  and the intrinsic period  $T_z$ . To determine the steepness of the waves, the intrinsic frequency is used. These frequencies are directly related to the wavelength. Parameterization of the steepening of waves is discussed in Section 2.4.

• **Wave-current bottom shear stress**, The friction experienced by waves in a wave-current regime is higher than in a non-current regime. Modification of the bed shear can lead to appreciable changes in the current strength or the gradient of mean water surface (Wolf & Prandle, 1999).

#### 2.2. Effect of Waves on Currents

The effect of waves on currents can be described by the following mechanisms:

- **Radiation stress:**, as described in Appendix A, is indicated as the wave-induced momentum. In the surf zone this momentum generates a set-up and an alongshore current. For completeness this factor is added here, but the wave-current interaction occurs far outside the surf zone.
- **Bottom friction coefficient for currents**. Waves cause an oscillatory wave bottom boundary. This is a relatively thin layer near the seabed, that induces shear stress and intensifies turbulence due to the combined effect of both waves and currents. The relation between shear stresses and turbulence due to waves and currents are non-linearly coupled. As a result, the shear stresses generated by either waves or currents

6 2. Literature Review

are different from the shear stresses induced by the wave-current interaction. Therefore, the current in the region above the wave bottom boundary layer not only experiences a shear stress due to the bottom roughness but also due to the wave bottom boundary layer (Grant & Madsen, 1979).

#### 2.3. Wave Pressure to Sea Surface Elevation

In the SEAWAD field campaign, there are no direct measurements of the sea surface elevation. Instead, these measurements are taken by means of pressure sensors. Since the wave shape is important, a precise reconstruction of the sea surface elevation in necessary. The bottom pressure to sea surface elevation has been done with several methods. In this section the widely used linear wave theory is explained. Furthermore a non-linear method for the reproduction of the sea surface elevation is elaborated on.

#### 2.3.1. Linear wave theory

The linear wave theory of gravity waves, also known as the Airy wave theory, considers water with idealized physical properties and motions, namely gravitational force is the only external force on the water. Linear wave theory is based on the mass and momentum balance, as explained in Appendix A. The Laplace and Bernoulli equations are obtained from the rewritten mass and momentum balance in terms of the velocity potential function. With the kinematic boundary conditions at the surface and bottom, as shown in Equation A.6, one of the solutions of the Laplace equation is the long-crested harmonic wave propagation. From this solution, the wave-induced particle motions, -the particle velocity and particle path-, are derived. The dynamic boundary conditions of the atmospheric pressure at the water surface, gives a relationship between the radian frequency  $\omega$  and the wavenumber k. This relationship is called the dispersion relationship, as shown in Equation 2.10. The propagation speed of the surface wave is obtained from the dispersion relationship, as shown in Equation 2.11

$$\omega^2 = gk \tanh(kd) \tag{2.10}$$

$$c = \frac{g}{\omega} \tanh(kd) \tag{2.11}$$

The linearized Bernoulli equation gives, in combination with the Laplace results, an expression of the wave-induced pressure in the water beneath the wave. The circular or elliptical motion of the water particles implies that there is an acceleration. This acceleration can only be caused by an force. These forces are the contribution of the gradient in the wave-induced pressure. The total pressure in the water column is described as:

$$p = -\rho gz + p_{wave} \tag{2.12}$$

In Equation 2.12  $p_{wave}$  corresponds to the wave-induced pressure. The wave induced pressure consists of correction factor K, and a sine function as shown in Equation 2.13. The pressure distribution provides a vertical acceleration beneath the crest and through. A horizontal acceleration is present in the zero-crossings of the water surface. Wave orbital motions are explained in Section 2.5.

$$p_{wave} = \rho g K a \sin(\omega t - kx) \quad with \quad K = \frac{\cosh[k(d+z)]}{\cosh(kz)}$$
 (2.13)

Linear wave theory is the basis for the transformation of the pressure measured to the surface elevation. The dynamic part of the pressure  $p_{wave}$  is decomposed by using the Fourier analyses. As shown in Equation 2.13, each pressure component is corrected with the pressure response function K. The time series surface elevation is obtained with an inverse fast Fourier transform.

A limitation of pressure measurements is that high frequency pressure signals are weak due to depth attenuation. This drawback is overcome with the pressure response function K, which increases with the frequency. However this function can also amplify noise (Lee & Wang, 1984). This can be corrected by introducing a cut-off frequency for the *K* factor. After a certain frequency the pressure is assumed to be the measured pressure.

#### 2.3.2. Nonlinear Wave Theory

If waves become too steep or the water becomes too shallow, linear wave theory is not applicable and the spectra do not provide the complete description of the waves. There are several classical nonlinear wave theories. These theories consider a wave as part of a wave train with constant shape, amplitude, and length. By assuming constant waves, these theories are not ideal for estimating the sea-surface elevation of an irregular sea state

However, Bonneton and Lannes (2017a) developed a method to to reconstruct sea surface elevation of an irregular sea state where the waves do not propagate with constant celerity. This method provides the derivation of the nonlinear formulas for the reconstruction of the sea surface waves for intermediate and shallow waters. The reconstruction of the non-linear formula is shown in Equation 2.14.

$$\zeta_{NL} = \zeta_L - \sqrt{\mu}\sigma\zeta_L\partial_t^2\zeta_L - \sqrt{\mu}\sigma(\partial_t\zeta_L)^2$$
 (2.14)

$$\sigma = \frac{a}{L} \tag{2.15}$$

$$\mu = \frac{2\pi h_0^2}{L^2} \tag{2.16}$$

In this equation  $\zeta$  is the linear (L) and non-linear (NL) dimensionless surface elevation,  $\mu$  is the dimensionless shallowness parameter and  $\sigma$  the dimensionless steepness. The first part of the right side of Equation 2.14 shows the linear approximation of the sea surface elevation. The second part on the right side is the factor that contributes to the wave extrema. This part reduces the troughs and amplifies the wave crest (Bonneton & Lannes, 2017a). The third part on the right side enhances the waves skewness and wave asymmetry.

The linear reconstruction of the surface elevation in the non-linear method uses the transfer function method as described in Section 2.3.1. The only difference with the linear method is that in the last steps, in addition to the linear inverse Fourier transform, two other inverse Fourier transforms are used. The linear time derivatives are used to compute the non-linear surface elevation, resulting in Equation 2.14.

Equation 2.14 entails the fully dispersive method for intermediate waters. However in a shallow regime the waves are not dispersive. Bonneton and Lannes (2017a) developed a weakly dispersive method to compute the surface elevation in a shallower zone. The distinction between shallow water and intermediate water is made by the shallowness parameter  $\mu$  as shown in Equation 2.16. Shallow water is indicated if  $\mu << 1$  and intermediate water if  $\mu \sim 1$ . The representation of the weakly dispersive reconstruction is given in Equation 2.17. There  $\zeta_H$  represents the hydrostatic surface elevation. In a weakly dispersive formula the linear part is derived from the simplification of the linear reconstruction.

$$\zeta_{SNL} = \zeta_{SL} - \epsilon \mu (\zeta_{SL} \delta_t \zeta_{SL}) \tag{2.17}$$

### 2.4. Wave Shape Characterization and Parameterization

In this section wave skewness and asymmetry are discussed. Furthermore, the parameterization of wave non-linearities is explained. This parameterization is used to estimate the skewed-asymmetric shape of the near-bed wave orbital motion which is relevant for onshore sediment transport. It should be noted that these wave characteristics and parameterizations are studied in the near shore by Doering and Bowen (1995) and Ruessink, Ramaekers, and Van Rijn (2012).

#### 2.4.1. Characterization of waves

In the near shore, skewness and asymmetry are measures wave nonlinearity. An increase in non-linearity is caused by decreasing depth, where wave start shoaling. As waves become asymmetric along the horizontal axis, as shown in Figure 2.2, this is called skewness.

8 2. Literature Review

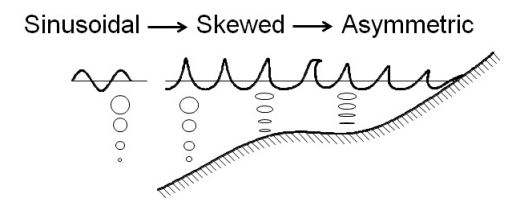


Figure 2.2: Wave propagation under influence of the bottom. The wave shape first becomes positively skewed and then before wave breaks, the wave shape becomes asymmetric (*LEGI - UMR 5519 - Nonlinearities of waves propagating over a mild-slope beach: laboratory and numerical results*, n.d.)

As waves propagate further towards the coast, the wave shape becomes more asymmetric, around the vertical axis, until they break.

Skewness, when the peaks become higher and shorter and the trough shallower, can be qualified by means of the velocity skewness coefficient  $R_u$ , as shown in Equation 2.18 (Ruessink et al., 2012). Waves that are increasingly pitched forward with a steep front face and a gentle rear face, show type of non-linearity is called asymmetry (Ruessink et al., 2012). Asymmetry is related to skewness by the derivative of u and the acceleration a. This can be described with the acceleration skewness coefficient  $R_a$ , as shown in Equation 2.19.

$$R_u = \frac{u_c}{u_c - u_t} \tag{2.18}$$

$$R_a = \frac{a_c}{a_c - a_t} \tag{2.19}$$

Equation 2.20 and Equation 2.21 describe the wave shape in terms of a parameter, respectively the skewness and asymmetry parameter (Berni, Barthélemy, & Michallet, 2013). In the skewness parameter u(z,t) is the cross-shore horizontal velocity, where the over bar notes the time-averaged over the interval. For the asymmetry parameter the imaginary part of the Hilbert transform  $\mathcal{H}$  of u is used. These parameters  $Sk_u$  and  $As_u$  are preferred over  $R_u$  because the latter is applicable on individual waves only.

$$Sk_u = \frac{(u(z, t\bar{1} - \bar{u})^3)}{(u_{rms}^2)^{3/2}}$$
 (2.20)

$$As_{u} = \frac{\Im(\mathcal{H}(u)^{3})}{\langle u_{rms}^{2} \rangle^{3/2}}$$
 (2.21)

The degree of sea surface elevation non-linearity is quantified by the Ursell number  $U_r$ . The Ursell number combines the steepness of the waves with the relative water depth.

$$U_r = \frac{steepness}{(relative\ depth)^3} = \frac{(H/L)}{(d/L)^3} \quad or \quad \frac{3}{4} \frac{a_w k}{(kh)^3}$$
 (2.22)

The Ursell number can be rewritten in a number of ways. Equation 2.22 represents the ratio between the amplitude of the harmonic wave and the amplitude of the second order Stokes correction. In other words, to determine the steepness of the waves, the wave height *H* is divided by the wave length *L*. The Ursell number is a ratio indicates the applicability of the various wave theories (Holthuijsen, 2007).

#### 2.4.2. Parameterization of the wave shape

Parameterizations of the wave shape in the near shore zone are used in several morphodynamic models. To describe the the free-stream near-bed horizontal orbital motion, Abreu, Silva, Sancho, and Temperville (2010) introduced a simple analytical expression to use in his developed parameterization method.

$$u(t) = \hat{U}_w f \frac{\left[\sin(\omega t) + \frac{r\sin(\phi)}{1 + \sqrt{1 - r^2}}\right]}{\left[1 - r\cos(\omega t + \phi)\right]}$$
(2.23)

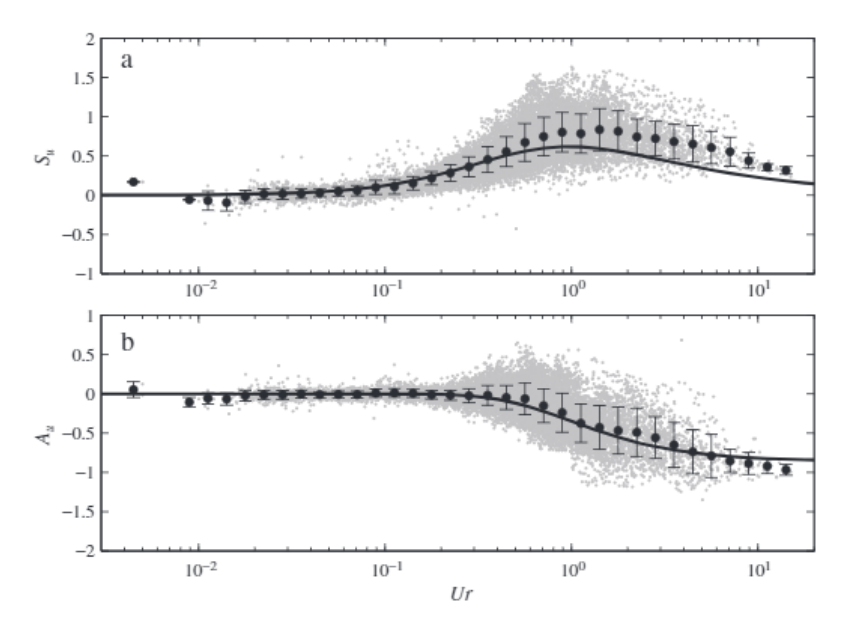


Figure 2.3: Near-bed velocity skewness and asymmetry as a function of the Ursel number. The dots represent the class mean based on binning. The line represents a fit proposed by Ruessink et al. (2012).

In this equation r is the index of skewness or nonlinearity and is related with n, the  $r=2n/(1+n^2)$ .  $U_w=(u_{max}-u_{min})/2$  is the velocity amplitude.  $f=\sqrt{1-r^2}$  is a dimensionless factor as a function of r and  $U_w$  is the velocity amplitude. Next,  $\phi$  is the wave form parameter and  $\hat{u}_b$  is the velocity amplitude. This analytical function is useful for calculating the sediment transport directly for the wave skewness/asymmetry parameters. (Abreu et al., 2010). The corresponding acceleration of Equation 2.23 is given by:

$$a(t) = U_w \omega f \frac{\cos(\omega t) - r\cos(\phi) - \frac{r^2}{1 + \sqrt{1 - r^2}} \sin(\phi) \sin(\omega t + \phi)}{[1 - r\cos(\omega t + \phi)]^2}$$
(2.24)

However, u(t) obtained from Equation 2.23 is monochromatic and not applicable for a series of natural random waves. Ruessink et al. (2012) further developed this method to compute the nonlinearity parameters r and  $\psi$  in Equation 2.23 as a function of the representative wave height and period. In the following section the parameterization of Ruessink et al. (2012) is further explained.

The data used for developing the parameterization is collected during a series of field campaigns at barred beaches in the Netherlands and France. Pressure and near-bed velocity recordings were taken with an ADV's and pressure sensors. Measurements  $H_s$  ranged from 0.05 to 3.99 m,  $T_p$  was between 3.1 and 13.9s and the depth h was between 0.25 and 11.2m. From the velocity data,  $S_k$  and  $A_s$  can be calculated, the Ursell number can calculated from pressure and velocity data. Finally,  $S_k$  and  $A_s$  combined with the Ursell number as in Figure 2.3

First, the  $Sk_u$  and  $As_u$  can be combined into a measure of total nonlinearity B and phase  $\Psi$ . A combined measure of total dimensionless nonlinearity B and phase  $\Psi$  can be described by Equation 2.25 and Equation 2.26:

$$B = \sqrt{S_k^2 + A_s^2} (2.25)$$

$$\Psi = tan^{-1}(A_s/S_k) \tag{2.26}$$

As velcoity skewness increases with higher wave nonlinearities, Ruessink et al. (2012) proposed standard fit curves for this relationship with dimensionless parameters based on B and  $\Psi$ . As shown in Equation 2.25 and Equation 2.26, the dimensionless parameters B and

10 2. Literature Review

 $\Psi$  are dependent on the skewness and asymmetry. In order to fit the relationship between the Ursell number and the skewness and asymmetry parameters (Figure 2.3), B and  $\Psi$  are parameterized as in Equation 2.27 and Equation 2.28:

$$B = p_1 + \frac{p_2 - p_1}{1 + exp \frac{p_3 - \log(Ur)}{p_4}}$$
 (2.27)

and

$$\Psi = -90^{\circ} + 90^{\circ} \tanh(p_5/Ur^{p6})$$
 (2.28)

with  $p_1 = 0$ ,  $p_2 = 0.857 \pm 0.016$ ,  $p_3 = -0.417 \pm 0.025$ ,  $p_4 = 0.297 \pm 0.021$ ,  $p_5 = 0.815 \pm 0.055$  and  $p_6 = 0.672 \pm 0.073$ . The  $\pm$ -sign represents the 95 % confidence interval. The fit is shown in Figure 2.3.

Other wave parameters have been proposed by several authors such as the velocity leaning index  $\beta_c$  by Watanabe and Sato (2004).

$$\beta_{cw} = 1 - \frac{2T_c}{T} \tag{2.29}$$

In Ruessink et al. (2012) the velocity asymmetry is expressed by  $\alpha$ :

$$\alpha = 2T_c/T \tag{2.30}$$

In both expressions,  $T_c$  corresponds to the duration from the negative-to-positive zero-crossing, and T the significant wave period. According to Abreu et al. (2010), Elfrink (2006) has done extensive field measurements and determined that the range of non-linearity yields  $0.51 \le R \le 0.66$  and  $0.22 \le \alpha \le 0.54$ .

#### 2.5. Velocity under Waves

The flow over the entire water depth results from an interaction between the waves and currents. As mentioned in Section 2.1, it is common to divide the flow into layers, because the length- and time scales of the waves and currents differ. One layer close to the sea bed is dominated by the waves. Another layer further away from the seabed is dominated by the currents. The wave bottom boundary layer is typically a few centimeters thick, while the current boundary layer occupies a significant part of the water depth (Holmedal, Myrhaug, & Rue, 2003). However, the flow in the wave bottom boundary layer and the current boundary layer are interdependent.



Figure 2.4: Vertical velocity profile with irregular bottom. ()

In the following section the distinction between the free-stream velocity and the wave bottom boundary layer velocity is discussed. Rotation in free-stream velocity is assumed to be zero while in the bottom boundary layer the rotation is not negligible. Figure 2.4 shows that the bottom boundary layer is formed by the roughness of the seabed.

#### 2.5.1. Free-stream velocity

The wave orbital velocity for small amplitude waves is predicted with linear wave theory. The horizontal component of the orbital velocity close to the bed is evaluated as:

$$u_0 = \frac{H\phi}{Tsinh(kh)}cos(kx - wt)$$
 (2.31)

It is assumed that the vertical orbital velocity in the free-stream layer decreases to zero as  $z \to -h$ . The wave orbital velocity varies sinusoidally through a wave period, going towards its maximum horizontal velocity when  $|cos(kx-\omega t)|=1$ . This results in the following velocity on top of the wave boundary layer:

$$\hat{u}_0 = \frac{\omega a}{\sinh(kh)} \tag{2.32}$$

Abreu et al (2009) developed formula for the skewed, non-linear, near-bed wave orbital velocity. Containing four parameters. Two parameters depend only on the velocity and acceleration skewness, as described in Section 2.4. The work of Abreu is based on previous work from Drake and Calantoni(2001), who considered the near-bed velocity proportional to a wide range of shoaling and broken waves.

$$u(t) \propto \hat{U}_w \sum_{k=0}^{\infty} \frac{1}{n^k} sin[(k+1)\omega t + k\phi]$$
 (2.33)

#### 2.5.2. Wave bottom boundary velocity

The bottom boundary layer flow under waves and currents is determined by the near-bed wave velocity with corresponding orbital displacements, near-bed current velocity, bottom roughness, water depth, and angle of attack of waves on the current (Holmedal et al., 2003). The bottom orbital velocity is directly related to the wave height and inversely to the water depth. The wave period determines the thickness of the wave bottom boundary layer. If the wave period rises the wave bottom boundary layer has more time to develop and increases as well. The thickness of the boundary layer can also increase due to bed roughness or viscosity. The transformation from free-stream velocity asymmetry to the bottom velocity skewness in the bottom boundary layer is described by Henderson and Allen (2004).

#### 2.6. Change of Wave Spectra in Presence of Current

As waves propagate in the direction of the current modifications in the surface elevation spectrum occurs. To derive this spectrum transformation the following assumptions are made:

- The current is vertically uniform
- The waves are generated on still water and subsequently encounter the current
- The random waves are long crested and the wave rays perpendicular to the current
- The water depth is sufficiently large, so deep water is considered.

In the absence of wave generation or dissipation, the principle of wave action conservation may be used to show that the surface elevation spectral density function for deep-water waves on a current  $S_{nn}(\omega, U)$  is given by Equation 2.34 (Burrows & Hedges, 1985):

$$S_{\eta\eta}(\omega, U) = \frac{4S_{\eta\eta}(\omega)}{\left[1 + \left(1 + \frac{4U\omega}{g}\right)^{1/2}\right]^2 \left[1 + \frac{4U\omega}{g}\right]^{1/2}}$$
(2.34)

In this equation,  $S_{\eta\eta}(\omega)$  is the spectral density function in case the zero-current area from the deep-water waves have propagated without refracting. U is the current velocity in the direction of wave propagation;  $\omega$  is the absolute wave angular frequency and g the gravitational constant. However, wave growth in any frequency band of the spectrum is limited by wave breaking. The spectral density limit for random wave propagation directly with or against the current in deep water conditions is given in Equation 2.35 (Burrows & Hedges, 1985). The wave length increases for waves on a following current while the amplitude decreases. This causes a drop in the surface elevation spectral density. As the waves encounter an opposing current, the waves shorten and steepen, causing a spectral density increase toward the higher frequencies, as shown in Figure 2.5 (Jonsson, 1991).

12 2. Literature Review

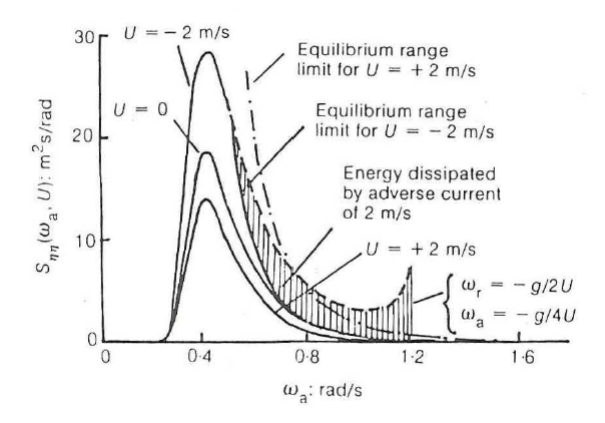


Figure 2.5: Change in deep water surface elevation spectra (Jonsson, 1991)

$$S_{\eta\eta ER}(\omega, U) = \frac{Ag^2}{[\omega - kU]^5} \frac{1}{[1 + \frac{2U}{g}(\omega - kU)]}$$
(2.35)

The subscript ER refers to the equilibrium range and A is a numerical constant. The factor  $(\omega - kU)$  is derived from the deep-water linear theory dispersion. The transformation in surface elevation spectra as waves encounter a current is governed by Equation 2.34 provided  $S_{nn}(\omega, U) \leq S_{nn}ER$ .

After determining the spectrum of the free-surface displacement the corresponding spectrum for the horizontal velocity component of the water particles velocity (Terence, 1985) can be predicted with Equation 2.36.

$$S_{uu}(\omega_a, U) = (\omega_a - kU)^2 \frac{\cosh^2 k(d+z)}{\sinh^2 kd} S_{\eta\eta}(\omega_a, U)$$
 (2.36)

When the frequency spectrum in the region without a current has the form  $S_0(\omega)$  and moves toward a region with non-uniform current, the higher spectrum harmonics will be filtered out by bottom and current effects with the cut-off frequency  $\omega_{cr}$ . This expression can be derived from the dispersion equation, as shown below in Equation 2.37

$$\omega_{st}^2 = gk_{st}tanh(k_{st}h) \tag{2.37}$$

The wave number  $k_{st}$  gives the location of the reflection point is for velocity  $U_{st}$  (Burrows & Hedges, 1985) From this the transformation ratio with respect to the mean wave height with a vertically non-uniform current can be defined, as shown in Equation 2.38. (Kantardgi & Dreyzis, 1993)

$$\frac{\bar{H_c}^2}{\bar{H_o}^2} = \int_0^{\omega_{st}} S_0(\omega) d\omega / \int_0^\infty S_0(\omega) d\omega$$
 (2.38)

## Field Experiment

This chapter outlines the field experiment by discussing general parameters, frame set-up and general initial data.

To obtain information about the transformation of waves due to currents a field experiment was executed. The measurements were performed during the SEAWAD field campaign. SEAWAD stands for <u>SE</u>diment supply <u>At</u> the <u>WA</u>dden Sea ebb-tidal <u>Delta</u>. The SEAWAD campaign was held in conjunction with Kustgenese II August 28 to October 9, 2017. By using five frames at different depths at the bottom of the sea, several quantities are measured, including the pressure and directional velocity parameters are of importance to determine the wave transformation. This chapter gives an overview of the conditions around the measurement area in the northwest of Ameland. This area is shown in 3.1.

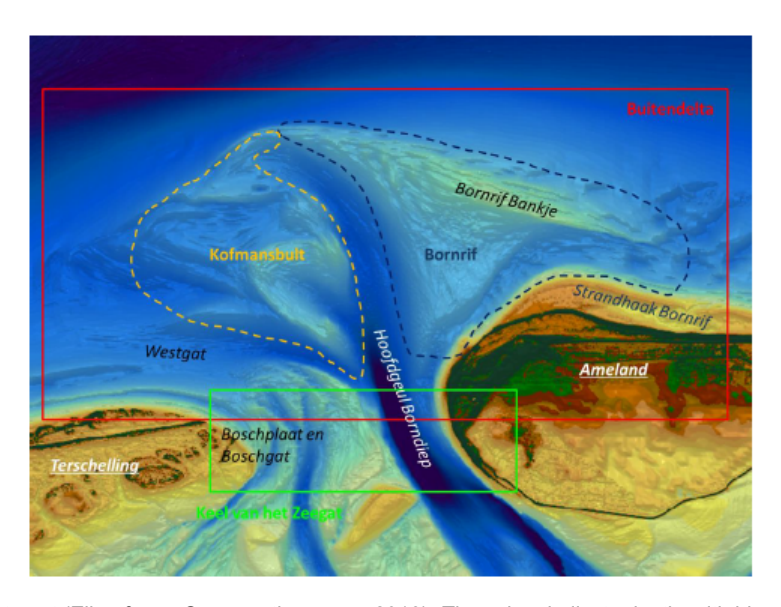


Figure 3.1: Area of interest (Elias & van Oeveren-theeuwes, 2016). The colors indicate depth, with blue for the deeper areas, and red for shallower areas.

#### 3.1. Field Site

The site is located northwest of Ameland, a Wadden Island north of the Netherlands in the vicinity of the entrance channel connecting the Wadden Sea to the North Sea. The main channel is called the Bornediep and the ebb-channels are called Westgat, and Bornrif as shown in Figure 3.1.

14 3. Field Experiment

#### 3.2. Instruments and Settings

In this section, the frames and their location, instruments, and instrument settings are discussed. The location of the frames can be found in Figure 3.2. The SEAWAD field campaign used five frames located at the seabed. The frames were equipped with different sensors, as described in the next section. Pressure sensors were located near frame 4 and frame 5. The exact locations of the sensors are given in Table B.2.



Figure 3.2: Orientation of pressure sensors (green) and frames (red)

#### 3.2.1. Frames and instruments

During the SEAWAD campaign five measurement frames were located at the seabed on the North Sea. The frames equipped with the ADV's and ADCP's were deployed for 42 days, from August 28 to October 9, 2017. A visual representation of the frames is shown in Figure 3.3. The frames have dimensions of 3x3x3m. The frames are situated northwest of Kofmansbult, as shown in Figure 3.1. Frame 5 is located at a depth of 5 m below NAP and frame 4 is located at a depth of 8 m below Nieuw Amsterdams Peil (NAP). The pressure sensors are located around frames 4 and 5. The numbering of the pressure sensors is given in Figure 3.2. The exact longitude and latitude corresponding to the location of the sensors are given in Appendix B.

While instrumentation on a given frame differs, overall, the following equipment is used:

- Acoustic Doppler Current Profiler (ADCP)
- Acoustic Doppler Velocimeter (ADV)
- Optical backscatter point sensor (OBS)
- · Aquadopp HR
- 3D Profiling Sonar
- LISST
- Pressure sensors

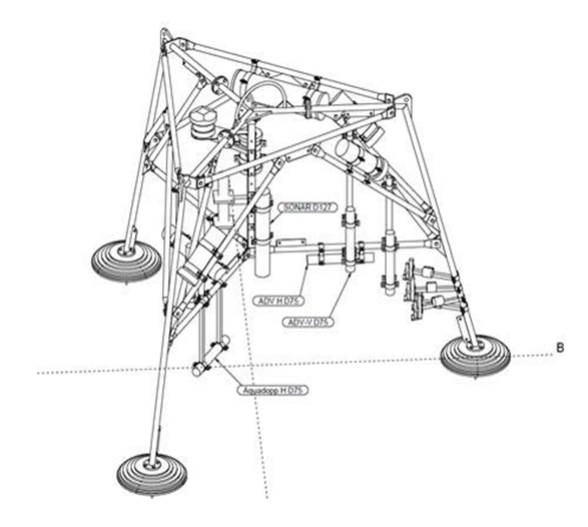


Figure 3.3: Impression frame (Elias & van Oeveren-theeuwes, 2016)

Table 3.1: Instrument setting of ADV, ADCP and pressure sensors of frame 4 and frame 5

Instrument	Frequency [Hz]	Continuous [yes/no]	Duration burst [s]	Brand instrument	
Pressure Sensors [PS]					
PS 1-8	10	yes	-		
	Frame 4				
ADV with PS	16	no	1790	Nortek	
ADCP	1,25	no	1800	Nortek	
Frame 5					
ADV	10	no	1740	Sontek	
AquadoppHR	4	no	1740	Nortek	

#### 3.2.2. Setting Instruments

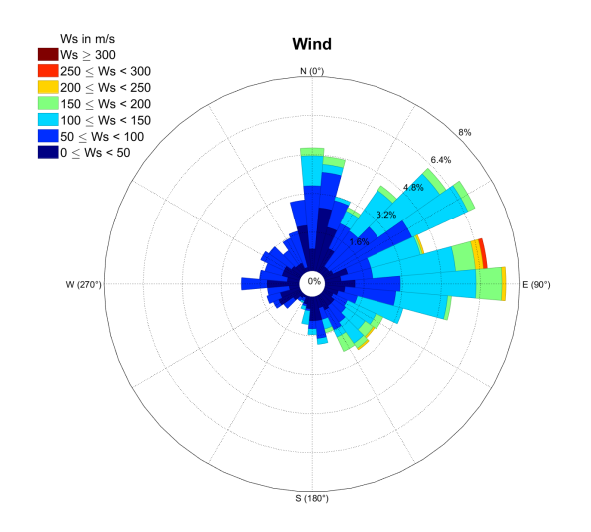
The data from the ADV's, ADCP, Aquadopp and pressure sensors is used in further analysis. The instrument settings of those instruments are listed in Table 3.1. The instrument settings of the other instruments on the frame can be found in Appendix B. The ADV of frames 4 and 5 measured in burst mode, meaning that every half hour, it measures the distance to the bottom for 10 seconds. The frequency of the ADV's on frame 4 is 16 Hz, and the frequency of the ADV's on frame 5 is at 10 Hz. The Aquadopp mounted on frame 5 had a frequency of 4 Hz. The ADCP measured in burst mode at 1.25 Hz. The pressure sensors sampled at 10 Hz continuously. The settings of the other instruments on the frames are given in Appendix B.

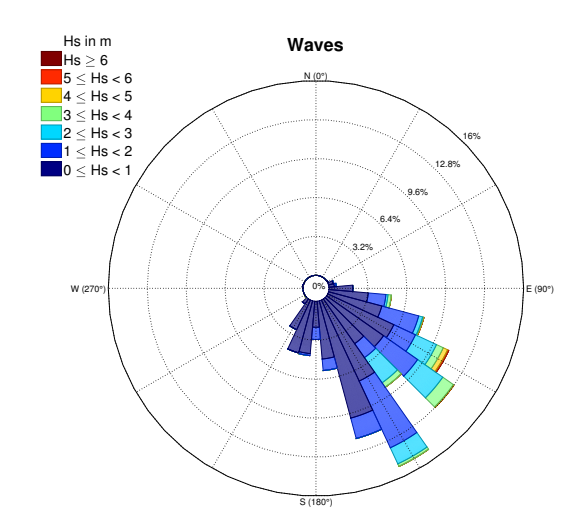
During the field campaign ADV3 and pressure sensor P6 were damaged. ADV3 was bent when the frames were retrieved for servicing. Pressure sensor 6 did not measure during the field campaign. In the analysis those instruments are not used.

#### 3.3. Environmental Conditions

In this section, the wind, wave, and tidal conditions near the site during the measurements are given. The conditions are summarized in Figures 3.4a and 5.1 and a further explanation of the figures is given in the subsections that follow.

16 3. Field Experiment

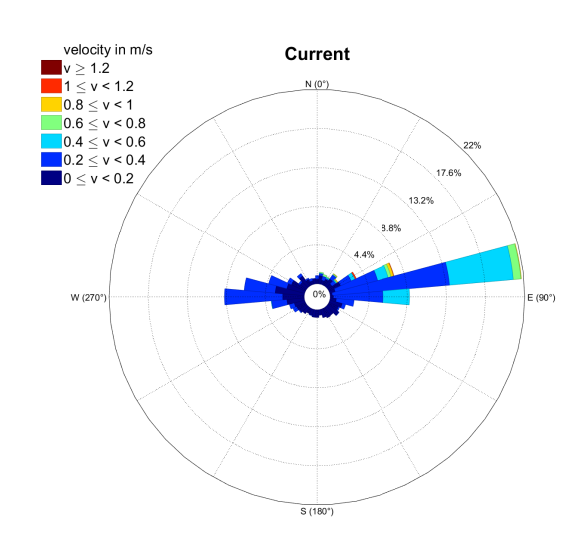


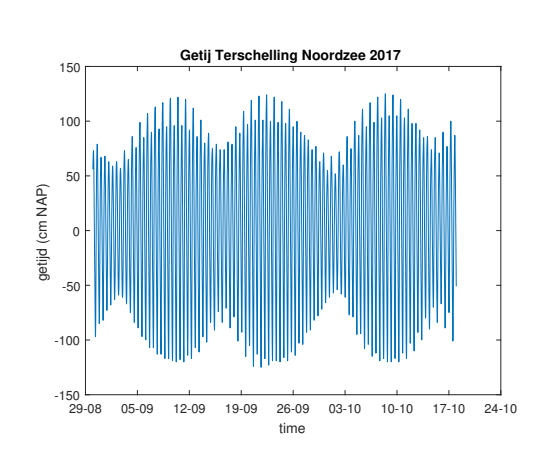


(a) Wind data near Vlieland

Figure 3.4: Environmental conditions







(b) Tide North Sea

(a) Currents and propagation directions

Figure 3.5: Environmental conditions

#### 3.3.1. Wind

The hourly average wind speed with the corresponding direction is given in the windrose in Figure 3.4a. This data was recorded at the measurement station of the Koninklijk Nederlands Meteorologisch Instituut (KNMI) at Vlieland (KNMI, 2014) 16 kilometers form the measuring site. As shown by the wind rose, main direction for wind propagation is SW up to NWW. note that wind rose indicates wind propagation, which is the opposite the more-conventional wind direction. The maximum wind speed during the campaign is below 30m/s.

#### 3.3.2. Waves

As shown in Figure 5.1, the governing wave direction is SE and the maximum significant wave height is less than 6m. The wave height and nautical direction are obtained from the pressure sensors and velocity meters of ADV 2 on frame 4. The wave directions in the rose are the propagation direction of the waves.

#### 3.3.3. Tides

The tidal amplitude over the measurement period varies from 1.4 m to 0.8 m in the springneap tidal cycle, with a mean tidal range of 2.0 m (Elias & van Oeveren-theeuwes, 2016), as shown in Figure 3.5b. The tide propagates along the coastline of Ameland to the northeast. The tide is a mainly semi-diurnal (M2) constituent. Figure 3.5b shows the measured tidal amplitude during the field campaign measured at the buoy offshore Terschelling.

#### 3.3.4. Currents

The currents in the area are measured with ADV's. Every 30 minutes the mean velocity is determined in the horizontal (east, north) and vertical (up) (ENU) direction. The direction and magnitude of the current velocity is determined using the Pythagoream theorem. Figure 3.5a shows the magnitude of the current velocity and its corresponding direction. The flow directions are in the flow propagation direction. The currents clearly show two main directions east and west.

## **Data Processing**

In this chapter, the data processing methodology is explained.

The raw data is processed to obtain useful data for analysis. The process involves removing outliers, clean data of instrumental errors, and correcting and analyzing to obtain the correct parameters. The different steps in the post-processing are explained.

As described in Chapter 3, the ADV and ADCP measured in burst mode. To simplify the analysis and avoid gaps in the data, the data is divided into blocks and a time vector is added. An overview of the steps is given in Figure 4.1.

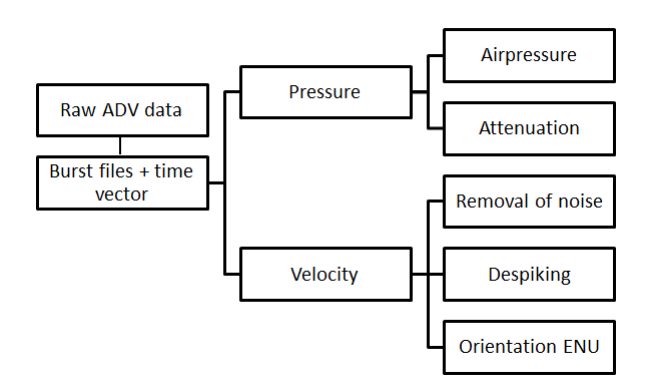


Figure 4.1: Overview of data processing steps

#### 4.1. Pressure Correction

Sections 4.1.1 and 4.1.2 describe the methods used to make correction in the air pressure and pressure attenuation.

#### 4.1.1. Air pressure correction

The total pressure of the ADV is the summation of the air pressure plus the water pressure head. As only the water pressure is necessary for the analysis of the results. Fluctuations in atmospheric pressure need to be subtracted from the pressure signal, as shown in Equation 4.1

$$p_{wave} = p_{total} - p_{atm} (4.1)$$

#### 4.1.2. Pressure attenuation

The pressure measured by the ADV is not directly related to the surface wave height. The pressure head at the sea floor does not equal real the surface level change. Vertical accelerations in the above water column cause forces to act on a particles, and accompanied by

20 4. Data Processing

a gradient in the water column pressure (Grace, 1978). When using linear wave theory to predict the surface height based on the total pressure head, the pressure needs to be attenuated up to frequencies of 0.33 Hz. This frequency is chosen to in order to amplify only those waves with a period higher than 3 seconds, as lower frequencies could be noise.

This factor is described by Equation 4.2:

$$\hat{p}_{wave} = \rho g a \frac{\cosh[k(d+z)]}{\cosh(kd)} \tag{4.2}$$

In this equation, d is the water depth, z the surface elevation and k the wave number (Holthuijsen, 2007). Equation 4.2 applies for regular waves. For irregular waves, after applying a fast Fourier transform, the attenuation factor corrects per frequency before using an inverse Fourier transform to obtain the surface elevation signal. This attenuation factor implies that the sea surface height is larger for smaller water depth to wave length ratios and the sea surface height is smaller for larger water depth to wavelength ratios.

Linear wave theory is applied to obtain sea surface elevation. However, before reaching this conclusion an analysis of methods for obtaining the sea surface elevation was conducted. In the first analysis, presented Appendix D, the linear wave theory is compared with the nonlinear transformation of Bonneton (2017). Bonneton and Lannes (2017a) derived a method which allows the elevation reconstruction of water wave in intermediate and shallow waters. This method describes the nonlinear terms, like skewness and asymmetry better. This method is only applied op monochromatic surface waves, but not tested for irregular ocean waves. The analysis concluded that a cut-off frequency of 0.25Hz would give reasonable estimation of the wave height. However, the wave height and wave skewness greatly depend on the cut-off frequency and no check on the real surface elevation can be done, this non-linear method is not used.

Secondly, currents are included in linear wave theory. Assuming a depth-averaged flow velocity, and a cut-off frequency of 0.25Hz. Observing the wave spectra, the energy in the spectra shows a shift toward higher frequencies for opposing flow and shift toward lower frequencies for following flow. The results show for high opposing flows a shift of the spectral peak towards the cut-off frequency, and furthermore unrealistically high wave heights. While, the frequency shift not changes the skewness and asymmetry profoundly. Therefore, linear wave theory with currents included will also not be used.

#### 4.2. Velocity Signal Correction

The quality of the velocity signal needs to be verified before interpreting the data. The validity of the obtained signal after the correction is discussed in Appendix C. In this section the removal of low correlation, noise, and spikes is explained, as well the transformation from the XYZ coordinates to ENU coordinates.

#### 4.2.1. Correlation, noise and Spikes

To correct the velocity signal, errors are removed in the following order: correlation, the signal to noise ratio (SNR) and finally despiked. After the removal of the points with low correlation and low SNR, the data is interpolated with a cubic spline method and then the spikes are removed.

**Correlation and SNR** are communication errors of the instrument. For each individual beam of the ADV the correlation (70%) and SNR (15dB) is checked. These thresholds are recommended by the manufacturer (Nortek, n.d.). If the correlation of SNR is below the threshold the points are removed from the velocity signal.

**Spikes** are generally caused by aliasing of the Doppler signal, which is a phase shift between the incoming and outgoing pulse. This phenomenon can occur if the flow velocity exceeds the set velocity range or the seabed geometry changes. In despiking the phase-space thresholding technique of Nikora and Goring (2002) is used. This method finds the second order derivatives of the velocity signal, then calculates the standard deviation of the original velocity signal as well as the first and second order derivative. The method can be used to create a dense point cloud and construct an ellipsoid in the three-dimensional phase space

4.3. Wave Spectra 21

which yields the first order and second order derivatives plotted against each other, as shown in Figure 4.2. The points lying outside the ellipsoid are designated as spikes. After the spikes are removed, the velocity signal is cubically interpolated.

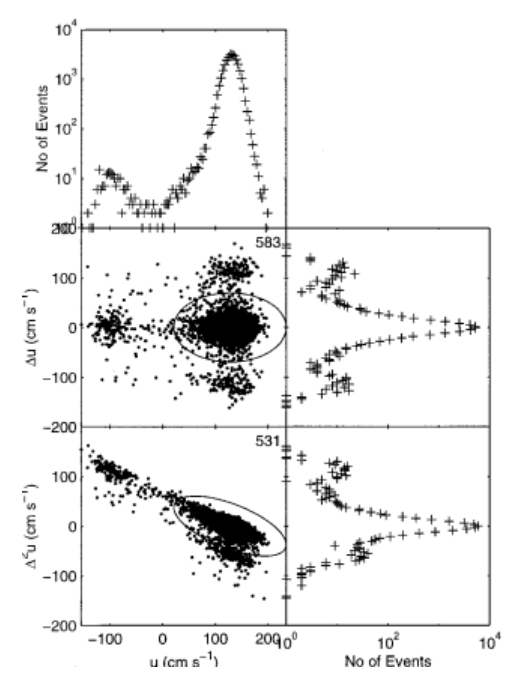


Figure 4.2: Phase-space plots (Nikora & Goring, n.d.)

#### 4.2.2. Orientation to ENU

The set coordinate system in the ADV is the Earth-Centered Earth-Fixed (ECEF) coordinates. To translate the ECEF coordinates to ENU coordinates, a few transformations have to be done. The coordinates transformation is calculated using the internal heading, pitch, and roll of the ADV, which is given in the .SEN file of the ADV. The standard transformation matrix of the ADV can be found in the . HDR file.

The resulting transformation matrix contains the equations shown in Equations 4.3 and 4.4:

$$R = H * P * T \quad with \quad P = \begin{bmatrix} cos(pp) & -sin(pp) * sin(rr) & -cos(rr) * sin(pp) \\ 0 & cos(rr) & -sin(rr) \\ sin(pp) & sin(rr) * cos(pp) & cos(pp) * cos(rr) \end{bmatrix}$$

$$H = \begin{bmatrix} cos(hh) & sin(hh) & 0 \\ -sin(hh) & cos(hh) & 0 \\ 0 & 0 & 1 \end{bmatrix}$$

$$(4.3)$$

$$H = \begin{bmatrix} cos(hh) & sin(hh) & 0\\ -sin(hh) & cos(hh) & 0\\ 0 & 0 & 1 \end{bmatrix}$$
(4.4)

The pp and rr in Equation 4.3 are the pitch and roll from the .SEN file. H is the heading matrix, Equation 4.4 with hh obtained from the .SEN file. All those parameters pp rr H are obtained from internal device files. ADV 1 has a flex head so therefor the .HDR file can not be used to correct the orientation.

#### 4.3. Wave Spectra

After obtaining the surface elevation with linear wave theory, the wave spectra are determined from the surface elevation. The max entropy method is used to obtain the wave directions and directional spreading from the velocity signal and the surface elevation. This method calculates the directional distribution from the estimates of the Fourier coefficients. The Fourier coefficients are determined by the spectral estimates for complex Gaussian, stationary processes (Lygre & Krogstad, 1986).

22 4. Data Processing

#### 4.4. Currents

Currents are obtained by averaging the velocity components in the east, north and up direction for each block. From those mean currents, the current magnitude and direction is calculated. The maximum current is calculated by the Pythagorean theorem. Additionally, the flow velocity in wave direction is obtained.

#### 4.5. Conclusion

All the above parameters - significant wave height  $H_s$ , peak period  $T_p$ , water depth h and the mean near-bed velocity in the direction of the waves per burst of ADV 2 and ADV 10- are plotted in Figure 4.3. Frame 5 is shown in blue, while the results of frame 4 are plotted in red.

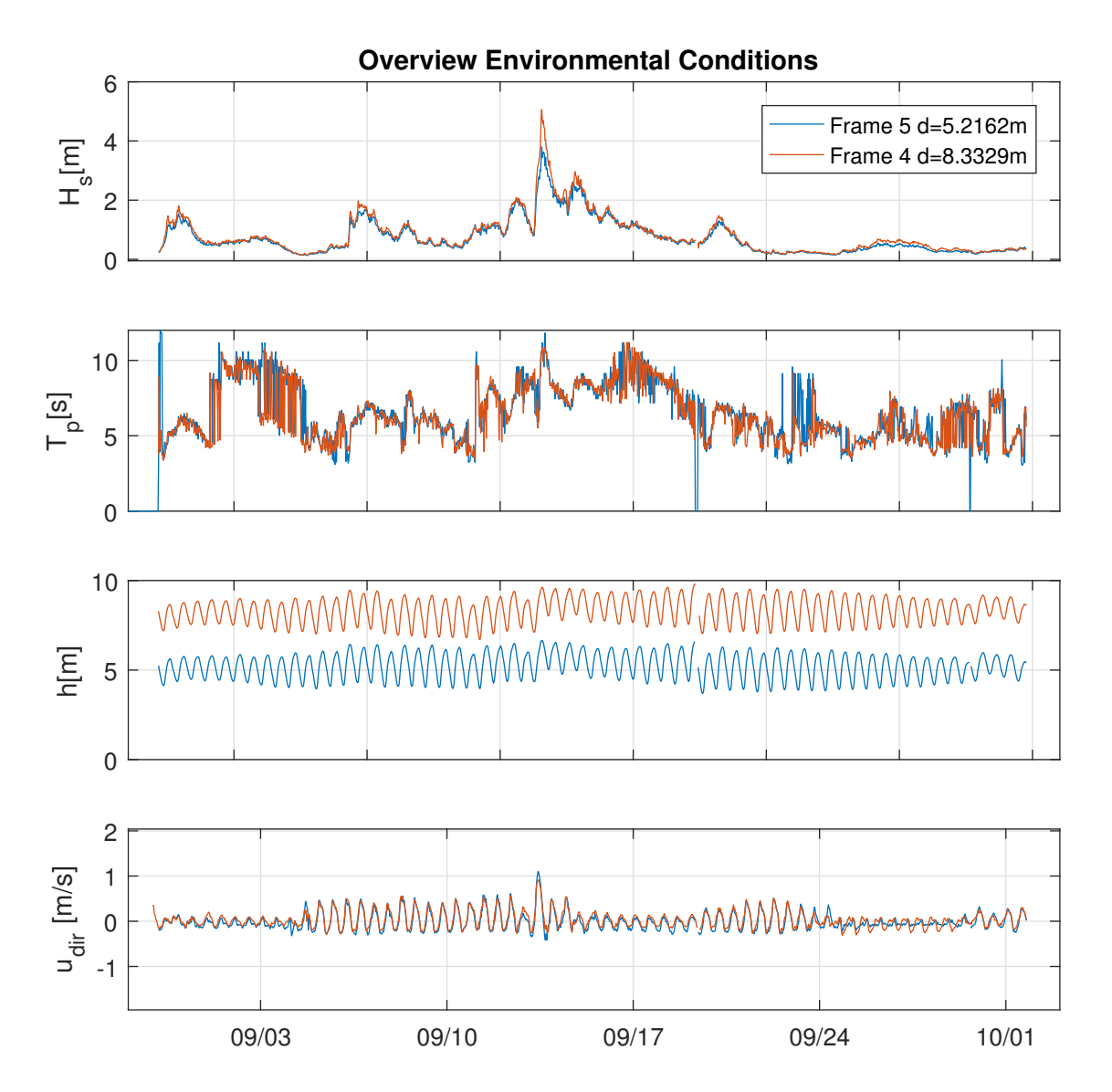


Figure 4.3: Overview of the significant wave height, wave period, mean water depth and depth-averaged current in the direction of the waves of frame 4 (red) and frame 5 (blue)

## Wave Nonlinearity on Ebb Tidal Shoal

This chapter presents the results of the data obtained during the field campaign.

The degree of non-linearity of the wave shape can be described in terms of skewness and asymmetry, as explained in Chapter 2. In addition to the skewness and asymmetry, the Ursell numbers and steepness are common parameters for the wave non-linearity. As nearbed velocity skewness and asymmetry are commonly used in sediment transport models it is relevant to study them in the vicinity of a tidal inlet. Wave skewness and asymmetry have been widely studied in the near-shore zone ((Doering & Bowen, 1995), (Elfrink, Hanes, & Ruessink, 2006a), (Grasso, Michallet, & Barthélemy, 2011), .

In this section, observations, based on pressure sensor data, on the wave shape are discussed in terms of non-linearity and the correlation with the flow velocity are discussed. In this section a distinction is made between the sea surface elevation skewness and asymmetry and near-bed velocity skewness and asymmetry.

#### 5.1. Overview

The sea surface elevation- and velocity skewness and asymmetry, water level, and significant wave height over the duration of the field campaign are calculated in Figure 5.3.

Some general observations can be drawn from Figure 5.3. From top to down, the parameters are, wave height, velocity skewness and asymmetry, sea surface elevation and skewness, Ursell number, water level, near-bed velocity in the direction of the waves and finally the depth-averaged velocity in the direction of the waves. Those parameters for each frame are observed in detail in this section. Frame 4, shown in red, is located at on average water depth of 8m and frame 5 is located at 5 m..

On average  $H_s$  ranged between 0.1 and 2.0 m. However, during a storm from September 12 until September 15, the data shows a peak in significant wave height up to 5.0 m. In the data,  $Sk_u$  ranged between -0.5 to 0.66,  $As_u$  from -0.25 to 0.4, h between 7.8 and 9.6m for frame 5 and 4.6 and 5.7m for frame 4. The Ursell number is ranged from 0 up to 1 for frame 5 while frame 4 has a maximum of 0.5. While in general the values are very small, the numbers start to increase during the observed storm. The velocity  $u_{dir}$  ranged between -0.25 and 1 m/s. The depth-averaged velocity ranged from -0.25 m/s up to 1.6 m/s.

In general, frame 4 has generally much lower values for the sea surface elevation skewness and asymmetry than frame 5. Furthermore, an increasingly significant wave height results in an increase in the sea surface skewness with a correlation of  $R^2 = 0.36$ , as shown in Figure 5.1. The velocity skewness show the same behavior. The same correlation  $R^2 = 0.34$  can be observed for the peak period, with increasing period the skewness increases as well, as shown in Figure 5.2. The correlation between asymmetry and significant wave height and peak period is shown in Appendix E. The correlation between the asymmetry and the local wave parameters,  $H_s$  and  $T_p$ , is weaker. Moreover, the correlation is negative, thus with an increasing period or wave height the asymmetry value deceases, wave become more pitched

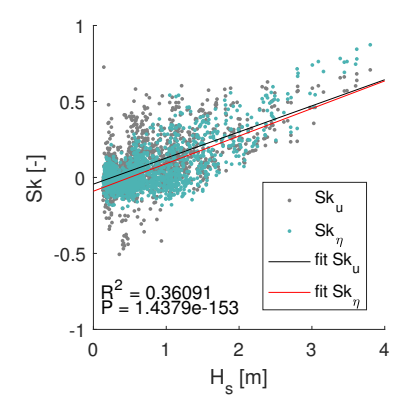


Figure 5.1: The significant wave height versus the sea surface elevation or velocity skewness. The linear fit is positively increasing with significant correlations. Thus the skewness is likely to increase with increasing significant wave height.

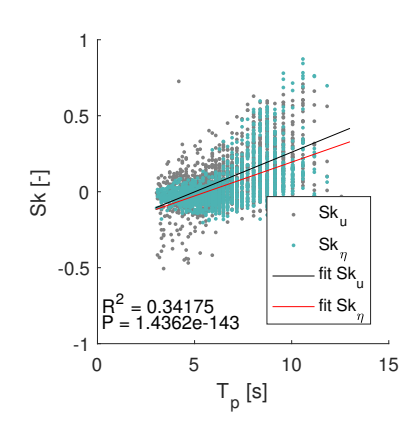


Figure 5.2: The peak period versus the sea surface elevation or velocity skewness. The linear fit is positively increasing with significant correlations. Thus the skewness is likely to increase with wave period.

forward and with a longer tail. To summarize this overview, there is significant wave skewness and asymmetry on the ebb tidal shoal northwest of Ameland.

5.1. Overview 25

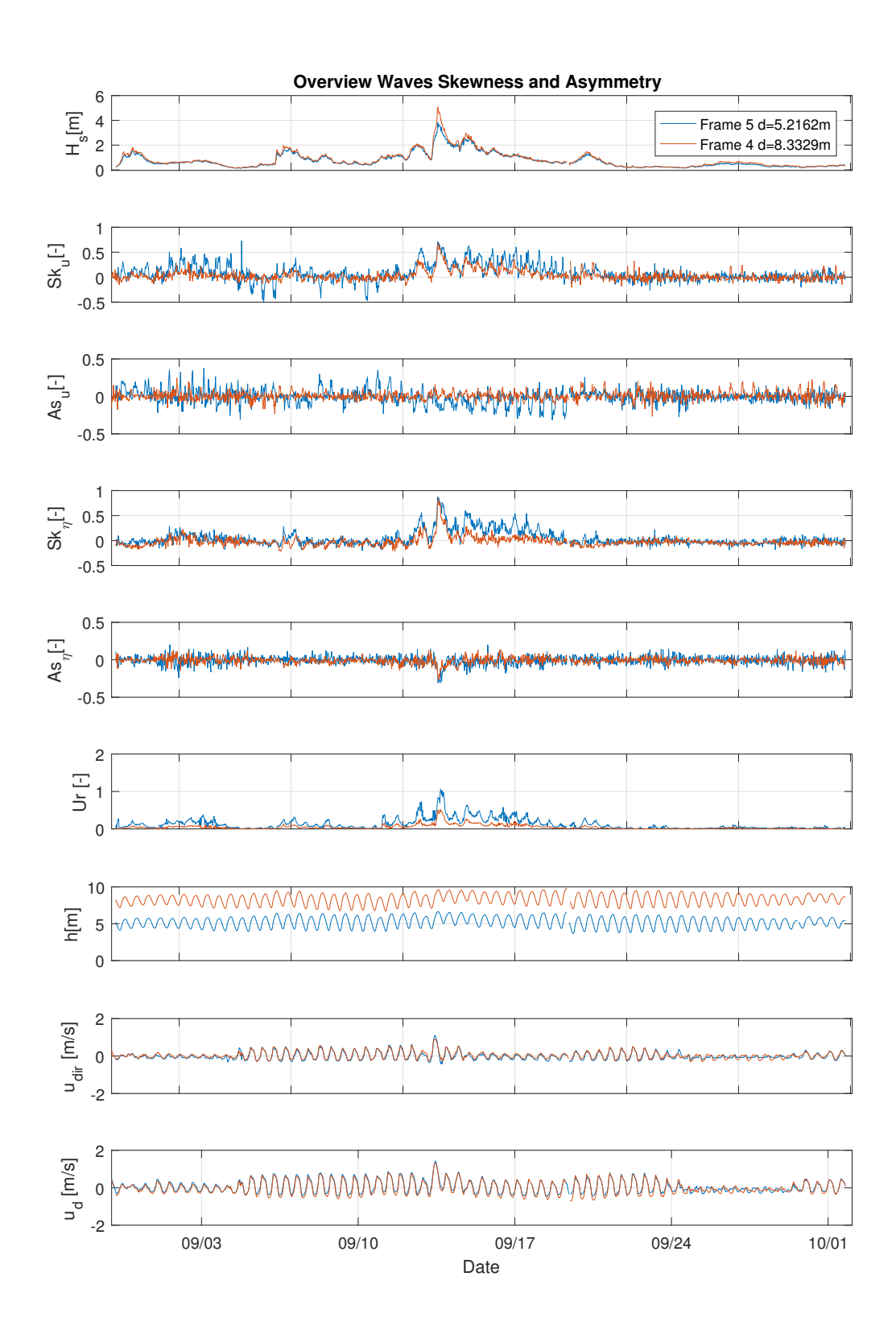
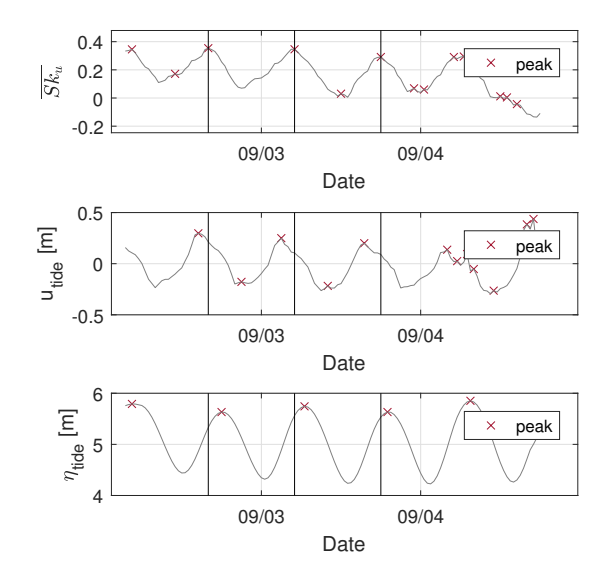


Figure 5.3: Overview of wave and velocity skewness and asymmetry over the duration of the field campaign for frame 4 (red) and frame 5 (blue). From top to bottom; significant wave height, velocity skewness and asymmetry, sea surface elevation skewness and asymmetry, Ursell number, water depth, and velocity in the direction of the wave (ADV 2 and ADV 11), depth-averaged flow in the direction of the waves (ADCP)



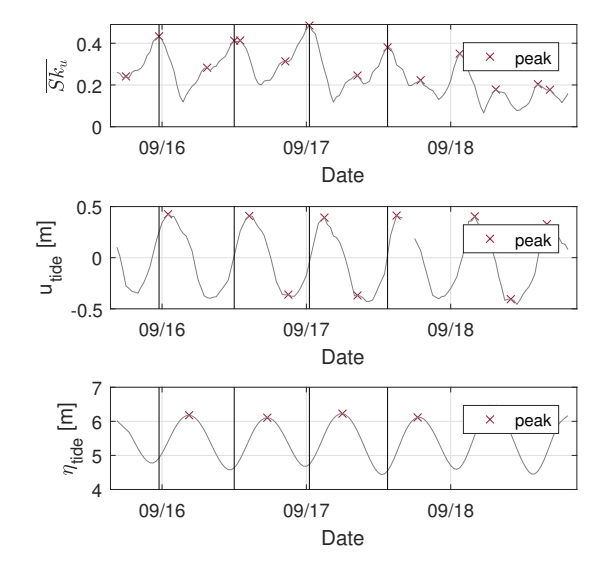


Figure 5.4: Case 1) Skewness, depth-averaged velocity and water level of frame 5 from the 2th of September until the 5th of September.

Figure 5.5: Case 2) Skewness, depth-averaged velocity and water level of frame 5 from the 16th of September until the 19th of September.

Additionally, the wave skewness and asymmetry tend to vary with the tide. Especially the velocity skewness at frame 5 seems to depend on the tide. Especially from September 3 until September 5 (case 1) and from September 16 until September 19 (case 2). The wave parameters averaged over the cases are presented in Table 5.1.

Table 5.1: Wave parameters for cases 1/2. Averaged over the duration of the case.

	Case 1	Case 2
Hs [m]	0.55	1.26
Tp [s]	9.09	8.67
Dir [∘]	166	154

In order to get rid of the peakiness of the original signal, a moving average is taken over 8 burst, leading to  $\widetilde{SK_u}$ . Afterwards the local peaks (red crosses) are computed in Figure 5.4 and Figure 5.5. The local maximum are computed for the depth averaged velocity and the water elevation. The black vertical lines indicate the moment when the skewness is maximum. This is done in order to compare the moment when the maxima skewness occurs in relation to the velocity and water levels. In Appendix E the corresponding times of the peaks are summarized in Table E.1.

When observing Figures 5.4 and 5.5 and Table E.1 the velocity is leading over the water level with on average 3 hours, corresponding with a M2 tide. On the other hand the maximum of the skewness differs per selected duration. Considering case 1), the maximum of the velocity skewness in between the peak of the depth-averaged velocity and the tidal elevation. Following the velocity with 1.5/2 hours and leading with the tidal elevation 1.5/2h. Whereas case 2, the maximum velocity skewness leads with 1.5 hours depth averaged velocity. The maximum velocity skewness occurs at/or moments after low water. For case 2 largest skewness is at low tide, when  $u_{tide} = 0$ , while for case 1 largest skewness is at rising tide. At high water levels and high following velocities.

Concluding from observations the skewness fluctuates with the tidal elevation. The way the skewness depends on the tides is not that straightforward, a lot is depending on the cases. Therefore, more factors come into play a role influencing the skewness.

### 5.2. Sea Surface Elevation Skewness and Asymmetry

In this section, the results of the sea surface elevation skewness versus the Ursell number are presented. First the surface elevation skewness from the frames is discussed, followed by the surface elevation skewness of the pressure sensors. Figure 5.3 shows that surface skewness and asymmetry is present in the ebb-tidal shoal under high waves. Parameterizations of the wave skewness and asymmetry have been developed in the nearshore zone. Since the field site is not confined to the coast, where wave asymmetry can occur due to influences other than the depth, it is interesting to examine how accurately wave skewness and asymmetry can be predicted in this region by existing parameterizations.

The results on the parameterization of the sea surface elevation as a function of the Ursell number can be found in Figure 5.6. All the data from the pressure sensors are combined in Figure 5.6. In total 12.976 data points were available. For  $U_r < 0.05$  both  $Sk_\eta$  and  $As_\eta$  scatter around 0, which means that the orbital motion is sinusoidal. For  $U_r > 0.05$ ,  $Sk_\eta$  increases to a maximum of 0.83 on average, indicating a large wave crest. For  $U_r > 1$  there are no data points available in our data set. The sea surface elevation skewness for each pressure sensor is shown in Figure 5.7, 5.8 and 5.9. The pressure sensors located in the deeper regions show higher higher wave skewness, as shown in Figure 5.11. For the same Ursell numbers  $U_r = 0.3$ , data from the shallower pressure sensors show a sightly lower average skewness than for the deeper pressure sensors. Only this trend is not that obvious. It is clear though from Figure 5.11 that the standard deviation depends on the depth.

In Figure 5.10 the asymmetry for all the pressure sensors is presented. Asymmetry shows little variation for the low Ursell numbers. For  $U_r > 0.05$ ,  $Ak_{\eta}$  increase to maximum of -0.25 on average, with a maximum at -0.7. For  $U_r > 1$  there are no data points available in our data set.

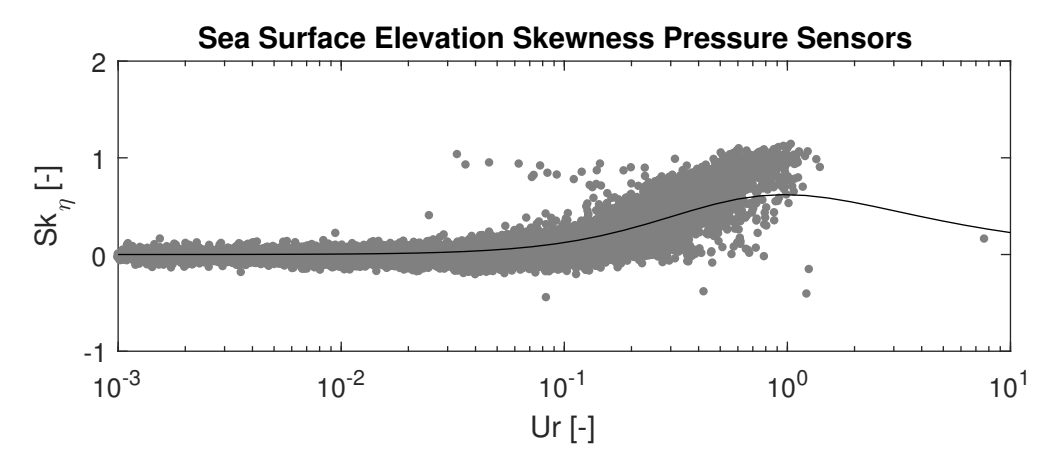


Figure 5.6: Wave skewness for frames 4 and 5 and the pressure sensors P1-5 and P7-8. For the low Ursell numbers the scatter is low, with a higher Ursell number the scatter increases. The continuous black line shows the parameterization fit of Ruessink et al. (2012).

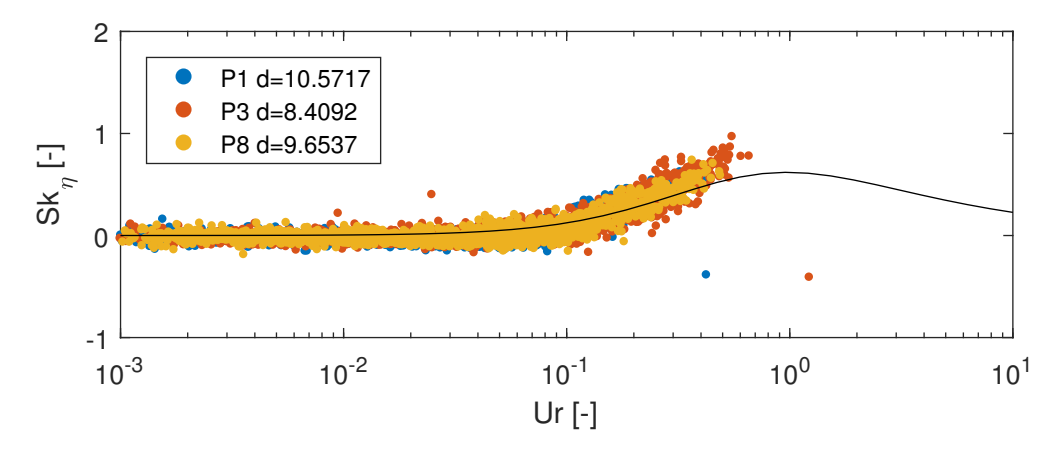


Figure 5.7: Wave skewness versus Ursell number for the pressure sensors 1,3,8. The continuous black line shows the parameterization fit of Ruessink et al. (2012).

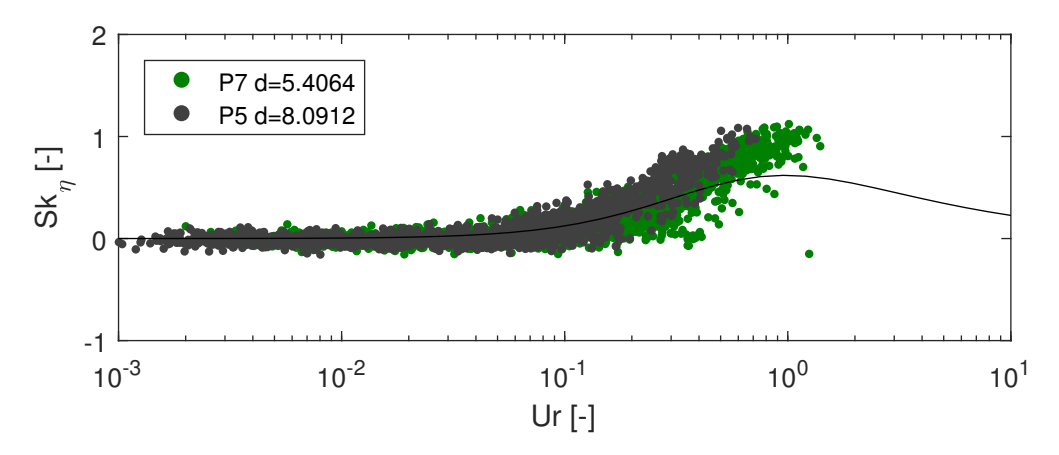


Figure 5.8: Wave skewness versus Ursell number for the pressure sensors 5 and 7. The continuous black line shows the parameterization fit of Ruessink et al. (2012).

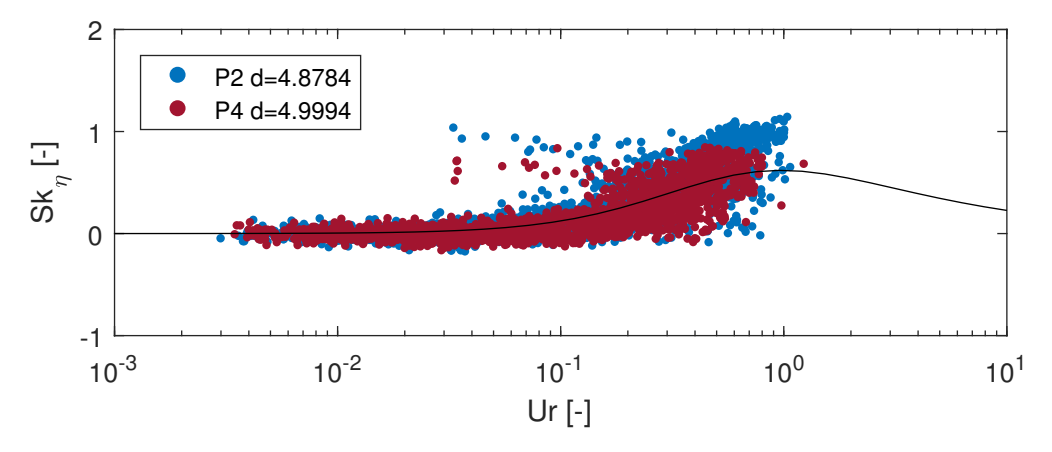


Figure 5.9: Wave skewness versus Ursell number for the pressure sensors 2 and 4. The continuous black line shows the parameterization fit of Ruessink et al. (2012).

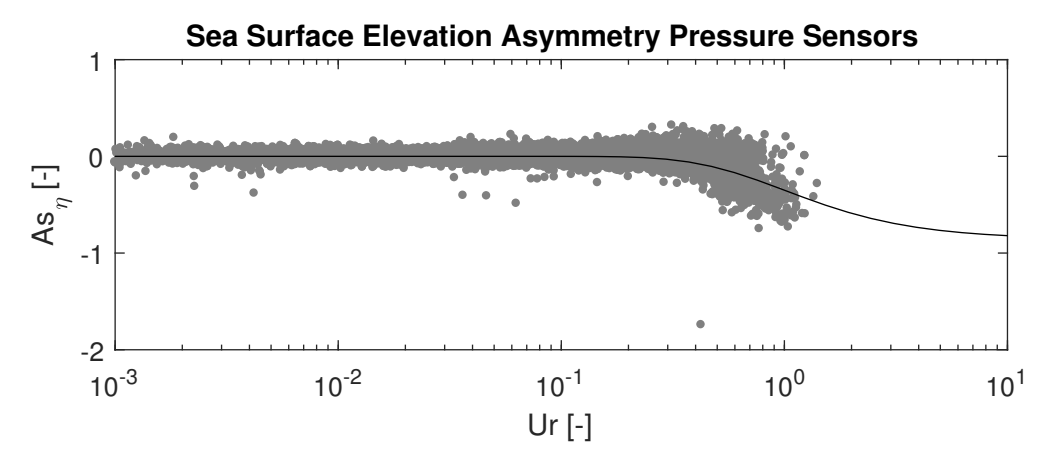


Figure 5.10: Wave asymmetry for frames 4 and 5 and the pressure sensors P1-5 and P7-8. The continuous black line shows the parameterization fit of Ruessink et al. (2012).

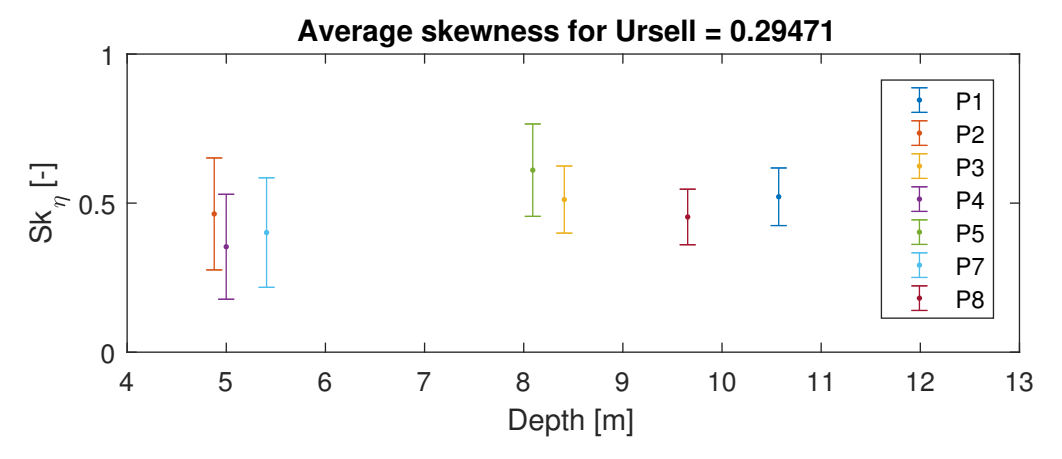


Figure 5.11: The sea surface elevation skewness per pressure sensor for Ursell number =0.3 as a function of the mean water depth. The dots represent the mean in that bin and the vertical lines the standard deviation. Smaller depths shows slightly lower average skewness values but higher standard deviation.

Figure 5.12 show the sea surface elevation skewness and asymmetry for frame 4 with an average depth of 8.02 m and frame 5 with an average depth of 5.01 m. The skewness scatters around 0 for  $U_r$ <0.05. For  $U_r$ >0.05 the skewness increases to maximum of 0.7. It shows that the sea surface elevation skewness is on average below the parametrization. Frame 5 shows slightly higher maximum sea surface elevation skewness,  $Sk_{umax} = 0.87$  compared to frame 4,  $Sk_{umax} = 0.82$ . Furthermore frame 5 shows higher Ursell numbers  $U_r = 0.4$  compared to frame 4,  $U_r = 1.05$ .

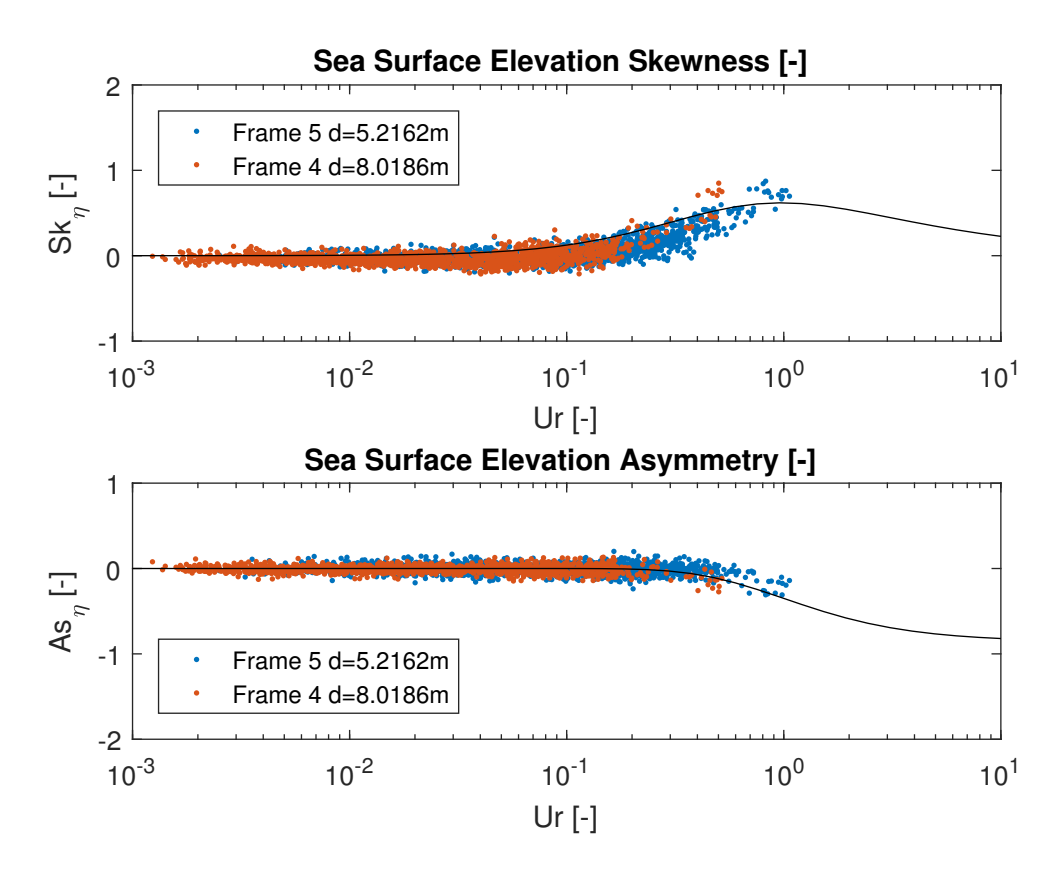


Figure 5.12: Surface elevation skewness plotted against the Ursell number of frame 4 and frame 5. The continuous black line shows the parameterization fit of Ruessink et al. (2012).

## 5.3. Velocity Skewness and Asymmetry

In total 3224 data points are plotted in Figure 5.13, showing the velocity skewness plotted with respect to the Ursell number of frame 4 and 5. The velocity skewness for frame 5 is more scattered than frame 4. For frame 4, 98% of the data points are below  $U_r < 0.1$ , while for frame 5, 40% of the data points are above  $U_r > 0.1$ . For frame 4, the maximum  $U_r$  is 0.4, while the maximum  $U_r$  for frame 5 is 1. In summary, the velocity skewness shows the same behavior as the surface elevation skewness. The wave nonlinearity for frame 5,  $Sk_{umax} = 0.65$ , is higher than for frame 4,  $Sk_{umax} = 0.6$ 

Corresponding to the results of the sea surface elevation asymmetry, there is negligible velocity asymmetry in the ebb-tidal shoal. The velocity asymmetry in Figure 5.13 shows again limited variability and low values. Since both velocity asymmetry and sea surface elevation asymmetry show very low values, the asymmetries are discussed not further. For completeness, the asymmetry values are included in Appendix E.

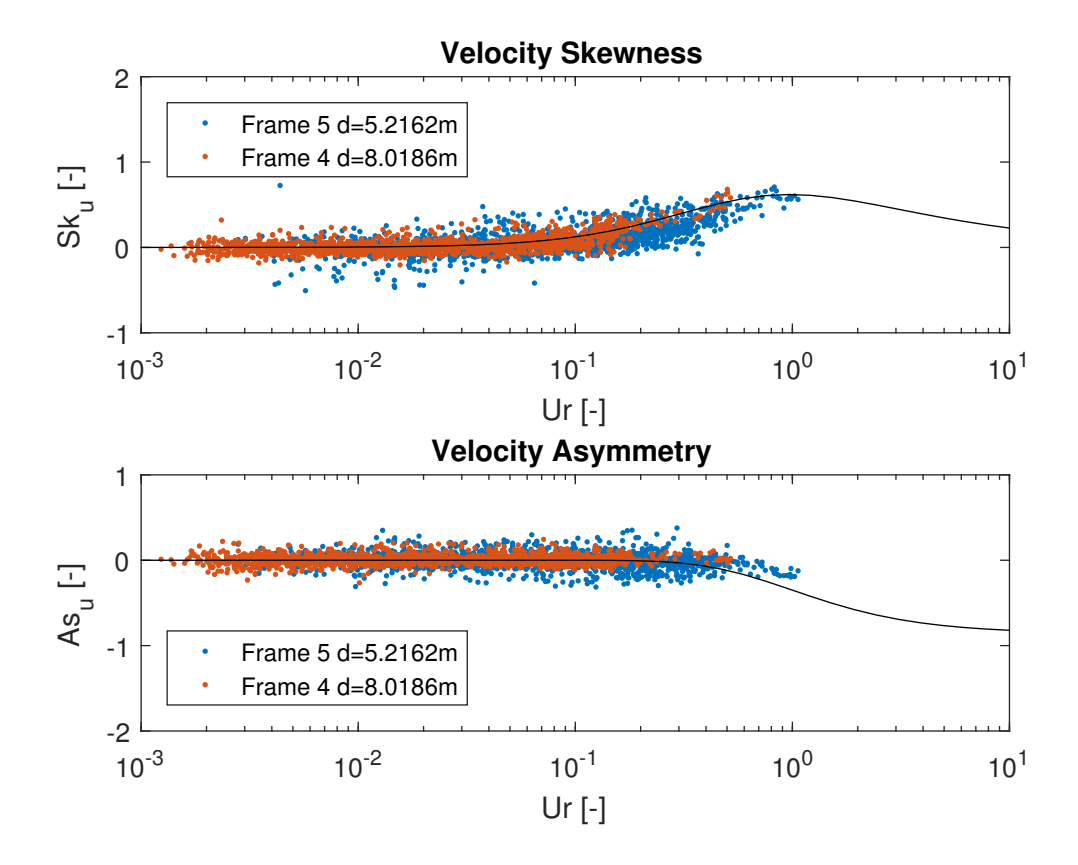


Figure 5.13: Velocity skewness and asymmetry plotted against the Ursell number for frame 4 and frame 5. The continuous black line shows the parameterization fit of Ruessink et al. (2012).

### 5.4. Correlation Sea Surface Elevation and Velocity Skewness

As mentioned earlier, the non-linear wave parameters are used in sediment transport models. Observations show the near-bed velocity skewness should follows the same trend as the sea surface elevation skewness Rocha, Michallet, and Silva (2017). During the field experiment two frames were equipped with both pressure sensors and velocity meters, making it possible to compare the nonlinearity parameters for the sea surface elevation signal and the velocity signal. In this section the correlation between the near-bed velocity skewness and asymmetry and the sea surface elevation skewness is investigated.

The correlation is calculated with the correlation coefficient function in Matlab. This function calculates the correlation coefficient R and the significance value P for null-hypotheses. The correlation is determined by  $R^2$  from 0 to 1, the higher the value of R the higher the correlation. The significance of the correlation is determined by p - value. If p is lower than 0.05, the correlation is significant. A linear polynomial is fitted through the data.

Figures 5.14 and 5.15 show the velocity skewness as a function of the sea surface elevation skewness. For frame 4 the correlation is  $R^2 = 0.7$  and for frame 5 the correlation is  $R^2 = 0.61$ , both significant results. The relationship between the velocity and sea surface elevation asymmetry is negligible due to the fact that the velocity and sea surface elevations show little asymmetry at 5 to 8 m depths.

As the longer waves have a greater influence on the near bed velocity signal, the correlation is checked for longer waves. Once the bursts with a period below 8 s are removed, the correlation for the frame 5 increases to  $R^2 = 0.67$ , while the asymmetry remains weakly correlated. The correlation for frame 4 reduces to  $R^2 = 0.69$  for the longer waves, as shown in Figure E.11. The correlation for both frames is significant.

The sea surface elevation signal can be used to obtain an estimate of the near-bed velocity skewness. However, if the signal contains low asymmetries there is a limited correlation. It is

therefore not reliable to obtain free stream velocity asymmetry from the sea surface elevations asymmetry for our data set.

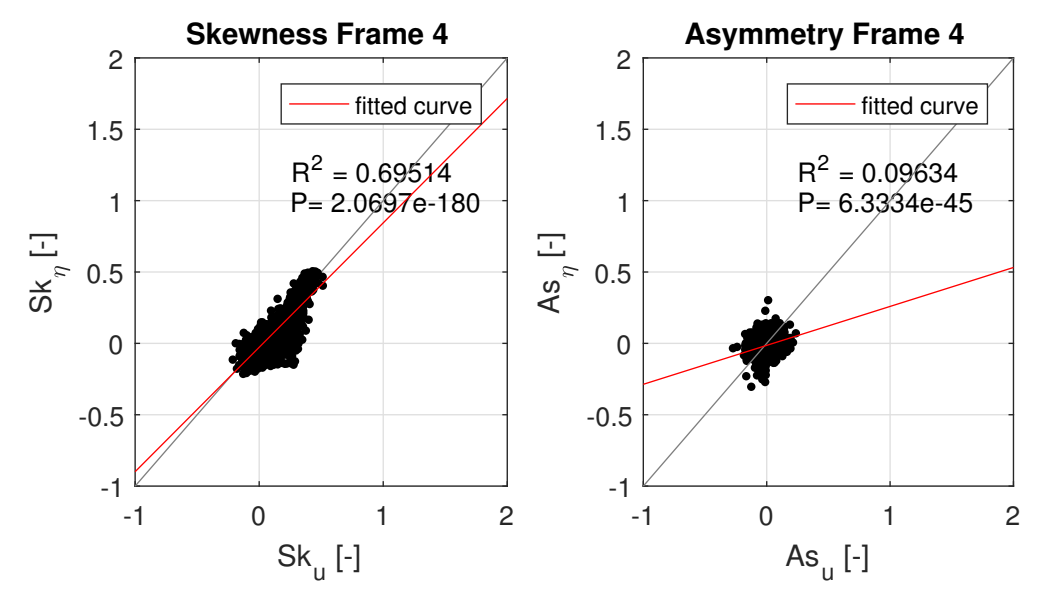


Figure 5.14: Correlation of velocity skewness and sea surface elevation skewness on the left. On the right the velocity asymmetry and wave asymmetry. This data is obtained from frame 4 with a depth of 8.02m.

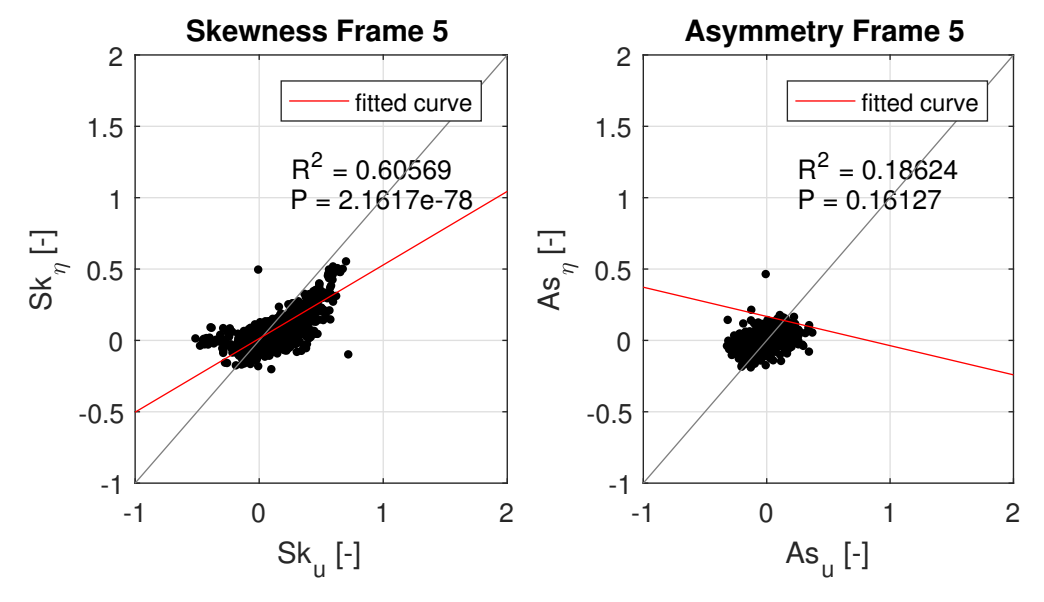


Figure 5.15: Correlation of the velocity skewness and sea surface elevation skewness on the left. On the right the velocity asymmetry and wave asymmetry. This data is obtained from frame 5 with a depth of 5.01m.

### 5.5. Influence of other Parameters on Wave Nonlinearities

In this section different parameters influencing the wave non-linearities are discussed. The larger depth might contribute relative low maximum skewness of frame 4 compared to the shallower frame 5. However, other parameters could influence the variation in the skewness. Directional spreading is addressed in the first in this section. Next, the change in Ursell number is discussed. Finally, the correlation between the Ursell number and skewness in combination with local wave parameters is discussed.

### 5.5.1. Directional spreading on wave skewness

The data shows differences between frames 4 and 5 for both velocity and sea surface elevation skewness. Figure 5.12 shows on average higher values for frame 4 than frame 5 for high Ursell numbers. Directional spread is likely to have influence on the wave skewness (Ruessink, Van Den Berg, & Van Rijn, 2009). In this section the influence of the directions and directional spread of the skewness is investigated. The directional spreading can not be calculated for the pressure sensor data. As a result, directional spreading is only known at the frames. The directional spread in combination with the velocity skewness is discussed.

First, the wave directions differ per frame, as shown in Figure 5.16. The directions per frame are determined with the principle directions from (u, v). The wave spreading is determined by the squared root of the second eigenvector of the total variance. The directional spreading shows larger spreading for frame 4 than frame 5. This spreading is, on average, 5 to 10 degrees larger for frame 4 than for frame 5, and can be up 30 degrees larger.

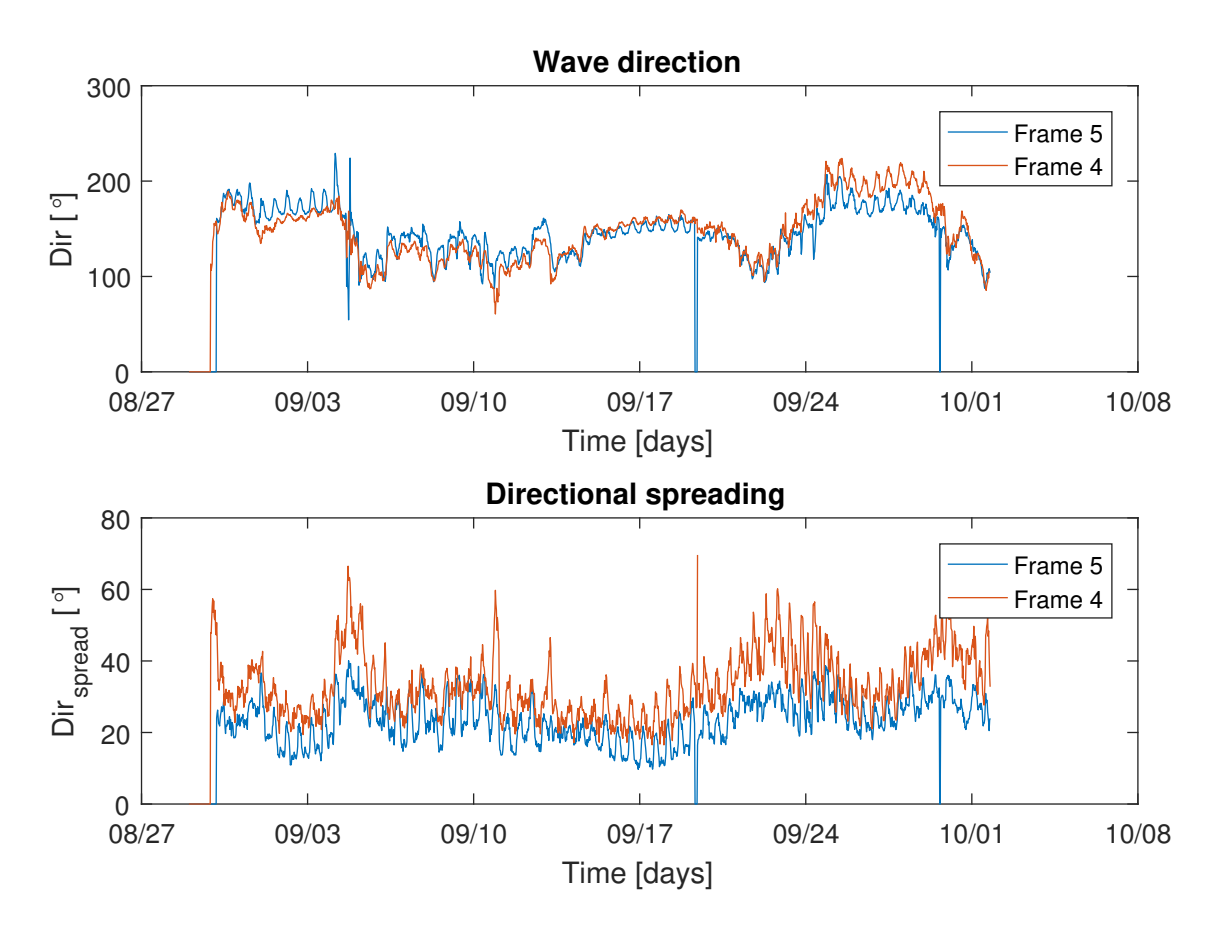


Figure 5.16: Wave directions and spreading for frame 4 (blue) and frame 5(red).

A larger spreading could lead to smaller sea surface elevation and velocity skewness. The relation between the skewness and directional spreading is shown in Figure 5.17. In this case only the values  $U_r > 0.1$  are shown, since this part shows waves with higher nonlinearity. The spreading of frame 4 ranged between 20 degrees and 30 degrees. For frame 5 the spreading

ranged from 10 degrees to 30 degrees. Both frames show a weak negative correlation between the directional spreading and velocity skewness. However, the skewness is weakly correlated to the directional spread, so other factors probably account for the difference in skewness for both frames. Additionally, frame 5 shows considerably more data points, because the frame was in shallower waters. A larger directional spreading would lead to lower skewness values is not proven in our data set.

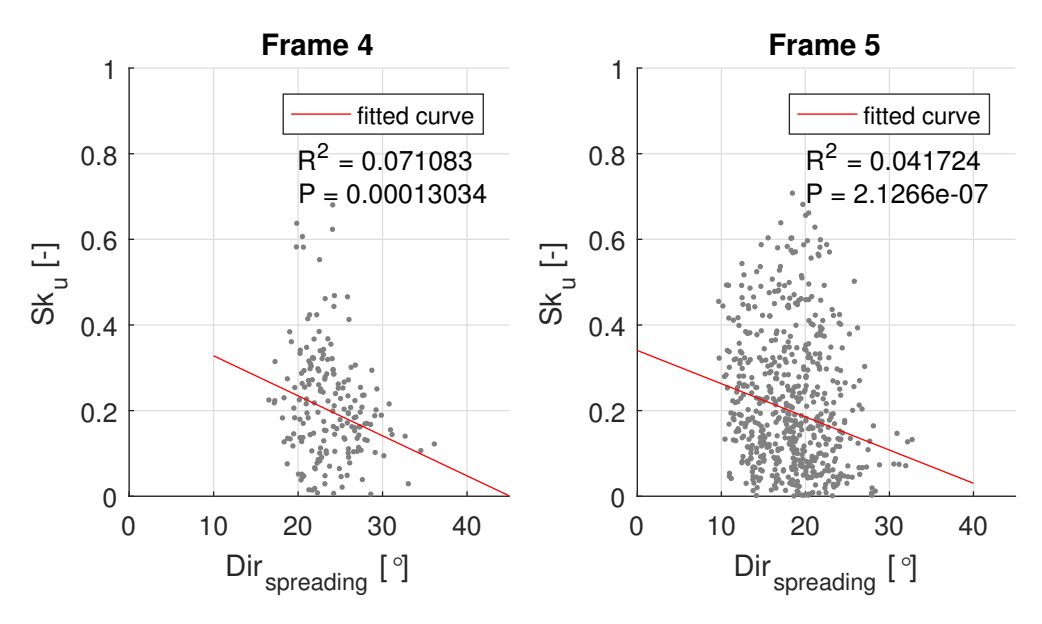


Figure 5.17: Directional spreading per frame 4 and frame 5 as a function of the skewness. The fit (red) and the corresponding correlations between the direction and the skewness.

### 5.5.2. Currents on wave skewness

From the results discussed in previous sections it can be concluded that there is wave skewness in the ebb-tidal delta. However, it is unclear how this skewness develops under a directional flow. The correlation between the free-stream velocity and the sea surface elevations is significant, so the results are combined in this analysis. The distinction between an opposing flow and a following flow on wave non-linearities is made. First, the analysis of the wave skewness with a following and opposing flow is discussed. Afterwards, a comparison of the velocity skewness versus the flow direction is presented.

To investigate the difference in skewness under a following or opposing flow the sea surface elevation skewness of all the pressure sensors and frames is combined and the data of the velocity is combined. Next, the depth-averaged flow in the direction of the waves is obtained with the ADCP. This depth-averaged flow is used to distinguish between an opposing flow or a following flow. The velocity data from the closest frame to estimate the direction of the flow. For pressure sensors P1, P3, and P8 are obtained from the velocity data on frame 4, while for pressure sensors P2, P4, P5, and P7 the velocity data of frame 5 is used.

The sea surface elevation skewness on an opposing flow and a following flow is shown in Figure 5.18. It shows that the surface elevation on an opposing flow has a higher spreading in skewness compared to the surface elevation on a following flow for a given Ursell number. The same behavior can be observed for the sea surface asymmetry, as shown in Figure E.6. In Figure 5.19 the mean and standard deviation of the wave skewness per bin of the Ursell number are shown. The mean skewness for the following flow shows higher values for than for the opposing flow.

Figure 5.20, presents the velocity skewness in relation to on the flow direction; waves opposing the flow or waves following the flow. Since the frames have measured both the flow velocities and the pressure, the local flow velocity and wave direction are used in the comparison. Figure 5.21 shows that the velocity skewness is below the fit. By looking at the mean and standard deviation of the skewness of Figures 5.21 the same trend is noticeable

as for the sea surface elevation skewness. The following flow has on average a higher value than the opposing flow. Although, the mean is in the bandwidth of the error.

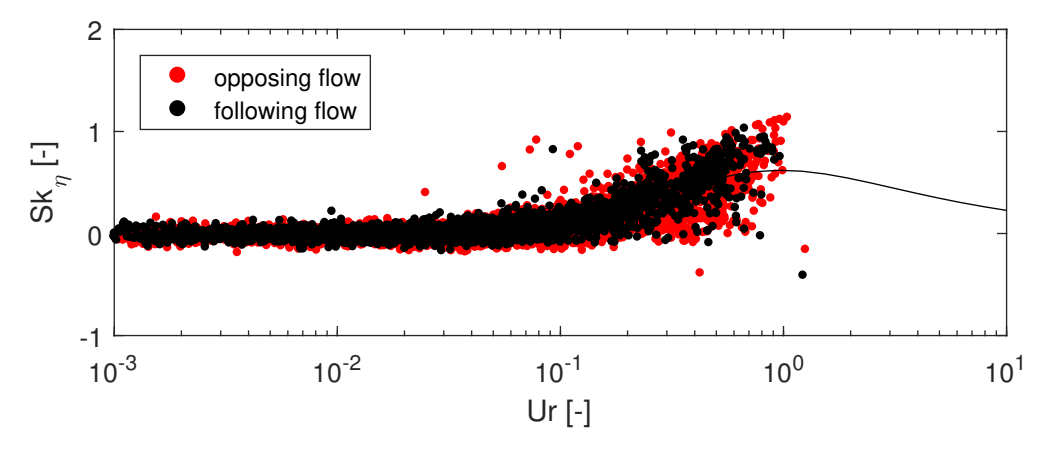


Figure 5.18: The sea surface elevation skewness of the opposing and following flow. The red dots represent the opposing flow, while the black dots represent the following flow. The continuous black line shows the parameterization fit of Ruessink et al. (2012).

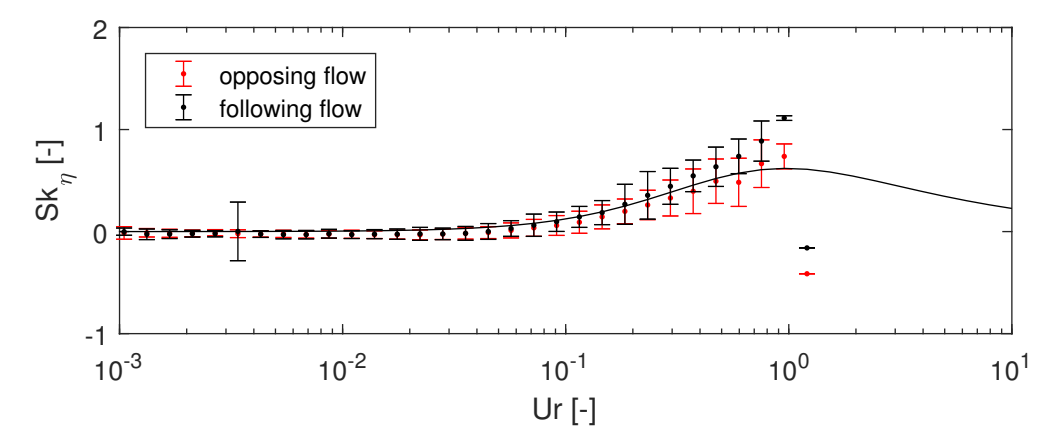


Figure 5.19: Ursell number versus the sea surface elevation skewness in an opposing (red) and following (black) flow. The dots represent the mean per bin, with a bin width of  $Ur = 10^{0.05}$ . The vertical lines represent the standard deviation in each bin. The continuous black line shows the parameterization fit of Ruessink et al. (2012).

Opposing flow and following flow is determined whether the sign of the velocity wave positive (following) or negative (opposing). Since it is likely that higher flow velocities influence waves and velocity to a greater extend, a threshold is applied in the depth-averaged flow velocities of |u| > 0.1 m/s. Afterward the mean per bin, with a width of  $U_r = 10^{0.05}$ , is compared with the Ruessink fit in case of a threshold and no threshold. The negative values imply the measured skewness is above the fit of Ruessink and positive values vise versa. Zero means that the measured values match the parameterization.

In sea surface elevation skewness shows clear difference between the opposing and following flow in Figure 5.22. For  $U_r > 0.07$  skewness starts to show divergence of from fit. The negative values in the plot suggest that the measured sea surface elevation skewness is larger than the skewness predicted by the parameterization. The applied threshold increases the skewness for an opposing flow. This trend is observed in the following flow.

The velocity skewness, as shown in Figure 5.5, shows a better fit with the parameterization than the sea surface elevation. For  $U_r > 0.1$  skewness starts to show divergence from the fit. Again, the skewness increases with the applied threshold for both opposing and following flow. Nevertheless, the separation between an opposing and following flow is not that obvious. Concluding in our data an increasing flow increases skewness.

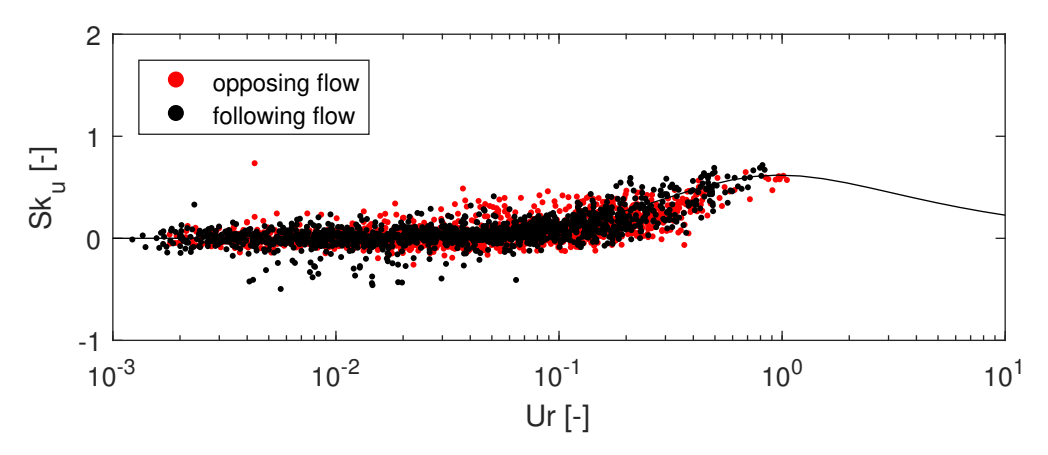


Figure 5.20: The velocity skewness of the opposing and following flow. The red dots represent the opposing flow, while the black dots represent the following flow. The continuous black line shows the parameterization fit of Ruessink et al. (2012).

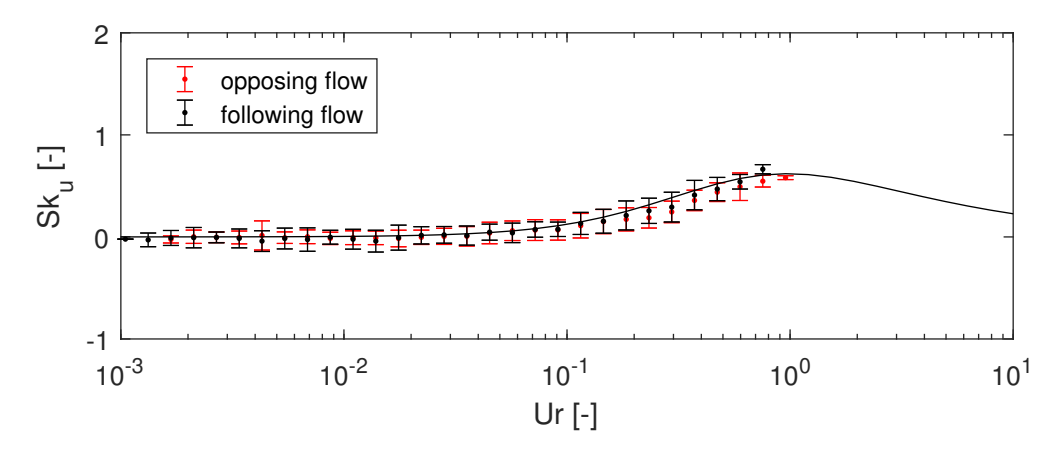


Figure 5.21: Ursell number versus the velocity skewness in an opposing (red) and following (black) current. The dots represent the mean per bin, with a bin width of  $Ur = 10^{0.05}$ . The vertical lines represent the standard deviation in each bin. The continuous black line shows the parameterization fit of Ruessink et al. (2012).

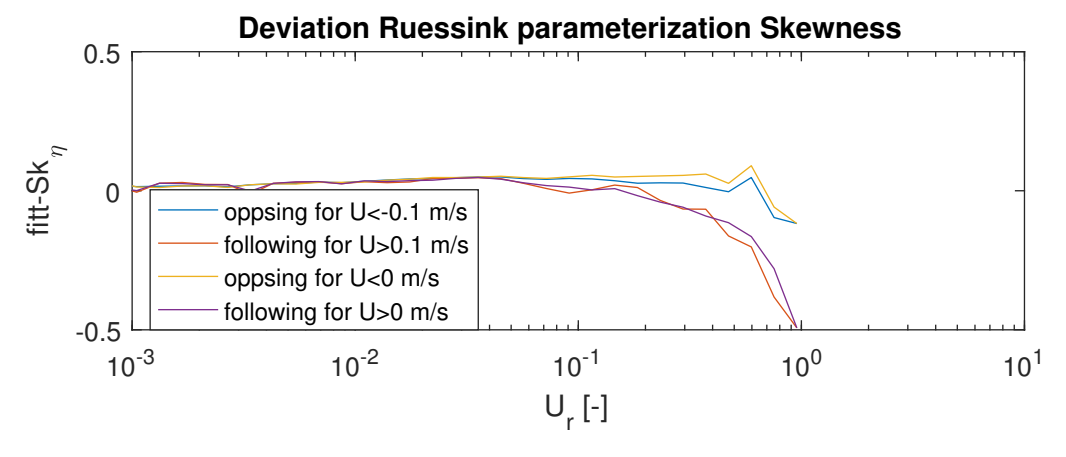


Figure 5.22: Deviation from the Ruessink fit for the sea surface elevation skewness. In both opposing and following flow directions with/without depth averaged velocity threshold of u >= +/-0.1..

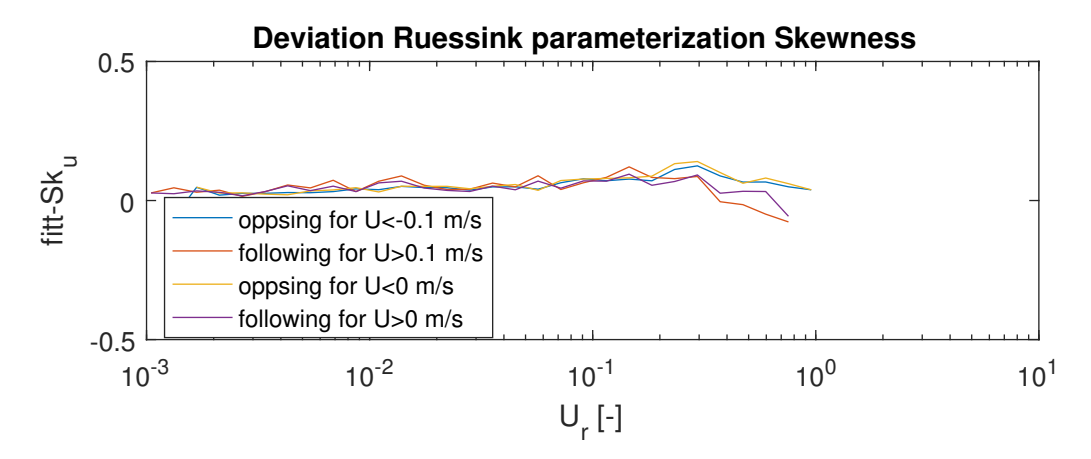


Figure 5.23: Deviation from the Ruessink fit for the velocity skewness. In both opposing and following flow directions with/without depth averaged velocity threshold of u >= +/-0.1.

### 5.5.3. Local wave parameters on wave skewness

Over the duration of the field experiment variations in wave conditions, wave period, and currents occurred. As discussed before, the flow direction has an influence on the value of the skewness. But several other parameters could also contribute to the correlation between the Ursell number and wave skewness. In this section, possible influences on the correlation between the wave skewness and the Ursell number are investigated.

In Figure 5.24, the correlation between the velocity skewness and the Ursell number is plotted. The correlation between the Ursell number and the skewness is obtained by using a moving correlation over the data set. The correlation is calculated over 12 bursts, so in total 6 hours. If the significance of the correlation is limited, if p > 0.05 the correlation does not give a number. Even around September 6 and around September 24, a very weak correlation occurs. In this period there are relatively low waves, around 0.25 m. This overall correlation shows that the wave skewness and Ursell number is relatively high for high waves and high periods. Around September 3, September 8 and September 13 to 17 there is a high correlation  $R^2 > 0.6$ . Over the course of this period the significant wave height is 1.1 m, 1.7 m and ranged from 2 m up to 4m, respectively

From the figure it can be observed that the correlation increases with a rising peak period. During low peak period the correlation decreases. Especially after September 24, the correlation is weak. This could be due to the fact that there are both low peak periods and low significant wave heights, which results in low Ursell numbers.

Concluding form this, the correlation between the skewness and Ursell number is significant and is correlated with the wave height and wave period increases. For low periods and low wave height the parameterization shows limited correlation so is less reliable.

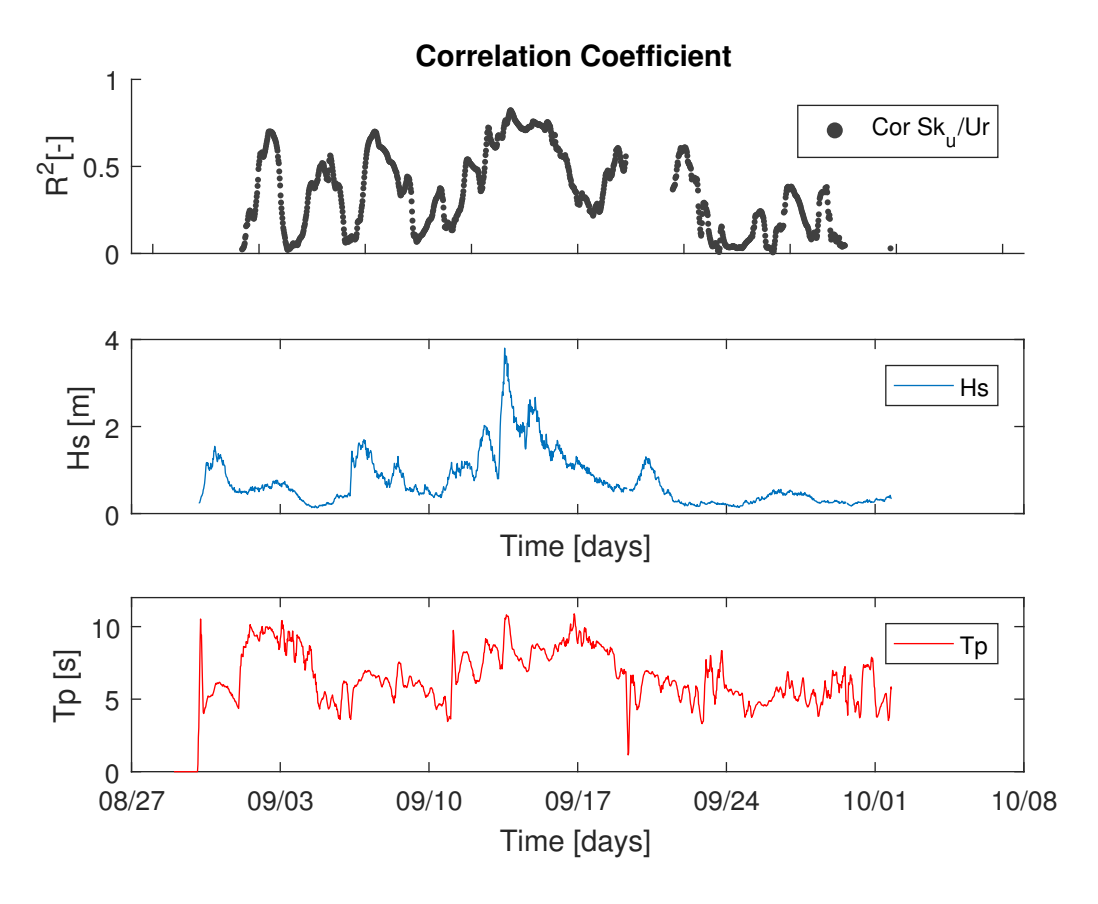


Figure 5.24: Correlation of skewness with Ursell number. The significant wave height (blue) and averaged peak period (red) over 6 bursts.



# Discussion

The discussions interprets and describes the significance of the results obtained in Chapter 5.

### 6.1. Link to Literature

The purpose of this research was to determine if wave skewness occurs in the ebb-tidal delta northwest of Ameland. The correlation between velocity and sea surface nonlinearities are discussed. In addition, the influence of the flow on the parameterization of the waves is investigated. These results are discussed and compared to previous literature.

### 6.1.1. Skewness in the vicinity of tidal inlet

First conclusion drawn in the Ameland ebb tidal delta wave skewness is induced. In literature the change wave height under influence of flows in tidal inlets have been studies extensively. Battjes (1982) studies the wave height variation of a tidal entrance of the Oosterschelde estuary, including wave breaking on the shoals in the estuary delta. Dodet et al. (2013) was interested in the wave-current induced changes in wave propagations at the Albufeira lagoon. The interaction of an offshore front of a river plume with wave breaking is discussed by Thomson, Horner-Devine, Zippel, Rusch, and Geyer (2014). However, to the best of my knowledge, no interest is taken into how a current changes the wave skewness in field observations. Only in the change in wave height and wave period.

As indicated in section 5.1 the skewness varies with the tide. The variations might come from the changes in depth and/or the current due to the tides. However which mechanism is dominant in which case in not completely clear. In one case the skewness is maximum at the lowest water level and zero flow. While other case shows that the skewness is just after maximum following flow and just before high water. This means that other factors might be dominant in the skewness, like the wave height, wave period. It is likely that for example a flow has more influence on high waves and waves with a longer period, because the wave orbital velocities penetrate deeper in to the water column.

### 6.1.2. Correlation wave skewness and asymmetry

Velocity skewness is found to have a strong correlation with the sea surface elevation skewness. The correlation is stronger than for the shallower frame. Asymmetry shows a weak correlation between the sea surface elevation and the velocity.

For sediment transport, the key feature is the wave shape, particularly skewness and asymmetry. Skewness and asymmetry are statistical measures of horizontal and vertical asymmetry of the wave form. From a practical point of view, it would be beneficial to obtain the velocity non-linearities from the sea surface elevation. Since a pressure sensor is easier deployed in the field than a velocity meter.

A literature review, showed that velocity skewness and asymmetry can be estimated from measurements of the surface elevation in the near-shore area. Michallet, Cienfuegos, Barthélemy,

42 6. Discussion

and Grasso (2011) showed that for irregular waves the velocity and sea surface elevation skewness and asymmetry follow the same trend but the absolute values are clearly different. Since velocity nonlinearities and sea surface nonlinearities follow the same trend, the velocity time series may potentially be retrieved from the sea surface elevation.

Rocha et al. (2017) found the same behavior and differences between the observed Sk and As. Although,  $Sk_u$  and  $As_u$  showed smaller absolute values. The difference between the absolute values can be up to 40%. Rocha et al. (2017) proposed that the lower values of  $Sk_u$  and  $As_u$  are the result of the depth attenuation of high frequencies velocities in the water column, since these frequencies make a major contribution to the skewness. These finding contradict our data, since the correlation between the sea surface elevation skewness and the velocity skewness is in favor of the velocity skewness. Rocha et al. (2017) showed higher sea surface elevation skewness than the velocity skewness. A possible explanation might be that linear wave theory under estimates the nonlinear wave form.

The asymmetry shows little correlation. Since the values of the asymmetry scatter around 0 and are very small, the correlation is not significant. The limited asymmetry is due to the depth, since asymmetry arises just before wave breaking. The water depth and/or the magnitude of the flow, compared to the wave celerity, is to low so that waves do not break yet.

### 6.1.3. Directional spreading

The directional spreading is not significantly correlated to the skewness. This analysis is done to understand the difference in velocity skewness near the frames. However, the directional spread of frame 4 is higher for frame 5 for the same Ursell numbers.

Ruessink et al. (2012) compared two data sets, sea wave and sea swell wave, with directional spreading to determine the difference skewness values for the  $0.75 > U_r > 2$ . Skewness is adapted under influence of the directional spread, because the directional spread influences the energy transfer from the primary wave to the higher harmonics. Since skewness is a measure of the amount of higher harmonics in the signal (Ruessink et al., 2012), the directional spread influences the skewness negatively.

First, as directional spread is not significant correlated to the skewness, other factors, wave period, wave height, are more likely to contribute to the on average higher skewness values for frame 4 if the  $U_r > 0.1$ . This phenomena was also found by Eldeberky and Battjes (1996), where the interacting waves have little effect on the frequency spectra. In other words the skewness it little influenced by the directional spread.

The difference between the frames might not be contributed to the directional spreading. A possible explanation could be the depth, since the depth at frame 5 is lower, higher Ursell numbers occur.

### 6.1.4. Parameterization on ebb-tidal shoal in the presence of a current

Parameterization of the nonlinearity parameters to estimate skewness and asymmetry developed by Ruessink et al. (2012) aims to derive them from local wave parameters, namely significant wave height  $H_s$ , peak period  $T_p$  and water depth h. This parameterization was developed for waves in the near shore zone and not in the presence of a flow. The data obtained during the SEAWAD experiment in the ebb tidal delta under influence of a flow fits the parameterization line well.

The parameterization of skewness and asymmetry developed by Ruessink et al. (2012) for near shore regions is found to preform well in the ebb-tidal delta near Ameland. Therefore, the wave height shows slightly higher values for a following flow than for a opposing flow. From this we can conclude that sea surface elevation skewness is influenced by the tidal flow. In the velocity skewness this trend is less obvious.

In literature, numerically Chen, Member, Madsen, and Basco (1999) concluded that an opposing current will reduce the Ursell number, the beat-length and the ratio of the energy of the higher harmonics to the primary harmonic in shallow water. It diminishes the triad interaction for opposing current, while for following flow the energy transfers intensifies. This indicated that an opposing current may reduce the degree of asymmetry and skewness of shoaling waves Chen et al. (1999). This is only applicable in near resonant triad interactions

6.1. Link to Literature 43

in limited water depths and valid in the nearshore. However, this reasoning agrees with the found results in the field experiment where the opposing flow limits the skewness and following flow increases the skewness.

### 6.1.5. Adapting Ursell number

In all the results, the linear wave theory is applied to calculate parameters such as peak period, wave height, and the Ursell number. The Ursell number is applied in the parameterization of Ruessink, however a flow could have influence on  $U_r$ . The Ursell number is dependent on the water depth, wave period and wave height. In the parameterization the absolute period is used to calculate k, however flow modulates the frequency. The governing equation is explained in Chapter 2.

In the Appendix E the effect of changing from absolute to intrinsic frequency on the wave number is explained. From this, it was concluded that an increasing opposing flow would increase the wave number, and for an increasing following flow, the wave number would decrease. The influence on the wave number is that for a stronger opposing current, the Ursell number would decrease and with stronger following flow, the Ursell number would increase.

In the analysis of applying linear wave theory with current (see Appendix D), the depth-averaged flow was used in linear wave theory to calculate the wave heights, skewness and asymmetry. It was found that significant wave heights show unrealistically high values for an opposing current. While, the skewness was hardly affected by the flow. In calculating the Ursell number, the significant wave height is calculated with linear wave theory without currents. While for calculating the wave number k, the intrinsic frequency is used. In the parameterization, the Ursell number with or without currents is applied.

Wave parameter, k, is calculated with linear wave theory with and without currents. Figure 6.1 mean and standard deviation of the skewness per bin, with a bin width of  $10^{0}.05$ , for following flow. The result show the sea surface elevation skewness plotted with respect to the Ursell number for linear wave theory with and without currents. The change of Usrell number has little influence on mean sea surface elevation skewness for opposing flow, as shown in Figure 6.1.The standard deviation is changed slightly changed for  $U_r > 0.08$ . As described above, the sea surface elevation with respect to the Ursell number for opposing flow is plotted in Figure 6.2. The means and the standard deviation shows only slight variations. Only for Ursell number around 1, the change is notable from Figure 6.2. This is probably the result of the limited amount of data points in that bin.

The analysis is done likewise for the velocity skewness. Again the velocity skewness is plotted again the Ursell number, calculated with and without currents applied in linear wave theory. The following flow conditions are presented in Figure 6.3. The Figure shows that the mean is slightly changed to higher values, especially bins for  $U_r$  ranged from 0.1 to 0.3. The standard deviation also changed substantially in that range. For  $U_r > 0.3$  the mean is not changed. Opposing flow shows other behavior, as shown in Figure 6.4. the Figure shows that the mean is slightly changed to higher values, especially for the bins  $U_r$  ranged from 0.07 to 0.1. The standard deviation remained the same. In Appendix E, the results of the linear wave theory with and without currents are presented.

The sea surface elevation shows a limited shift of the mean and standard deviation when comparing both opposing and following flow to the initial condition. The sea surface elevation shows a minimal shift of both opposing and following flow towards higher skewness. The velocity skewness shows a shift towards higher skewness for opposing flow, while for following flow the values does not show a clear shift. One of the reasons could be the limited amount of data points for the higher Ursell numbers.

From the limited change of the mean and standard deviations, it can be concluded in that Ursell number, seems to describe the waves in flow environment well. Even if, the currents are not included in the linear wave theory.

44 6. Discussion

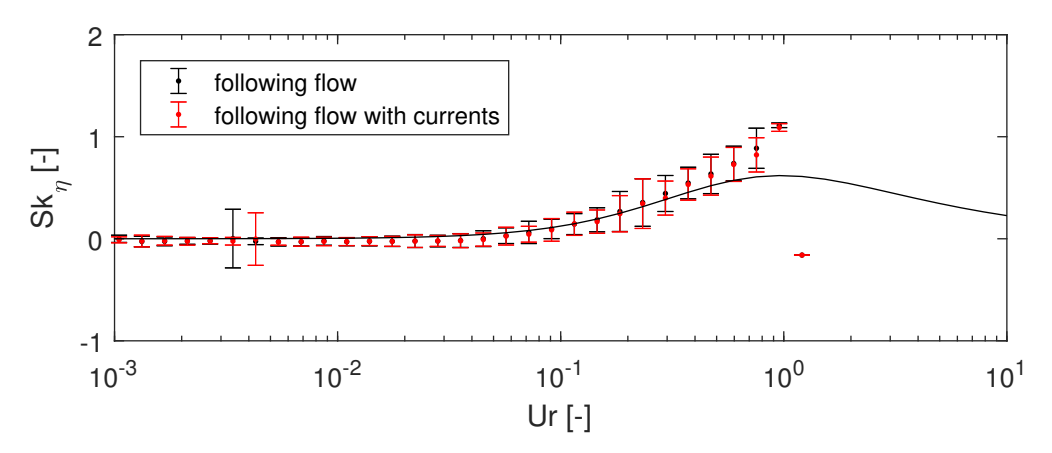


Figure 6.1: Sea surface elevation skewness under a following flow. Results for Ursell number calculated with linear wave theory without currents (black) and Ursell number calculated with linear wave theory with currents (red). The points represent bin means, with a bin width of  $10^{0.05}$ , and the lines show the standard deviation. The black lines shows the parameterization fit of Ruessink et al. (2012).

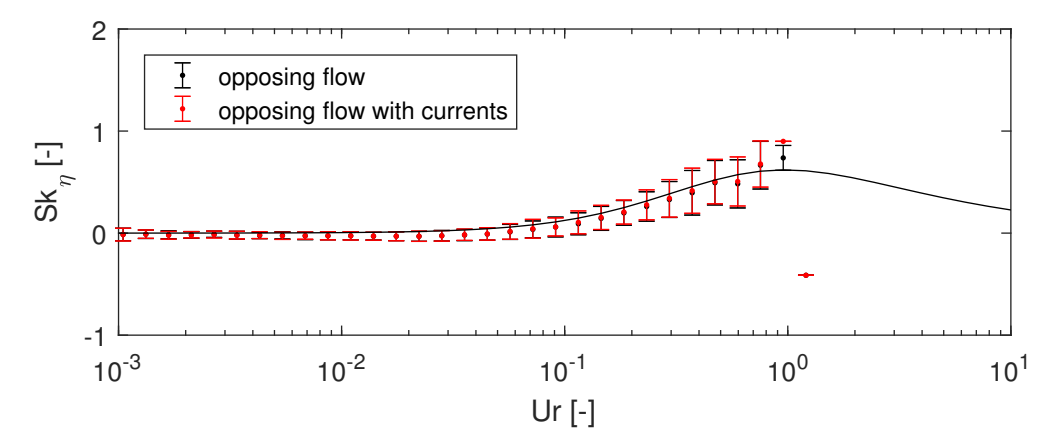


Figure 6.2: Sea surface elevation skewness under opposing flow. Results for Ursell number calculated with linear wave theory without currents (black) and Ursell number calculated with linear wave theory with currents (red). The points represent bin means, with a bin width of  $10^{0.05}$ , and the lines show the standard deviation. The black lines shows the parameterization fit of Ruessink et al. (2012).

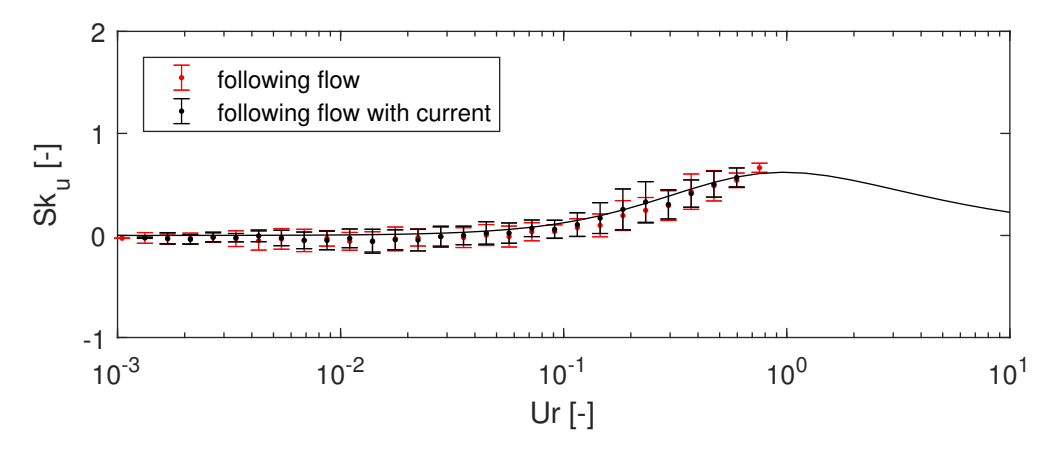


Figure 6.3: Velocity skewness under following flow. Results for Ursell number calculated with linear wave theory without currents (black) and Ursell number calculated with linear wave theory with currents (red). The points represent bin means, bins with a bin width of 10<sup>0.05</sup>, and the lines show the standard deviation. The black lines shows the parameterization fit of Ruessink et al. (2012).

6.2. Practical relevance 45

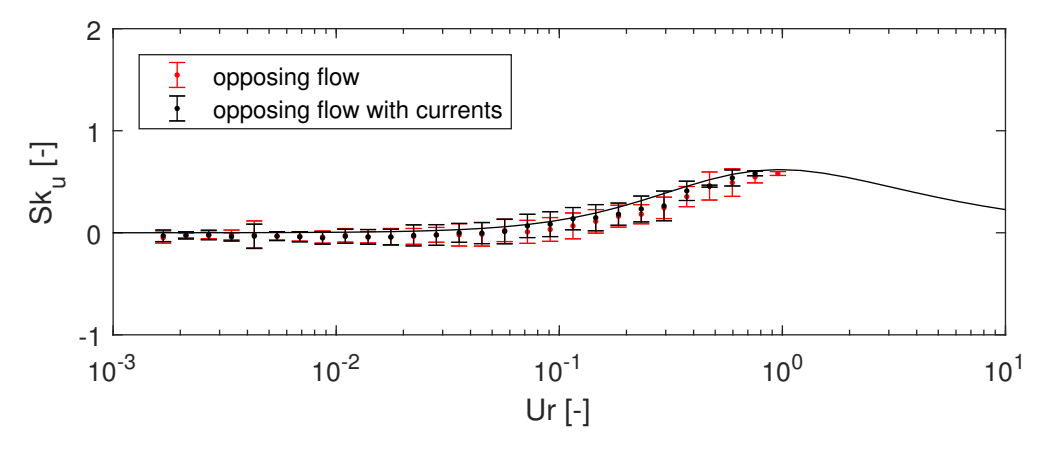


Figure 6.4: Velocity skewness under opposing flow. Results for Ursell number calculated with linear wave theory without currents (black) and Ursell number calculated with linear wave theory with currents (red). The points represent bin means, with a bin width of  $10^{0.05}$ , and the lines show the standard deviation. The black lines shows the parameterization fit of Ruessink et al. (2012).

### 6.2. Practical relevance

In order to accurately predict sediment transport, many morphological models use simple parameterization of the near-bed velocity motions. Several parameterizations methods are proposed by Drake (2001) and Elfrink, Hanes, and Ruessink (2006b). Limitations of these parameterizations include the limited amount of harmonics considered or unrealistic acceleration. Ruessink et al. (2012) developed parameterizations obtained from local wave parameters, which are a common output in morphodynamic models. Current parameterizations methods (Drake (2001), Elfrink et al. (2006b) and Ruessink et al. (2012)) have been developed for the nearshore zone. This research found that this parameterization of Ruessink et al. (2012), was working well on an ebb-tidal shoal. The applicability of the parameterization extends to a wider area now. This broader applicability of the parameterization could be used in morphological models. Finally, this will help to better predict morphological changes in cases of nourishments or changes in the ebb-tidal delta.

### 6.3. Limitations

This study has some limitations regarding the use of the parameterization of Ruessink et al. (2012).

Firstly, frames were in too deep water. Especially since, there are a limited number of data points for both velocity skewness and sea surface elevation skewness. The relationships found for the skewness are limited to the low Ursell numbers. To further improve the understanding of flow interaction with waves, shallower zones should be investigated. In particular, the highest values of the nonlinearities are expected to have a larger influence on sediment transport than the smaller values of nonlinearities.

Secondly, the bulk parameters in the presence of a depth-averaged flow are studied in this particular study. The effect of flow on the wave shape is not clearly quantified. The underlying mechanism of how a non uniform flow influences the wave shape and accounted underlying mechanisms are not quantified. In literature this wave current interaction is studies with numerical models by Chen et al. (1999). It has never been validated in field or lab experiments.



# Conclusions & Recommendations

In this section the conclusions regarding the research questions are presented and recommendations for further research are given.

### 7.1. Conclusion

The main objective of this research is to determine if a flow has influence on the wave shape. Distinctions between the near-bed velocity- and sea surface elevation nonlinearities can be made. The research questions were defined as follows:

- Are wave non-linearities influenced by the tidal flow on a ebb-tidal shoal?
- What is the correlation between the surface elevation skewness and near-bed velocity skewness?
- What is the relationship between skewness and asymmetry with respect to the Ursell number in case of tidal flow?

Through the data collected during SEAWAD field experiment these questions were studied. In the following sections each research question is answered.

### 7.1.1. Nonlinearity on the ebb-tidal shoal

In the ebb-tidal delta northwest of Ameland skewness and asymmetry occur. In the shallower area, waves show more nonlinear behavior. The skewness and velocity is partly dependent on the water depth, but also on the wave height. With higher significant wave height, wave skewness and asymmetry parameters increase. The wave skewness fluctuates with the tide.

### 7.1.2. Correlation nonlinear parameters

The correlation between the near-bed velocity skewness and the sea surface elevation skewness is larger than  $R^2 = 0.6$ . The correlation for the shallower frame is strongly dependent on the wave length of waves. For waves with a peak period  $T_p$  higher than 8 seconds the correlation increases to  $R^2 = 0.69$ , while correlation for the deeper frame remains around  $R^2 = 0.69$ . The sea surface elevation skewness can be used to give an estimate of the near-bed velocity skewness. The asymmetry, on the other hand, shows limited correlation with the velocity and the sea surface elevation, since in this area few asymmetric waves are present.

### 7.1.3. Parameterization of skewness & asymmetry

The method of computing the velocity skewness from the representative wave height, wave period and water depth, developed by Ruessink et al. (2012), is used at an ebb tidal shoal. The bulk wave parameters are used to compute the nonlinearity parameters, such as skewness and asymmetry. This parameterization for developed for near shore conditions preforms well

on ebb tidal delta. The parameterizations preforms well for relative high waves with long periods.

The tidal flow influences the development of the nonlinearities. The skewness values are larger for waves on a following flow, than the skewness values on an opposing flow. This distinction is higher for the observed for sea surface elevation skewness than for the velocity skewness.

### 7.2. Recommendations

Based on this research recommendations can be made to improve future research. First the instrumentation in the field campaign is discussed. Next, the methodology used in the analysis and the recommendations based on the further research are discussed.

#### 7.2.1. Instrumentation

Although wave measurement with subsurface pressure sensors has advantages, a disadvantage is the indirect measurement of the surface waves. Linear wave theory is commonly used to obtain the surface elevation from a pressure signal. However, this method underestimates the nonlinearities in the waves according to Bonneton and Lannes (2017a). Especially when the nonlinearities are of importance for the understanding of sediment transport, a direct measurement of the surface elevation is preferred.

### 7.2.2. Methodology

In the transformation of the pressure to sea surface elevation linear wave theory is used. As discussed above, linear wave theory has some drawbacks in recovering sea surface elevation. In the studied environment currents play a major role. However, currents are not included in the recovering of the sea surface elevation the wave are underestimated for opposing flows and overestimated for following flows. An analysis of the linear wave theory with currents it is seen that the wave height was unrealistically high for high opposing flows. The depth-averaged flow could contribute to the unrealistically high wave parameters. To get more realistic results the velocity distribution over the vertical should be used instead of the depth-averaged flow, since the wave is affected by the shape of the velocity profile.

An other method for obtaining sea surface elevation, developed Bonneton and Lannes (2017b), is evaluated. In this method, a drawbacks are the dependence on cut-off frequency, which has a major influence on the non-linearity parameters. In order to use this method with confidence, a more descriptive way should be found in using the cut-off frequency and its transfer function.

#### 7.2.3. Further research

This study contained the observations of the SEAWAD field experiment. Topics of further research are related to better understanding of the development of skewness and asymmetry under a flow. A better understanding on the energy transfer between the currents and waves occurs would be of importance for the hydrodynamic parameters and finally included in hydrodynamic models. Especially for the skewness and asymmetry parameters, since these are important parameters for sediment transport. Numerical experiments on wave-current interaction on skewness are already done, but not yet verified in the field of lab.

2.1	Wave-current amplification factor $a/a_0$ the wave height compared to the deepwater wave height as a function of $U$ in the direction of the wave propagation. Case (1) is with vertical upwelling from below, Case (2) is with horizontal inflow from the sides. Longuet-Higgins and Stewart (1961)	4
2.2	Wave propagation under influence of the bottom. The wave shape first becomes positively skewed and then before wave breaks, the wave shape becomes asymmetric ( <i>LEGI - UMR 5519 - Nonlinearities of waves propagating over a mild-slope</i>	
2.3	beach: laboratory and numerical results, n.d.)	9
2.4 2.5	Vertical velocity profile with irregular bottom. ()	10 12
	Area of interest (Elias & van Oeveren-theeuwes, 2016). The colors indicate depth, with blue for the deeper areas, and red for shallower areas Orientation of pressure sensors (green) and frames (red)	13 14 15 16 16
4.1 4.2 4.3	Overview of data processing steps	19 21 22
	The significant wave height versus the sea surface elevation or velocity skewness. The linear fit is positively increasing with significant correlations. Thus the skewness is likely to increase with increasing significant wave height	24
5.2	The peak period versus the sea surface elevation or velocity skewness. The linear fit is positively increasing with significant correlations. Thus the skewness is likely to increase with wave period	24
5.3	Overview of wave and velocity skewness and asymmetry over the duration of the field campaign for frame 4 (red) and frame 5 (blue). From top to bottom; significant wave height, velocity skewness and asymmetry, sea surface elevation skewness and asymmetry, Ursell number, water depth, and velocity in the direction of the wave (ADV 2 and ADV 11), depth-averaged flow in the direction	
	of the waves (ADCP)	25
	Case 1) Skewness, depth-averaged velocity and water level of frame 5 from the 2th of September until the 5th of September.	26
5.5	Case 2) Skewness, depth-averaged velocity and water level of frame 5 from the 16th of September until the 19th of September	26
5.6	Wave skewness for frames 4 and 5 and the pressure sensors P1-5 and P7-8. For the low Ursell numbers the scatter is low, with a higher Ursell number the scatter increases. The continuous black line shows the parameterization fit of	
	Ruessink et al. (2012).	27
5.7	Wave skewness versus Ursell number for the pressure sensors 1,3,8. The continuous black line shows the parameterization fit of Ruessink et al. (2012).	28

5.8	Wave skewness versus Ursell number for the pressure sensors 5 and 7. The continuous black line shows the parameterization fit of Ruessink et al. (2012).	28
5.9	Wave skewness versus Ursell number for the pressure sensors 2 and 4. The continuous black line shows the parameterization fit of Ruessink et al. (2012).	28
5.10	Wave asymmetry for frames 4 and 5 and the pressure sensors P1-5 and P7-8. The continuous black line shows the parameterization fit of Ruessink et al. (2012)	29
5.11	The sea surface elevation skewness per pressure sensor for Ursell number =0.3 as a function of the mean water depth. The dots represent the mean in that bin and the vertical lines the standard deviation. Smaller depths shows slightly lower average skewness values but higher standard deviation	29
5.12	Surface elevation skewness plotted against the Ursell number of frame 4 and frame 5. The continuous black line shows the parameterization fit of Ruessink et al. (2012).	30
5.13	Velocity skewness and asymmetry plotted against the Ursell number for frame 4 and frame 5. The continuous black line shows the parameterization fit of Ruessink et al. (2012).	31
5.14	Correlation of velocity skewness and sea surface elevation skewness on the left. On the right the velocity asymmetry and wave asymmetry. This data is obtained from frame 4 with a depth of 8.02m.	33
5.15	Correlation of the velocity skewness and sea surface elevation skewness on the left. On the right the velocity asymmetry and wave asymmetry. This data is obtained from frame 5 with a depth of 5.01m	33
5.16	Wave directions and spreading for frame 4 (blue) and frame 5(red)	34
	Directional spreading per frame 4 and frame 5 as a function of the skewness. The fit (red) and the corresponding correlations between the direction and the skewness.	35
5.18	The sea surface elevation skewness of the opposing and following flow. The red dots represent the opposing flow, while the black dots represent the following flow. The continuous black line shows the parameterization fit of Ruessink et al. (2012).	36
5.19	Ursell number versus the sea surface elevation skewness in an opposing (red) and following (black) flow. The dots represent the mean per bin, with a bin width of $Ur = 10^{0.05}$ . The vertical lines represent the standard deviation in each bin. The continuous black line shows the parameterization fit of Ruessink et al. (2012)	36
5.20	The velocity skewness of the opposing and following flow. The red dots represent the opposing flow, while the black dots represent the following flow. The continuous black line shows the parameterization fit of Ruessink et al. (2012).	37
5.21	Ursell number versus the velocity skewness in an opposing (red) and following (black) current. The dots represent the mean per bin, with a bin width of $Ur = 10^{0.05}$ . The vertical lines represent the standard deviation in each bin. The continuous black line shows the parameterization fit of Ruessink et al. (2012).	37
5.22	Deviation from the Ruessink fit for the sea surface elevation skewness. In both opposing and following flow directions with/without depth averaged velocity threshold of $u \ge +/-0.1$	37
5.23	Deviation from the Ruessink fit for the velocity skewness. In both opposing and following flow directions with/without depth averaged velocity threshold of $u >= +/-0.1.$	38
5.24	Correlation of skewness with Ursell number. The significant wave height (blue) and averaged peak period (red) over 6 bursts	40

6.1	Sea surface elevation skewness under a following flow. Results for Ursell number calculated with linear wave theory without currents (black) and Ursell number calculated with linear wave theory with currents (red). The points represent bin means, with a bin width of $10^{0.05}$ , and the lines show the standard deviation. The black lines shows the parameterization fit of Ruessink et al. (2012)	44
6.2	Sea surface elevation skewness under opposing flow. Results for Ursell number calculated with linear wave theory without currents (black) and Ursell number calculated with linear wave theory with currents (red). The points represent bin means, with a bin width of $10^{0.05}$ , and the lines show the standard deviation. The	•
6.3	black lines shows the parameterization fit of Ruessink et al. (2012) Velocity skewness under following flow. Results for Ursell number calculated with linear wave theory without currents (black) and Ursell number calculated with linear wave theory with currents (red). The points represent bin means, bins with a bin width of $10^{0.05}$ , and the lines show the standard deviation. The	44
6.4	black lines shows the parameterization fit of Ruessink et al. (2012) Velocity skewness under opposing flow. Results for Ursell number calculated with linear wave theory without currents (black) and Ursell number calculated with linear wave theory with currents (red). The points represent bin means, with a bin width of $10^{0.05}$ , and the lines show the standard deviation. The black lines shows the parameterization fit of Ruessink et al. (2012)	44
	3-D Conservation Balance	59 61
	Frame 4 instrument codes and heights above seabed	64 64
	Correlation and Signal to Noise ratio of burst 743	67 68
D.2 D.3 D.4 D.5 D.6 D.7 D.8 D.9 D.10 D.11 D.12	The wave spectra of burst 545 with a very high cut-off frequency is used to estimate the surface spectra from linear wave theory	
E.1	The significant wave height versus the velocity skewness. The linear fit is weakly decreasing with significant correlations, thus the skewness is likely to decrease	
E.2	with increasing significant wave height	82
E.3	increasing wave period	82
E.4	Parameterization for pressure sensor 3 and 8. The black line represents the Ruessink (2012) parametrization	83

E.5	Parameterization for pressure sensor 5 and 7. The black line represents the	
	Ruessink (2012) parametrization	83
E.6	The wave asymmetry of the opposing and following flow. The red dots represent	
	the opposing flow, while the black dots represent the following flow	84
E.7	Ursell number versus the wave asymmetry in an opposing (red) and following	
	(black) current	84
E.8	Ursell number versus the velocity asymmetry in an opposing (red) and following	
	(black) current	85
E.9	Ursell number versus the velocity asymmetry in an opposing (red) and following	
	(black) current. The 50 blocks with the mean and standard deviation	85
E.10	OCorrelation of the wave and velocity skewness of frame 4for bursts with a $T_P > 8$ s	86
E.11	Correlation of the wave and velocity skewness of frame 5 for bursts with a $T_P > 0$	
	8s	86
E.12	Wave number under influence of flow (blue) and wave number with no back-	
	ground flow (red).	88
E.13	BUrsell number under influence of flow with changing significant wave height.	
	Constant peak period of 8s and water depth of 5m	88
E.14	Hursell number under influence of flow with changing significant wave height.	
	Constant significant wave height of 8s and water depth of 5m	89
E.15	5The deviation of the measured sea surface elevation skewness for opposing flow.	
	The applied threshold influences the mean limited	90
E.16	6The deviation of the measured velocity skewness for opposing flow. The applied	
	threshold influences the mean limited	91
E.17	7Sea surface elevation skewness for opposing and following flow. Ursell number	
	calculated with linear wave theory (lwt) with and without currents included	91
E.18	BVelocity skewness for opposing and following flow. Ursell number calculated	
	with linear wave theory (lwt) with and without currents included	92

# **List of Tables**

3.1	Instrument setting of ADV, ADCP and pressure sensors of frame 4 and frame 5	15
5.1	Wave parameters for cases 1/2. Averaged over the duration of the case	26
B.2	Frame Location	63 63 65
	The amount of points removed by despiking and SNR/ correlation. The distinction is between the consecutive point or a % of the total amount of points The amount of points removed by despiking and SNR/ correlation. The distinction is between the consecutive point or a % of the total amount of points	69 69
D.2	Overview cases	72 73 78
E.1	Peaks of the plot in Figure 5.4 and 5.5. With the velocity skewness $Sk_u$ , depth-averaged flow $u$ and the tide $\eta_{tide}$	81

# References

- Abreu, T., Silva, P. A., Sancho, F., & Temperville, A. (2010). Analytical approximate wave form for asymmetric waves. *Coastal Engineering*, 57(7), 656–667. Retrieved from http://dx.doi.org/10.1016/j.coastaleng.2010.02.005 doi: 10.1016/j.coastaleng.2010.02.005
- Battjes, J. A. (1982). A case study of wave height variation due to currents in a tidal entrance. *Coastal Engineering*, 6, 47-57. Retrieved from http://ac.els-cdn.com/037838398290014X/1-s2.0-037838398290014X-main.pdf?\_tid=5e962814-9a05-11e7-96a9-00000aab0f01&acdnat=1505473531 453deebd65a7500fa87e0452ab70370d
- Berni, C., Barthélemy, E., & Michallet, H. (2013). Surf zone cross-shore boundary layer velocity asymmetry and skewness: An experimental study on a mobile bed. *Journal of Geophysical Research: Oceans*, 118(4), 2188–2200. doi: 10.1002/jgrc.20125
- Bonneton, P., & Lannes, D. (2017a). Recovering water wave elevation from pressure measurements. *Journal of Fluid Mechanics*, 833, 399–429. Retrieved from https://hal.archives-ouvertes.fr/hal-01588687/document doi: 10.1017/jfm.2017.666
- Bonneton, P., & Lannes, D. (2017b). Recovering water wave elevation from pressure measurements. Journal of Fluid Mechanics, 833, 399-429. Retrieved from https://www.cambridge.org/core/services/aop-cambridge-core/content/view/2D8C0A262A78CF8BB277D3889E87DBC9/S0022112017006668a\_hi.pdf/\_div\_class\_\_title\_\_Recovering\_water\_wave\_elevation\_from\_pressure\_measurements\_\_div\_.pdf doi: 10.1017/jfm.2017.666
- Burrows, R., & Hedges, T. S. (1985). The influence of currents on ocean wave climates. Coastal Engineering, 9(3), 247-260. Retrieved from http://ac.els-cdn.com/0378383985900109/1-s2.0-0378383985900109-main.pdf?\_tid=f7af825e-96e3-11e7-a890-00000aab0f27&acdnat=1505129331 24b585a8824d84e5b7604b60a53758c3 doi: 10.1016/0378-3839(85)90010-9
- Chawla, A., & Kirby, J. (1998). Experimental study of wave breaking and blocking on opposing currents. *Coastal Engineering Proceedings*, 1–14. Retrieved from http://journals.tdl.org/icce/index.php/icce/article/viewArticle/5646
- Chen, B. Q., Member, A., Madsen, P. A., & Basco, D. R. (1999). Current Effects on Non-linear Interactions of Shallow-Water Waves. *J. Waterway, Port, Coastal, Ocean Eng.*, 125(August), 176–186.
- Dodet, G., Bertin, X., Bruneau, N., Fortunato, A. B., Nahon, A., & Roland, A. (2013). Wave-current interactions in a wave-dominated tidal inlet. *Journal of Geophysical Research: Oceans*, 118(3), 1587–1605. doi: 10.1002/jgrc.20146
- Doering, J. C., & Bowen, A. J. (1995). Parametrization of orbital velocity asymmetries of shoaling and breaking waves using bispectral analysis. *Coastal Engineering*, 26(1-2), 15-33. Retrieved from http://ac.els-cdn.com/037838399500007X/1-s2.0-037838399500007X-main.pdf?\_tid=aacc3006-8ee4-11e7-bc7c-00000aab0f27&acdnat=1504250023\_aaeea49f101a1f6bf3bb37aeaa491fbf doi: 10.1016/0378-3839(95)00007-X
- Drake, G. (2001). Discrete particle model for sheet flow sediment transport in the near shore. *JOURNAL OF GEOPHYSICAL RESEARCH*, 106(C9), 19859–19868.
- Eldeberky, Y., & Battjes, J. A. (1996, 1). Spectral modeling of wave breaking: Application to Boussinesq equations. *Journal of Geophysical Research*, 101(C1), 1253. Retrieved from http://doi.wiley.com/10.1029/95JC03219 doi: 10.1029/95JC03219
- Elfrink, B., Hanes, D. M., & Ruessink, B. G. (2006a). Parameterization and simulation of near bed orbital velocities under irregular waves in shallow water. *Coastal Engineering*, 53(11), 915–927. Retrieved from https://ac.els-cdn.com/S0378383906000871/1-s2.0-S0378383906000871-main.pdf? tid=26c25614-b79c-4196-bedf

56 References

-b7652f2ed963&acdnat=1528707927\_49ec48b405b1aa730705149f6ef2f97c doi: 10.1016/j.coastaleng.2006.06.002

- Elfrink, B., Hanes, D. M., & Ruessink, B. G. (2006b). Parameterization and simulation of near bed orbital velocities under irregular waves in shallow water. *Coastal Engineering*, 53(11), 915–927. Retrieved from http://ac.els-cdn.com/S0378383906000871/1-s2.0-S0378383906000871-main.pdf?\_tid=2e91e20e-6c59-11e7-9281-00000aacb360&acdnat=1500451777\_202eeeb0b60e957a9e2cbeb9e6782264 doi: 10.1016/j.coastaleng.2006.06.002
- Elias, E., & van Oeveren-theeuwes, C. (2016). Informatie- en meetbehoefte ten behoeve van Kustgenese-2., 45.
- Grace, R. A. (1978, 1). Surface wave heights from pressure records. *Coastal Engineering*, 2(C), 55-67. Retrieved from http://www.sciencedirect.com/science/article/pii/0378383978900054 doi: 10.1016/0378-3839(78)90005-4
- Grant, W. D., & Madsen, O. S. (1979). Combined wave and current interaction with a rough bottom. *Journal of Geophysical Research*, 84(C4), 1797. doi: 10.1029/JC084iC04p01797
- Grasso, F., Michallet, H., & Barthélemy, E. (2011). Sediment transport associated with morphological beach changes forced by irregular asymmetric, skewed waves. *Journal of Geophysical Research: Oceans*, 116(3), 1–12. doi: 10.1029/2010JC006550
- Henderson, S. M., & Allen, J. S. (2004). Nearshore sandbar migration predicted by an eddy-diffusive boundary layer model. *Journal of Geophysical Research C: Oceans*, 109(6), 1–15. doi: 10.1029/2003JC002137
- Holmedal, L. E., Myrhaug, D., & Rue, H. (2003). The sea bed boundary layer under random waves plus current. *Continental Shelf Research*, 23(7), 717–750. doi: 10.1016/S0278 -4343(03)00020-7
- Holthuijsen, L. H. (2007). Waves in Oceanic and Coastal Waters. New York City: Cambridge University Press. Retrieved from https://books.google.com/books?hl=en&lr=&id=7tFUL2blHdoC&pgis=1 doi: 10.5670/oceanog.2007.42
- Jonsson, I. (1991). Wave-current interaction. The Sea, 9(1), 65–115.
- Kantardgi, I., & Dreyzis, Y. (1993). Wave spectrum filtration by current and wave height calculation. Coastal Engineering, 20(3-4), 203-221. Retrieved from http://ac.els-cdn.com/037838399390002P/1-s2.0-037838399390002P-main.pdf?\_tid=68a78bcc-9e06-11e7-9da0-00000aab0f6c&acdnat=1505913782 c615c6918f2bb042d42eclef344d3a89 doi: 10.1016/0378-3839(93)90002-P
- Kirby, J. T., & Chen, T.-M. (1989). Surface waves on vertically sheared flows: Approximate dispersion relations. Journal of Geophysical Research: Oceans, 94(C1), 1013-1027. Retrieved from http://onlinelibrary.wiley.com/doi/10.1029/JC094iC01p01013/abstract%5Cnhttp://onlinelibrary.wiley.wiley.com/doi/10.1029/JC094iC01p01013/abstract;jsessionid= 06B30F154EC5E69916519CB211B2EA32.f02t03%5Cnhttp://onlinelibrary.wiley.com/store/10.1029/JC094iC01p01013/a doi: 10.1029/JC094iC01p01013
- KNMI. (2014). KNMI Uurgegevens van het weer in Nederland Download. Retrieved from https://projects.knmi.nl/klimatologie/uurgegevens/selectie.cgihttp://www.knmi.nl/klimatologie/uurgegevens/#no
- Lee, D.-Y., & Wang, H. (1984). Measurement of surface waves from subsurface gage. *Coastal Engineering Proceedings*, 271–286. Retrieved from https://icce-ojs-tamu.tdl.org/icce/index.php/icce/article/viewFile/3800/3483
- LEGI UMR 5519 Nonlinearities of waves propagating over a mild-slope beach: laboratory and numerical results. (n.d.). Retrieved from http://www.legi.grenoble-inp.fr/web/spip.php?article885&lang=en
- Longuet-Higgins, M. S., & Stewart, R. W. (1961). The changes in amplitude of short gravity waves on steady non-uniform currents. *Journal of Fluid Mechanics*, 10, 529. doi: 10.1017/S0022112061000342
- Lygre, A., & Krogstad, H. E. (1986). Maximum Entropy Estimation of the Directional Distribution in Ocean Wave Spectra. *Journal of Physical Oceanography*, 16(12), 2052–2060. Retrieved from http://journals.ametsoc.org/doi/abs/10

References 57

.1175/1520-0485%281986%29016%3C2052%3AMEEOTD%3E2.0.C0%3B2 doi: 10.1175/1520-0485(1986)016<2052:MEEOTD>2.0.CO;2

- Michallet, H., Cienfuegos, R., Barthélemy, E., & Grasso, F. (2011). Kinematics of waves propagating and breaking on a barred beach. *European Journal of Mechanics, B/Fluids*, 30(6), 624-634. Retrieved from https://ac.els-cdn.com/S0997754610001305/1-s2.0-S0997754610001305-main.pdf?\_tid=718bd4cc-f0bb-4883-9715-74f2007b2e60&acdnat=1528718550\_0068004a46dfe3a287d0d487f61c608c doi: 10.1016/j.euromechflu.2010.12.004
- Nikora, V. I., & Goring, D. G. (n.d.). ADV MEASUREMENTS OF TURBULENCE: CAN WE IMPROVE THEIR INTERPRETATION? Retrieved from https://ascelibrary.org/doi/pdf/10.1061/%28ASCE%290733-9429%281998%29124%3A6%28630%29
- Nortek. (n.d.). *Velocimeters Nortek USA*. Retrieved from http://www.nortekusa.com/usa/knowledge-center/table-of-contents/velocimeters
- Rocha, M. V., Michallet, H., & Silva, P. A. (2017). Improving the parameterization of wave nonlinearities The importance of wave steepness, spectral bandwidth and beach slope. Coastal Engineering, 121, 77–89. Retrieved from https://ac.els-cdn.com/S0378383916303660/1-s2.0-S0378383916303660 -main.pdf?\_tid=7d0938c0-b26c-11e7-9a77-00000aab0f26&acdnat=1508156648 da66912404dda03c0ef2ab5d36ee00fa doi: 10.1016/j.coastaleng.2016.11.012
- Ruessink, B. G., Ramaekers, G., & Van Rijn, L. C. (2012). On the parameterization of the free-stream non-linear wave orbital motion in nearshore morphodynamic models. *Coastal Engineering*, 65, 56–63. Retrieved from http://dx.doi.org/10.1016/j.coastaleng.2012.03.006 doi: 10.1016/j.coastaleng.2012.03.006
- Ruessink, B. G., Van Den Berg, T. J. J., & Van Rijn, L. C. (2009). Modeling sediment transport beneath skewed asymmetric wavesabove a plane bed. *Journal of Geophysical Research: Oceans*, 114(11), 1–14. doi: 10.1029/2009JC005416
- Terence, B. (1985). Interaction of Random Waves and Currents. *J. Waterway, Port, Coastal, Ocean Eng.*, *I*(2), 275–288.
- Thomson, J., Horner-Devine, A. R., Zippel, S., Rusch, C., & Geyer, W. (2014). Wave breaking turbulence at the offshore front of the Columbia River Plume. *Geophysical Research Letters*, 41(24), 8987–8993. doi: 10.1002/2014GL062274
- Wolf, J. (1999). The estimation of shear stresses from near-bed turbulent velocities for combined wave-current flows. *Coastal Engineering*, 37(3-4), 529–543. Retrieved from www.elsevier.comrlocatercoastaleng doi: 10.1016/S0378-3839(99)00042-3
- Wolf, J., & Prandle, D. (1999). Some observations of wave-current interaction. *Coastal Engineering*, 37(3-4), 471–485. Retrieved from www.elsevier.comrlocatercoastaleng doi: 10.1016/S0378-3839(99)00039-3



### A.1. Linear Wave Theory

When describing waves mathematically with linear wave theory the following assumptions are made. First of all the waves need to be small compared to the water depth. Thereby water has to be assumed as an ideal fluid, so incompressible, no viscosity and a constant density (horizontally).

A balance equations are at the basis of the linear wave theory, the conservation of mass and momentum. These balances are derived from a property  $\mu$  being transported in the x-direction through a volume  $\delta x \delta y \delta z$  in a three dimensional situation, see Figure A.1.

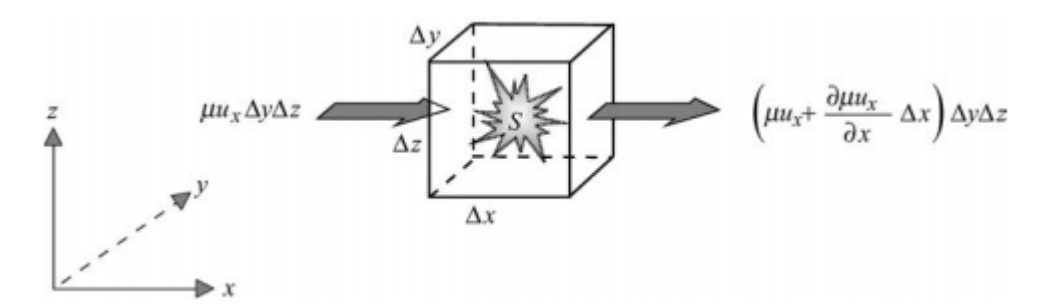


Figure A.1: 3-D Conservation Balance

storage of 
$$\mu$$
 during time interval  $\delta t$   
= net import of  $\mu$  during time interval  $\delta t$  (A.1)  
+ local production of  $\mu$  during time interval $\delta t$ 

$$\frac{\delta\mu}{\delta t} + \frac{\delta\mu u_x}{\delta x} + \frac{\delta\mu u_y}{\delta y} + \frac{\delta\mu u_z}{\delta z} = S \tag{A.2}$$

This equation can be used to derive the mass and momentum balance, since there is assumed that the density is constant and putting in the momentum properties respectively. This result in the following mass and momentum balance, Equation A.3 and Equation A.4.

$$\frac{\delta u_x}{\delta x} + \frac{\delta u_y}{\delta y} + \frac{\delta u_z}{\delta z} = 0 \tag{A.3}$$

$$\frac{\delta \rho u_x}{\delta x} + \frac{\delta \rho u_y}{\delta y} + \frac{\delta \rho u_z}{\delta z} = F_x \tag{A.4}$$

60 A.

If the assumption for constant density is put into the momentum balance the corresponding momentum balance ends up into the linearized momentum balance in x-, y- and z-direction Equation A.5.

$$\begin{split} \frac{\delta u_x}{\delta t} &= -\frac{1}{\rho} \frac{\delta p}{\delta x} \\ \frac{\delta u_y}{\delta t} &= -\frac{1}{\rho} \frac{\delta p}{\delta y} \\ \frac{\delta u_z}{\delta t} &= -\frac{1}{\rho} \frac{\delta p}{\delta z} - g \end{split} \tag{A.5}$$

To find expressions for the propagation speed of wave and wave induced pressure, dynamic and kinematic boundary conditions need to be applied on the continuity and momentum equations. First kinematic boundary condition is that the particles does not leave the surface in other words, so the velocity of the water particles at the surface is equal to the speed of the surface . Second kinematic boundary condition states that the particles can not penetrate through the horizontal fixed bottom. The last boundary condition is dynamic and ensures that the wave is a free wave, only subjected to gravity (Holthuijsen, 2007). The boundary conditions are given in Equation A.6

$$u_z = \frac{\delta \eta}{\delta t}$$
 at  $z = 0$   
 $u_z = 0$  at  $z = -d$   
 $p = 0$  at  $z = 0$  (A.6)

This result in the mathematical solution for the spatial velocity derivative.

$$\phi(x, y, z, t)$$
 defined such that  $u_x = \frac{\delta \phi}{\delta x}$ ,  $u_y = \frac{\delta \phi}{\delta y}$  and  $u_z = \frac{\delta \phi}{\delta z}$  (A.7)

By substituting the velocity potential in the continuity equation, it results in the Laplace equation, Equation A.8. And the linearized Bernoulli equation is derived from the momentum balance, Equation A.9

$$\frac{\delta^3 \phi}{\delta x^2} + \frac{\delta^3 \phi}{\delta v^2} + \frac{\delta^3 \phi}{\delta x^2} = 0 \tag{A.8}$$

$$\frac{\delta\phi}{\delta t} + \frac{p}{\rho} + gz = 0 \tag{A.9}$$

## A.2. Energy balance

The energy density of each wave component  $(f, \theta)$  can be derived by integrating an energy evolution equation propagating with the group velocity on a wave ray.

$$\frac{dE(f,\theta;x,y,t)}{dt} = S(f,\theta;x,y,t)$$
 (A.10)

This left represents the rate of change of the energy density, thereby knowing that  $dx/dt = c_{g,z}$  and  $dy/dt = c_{g,y}$ . The right hand side is the energy dissipation or generation and wave-wave interaction.

To derive the local energy balance, a regular geographic grid, either a Cartesian or a longitude-latitude grid is considered. The energy balance over the cell is taken balancing it over time.

change of energy in cell = net import of energy 
$$+$$
 local generation of energy (A.11)

A.2. Energy balance 61

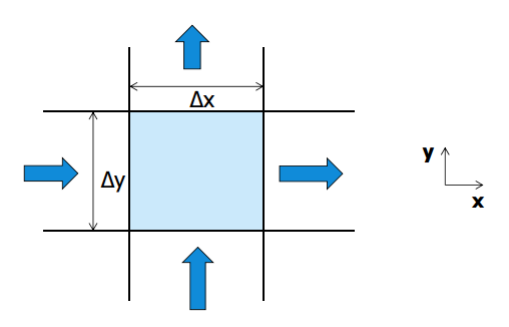


Figure A.2: Energy propagation through one cell

This represent the balance of the incoming energy versus the outgoing energy over the grid cell in interval  $\delta t$ . Finally, when the balance is taken over the cells and divided by  $\delta x \delta y \delta t$ , it will result in Eulerian spectral energy balance for each wave component in deep water, in Equation A.12:

$$\frac{\delta E(\sigma,\theta;x,y,t)}{\delta t} + \frac{\delta c_{gx} E(\sigma,\theta;x,y,t)}{\delta x} + \frac{\delta c_{gy} E(\sigma,\theta;x,y,t)}{\delta y} = S(\sigma,\theta;x,y,t) \tag{A.12}$$



## **B.1. Coordinates frames and pressure sensors**

The position of the five frames are presented in Table B.1:

Table B.1: Frame Location

NAME	Latitude	Longitude
Frame 1	53.5008	5.5705
Frame 2	53.4782	5.5883
Frame 3	53.4436	5.5946
Frame 4	53.4876	5.5351
Frame 5	53.4854	5.5420

The position of the eight pressure sensors are presented in Table B.2:

Table B.2: Pressure sensors Location

NAME	Latitude	Longitude
Buoy E P1	53.4890	5.5305
Buoy G P3	53.4848	5.5326
Buoy F P8	53.4905	5.5360
Buoy H P5	53.4881	5.5443
Buoy J P7	53.4827	5.5400
Buoy I P6	53.4862	5.5395
Buoy K P2	53.4846	5.5445
Buoy L P4	53.4831	5.5491

# **B.2.** Instrument setting frames and pressure sensors

Instruments mounted on the frames 4 and 5 are depicted in Figures ?? and ??. The position of the instrument relative to the bottom is given is Z(m) and it is position relative to the middle of the frame in x, y direction.

#### **B.2.1. Frame 4**

The settings of the instruments on Frame 4 are summarized in Table B.3

64 B.

Sensor	Code	X [m]	Y [m]	Z [m]	Position
ADCP	ADC04	0,017	0,410	2,298	Top center
ADCP	AQD04	-0,752	0,451	0,522	Mid transducer center
ADV	ADV12	-0,134	-0,577	0,926	Mid transducer center
ADV	ADV07	-0,174	-0,925	0,651	Mid transducer center
ADV	ADV08	-0,177	-1,226	0,358	Mid transducer center
3DSRPS	PFS04	-0,152	-0,081	0,977	Head center
OBS	OBS13	0,026	-1,286	0,792	Optical center
OBS	OBS14	-0,198	-1,413	0,504	Optical center
OBS	OBS15	0,000	-1,422	0,302	Optical center
OBS	OBS16	-0,173	-1,483	0,193	Optical center
MPP	MPP04	-0,066	0,244	1,265	Bottom center
LISST	LIS02	0,856	0,502	0,597	Mid transducer center

Figure B.1: Frame 4 instrument codes and heights above seabed

Sensor	Code	X [m]	Y [m]	Z [m]	Position
ADCP	ADC05	-0,501	0,549	2,272	Top center
ADCP	AQD05	-0,864	0,750	0,481	Mid transducer center
ADV	ADV09	-0,157	-0,595	0,981	Mid transducer center
ADV	ADV10	-0,164	-0,893	0,681	Mid transducer center
ADV	ADV11	-0,159	-1,208	0,382	Mid transducer center
3DSRPLS	PFS05	-0,096	-0,055	0,947	Bottom head center
OBS	OBS17	-0,077	-1,335	0,805	Optical center
OBS	OBS18	-0,106	-1,397	0,508	Optical center
OBS	OBS19	-0,177	-1,514	0,203	Optical center
OBS Array	OBS20	-0,085	-1,431	0,231	Optical center
OBS Array	OBS21	-0,088	-1,430	0,200	Optical center
OBS Array	OBS22	-0,090	-1,428	0,169	Optical center
OBS Array	OBS23	-0,093	-1,427	0,137	Optical center
OBS Array	OBS24	-0,095	-1,426	0,105	Optical center
Pressure	PRE01	N/A	N/A	1,910	Pressure opening
MPP	PFS05	-0,141	0,200	1,212	Bottom center
LISST	LIS03	0,905	0,464	0,593	Mid transducer center

Figure B.2: Frame 5 instrument codes and heights above seabed

Table B.3: Instrument settings

Instruments	Frequency	Burstlength	Heigth above seabed
ADV	4011-	00	0.2 m
ADV	16 Hz	29 min 50 sec	0.5 m 0.8 m
ADCP (upward/downward)		continuous	0.0 111
Aquadopp HR	4 Hz	29 min 50 sec	
			0.2 m
OBS	16 Hz	continuous	0.3 m
OBS			0.5 m
			0.8 m
3D Profiling Sonar	842 samples per ping	1 hour	1.5 m
LISST	1 Hz	1 minute	
Pressure Sensor	10 Hz	continuous	



#### C.1. Correlation

Figure C.1 shows a burst with low correlation, but high signal to noise ratio. The point with the low correlation will be removed and interpolated. Since, almost 90% of the points has a low correlation the signal is not relaible in further use.

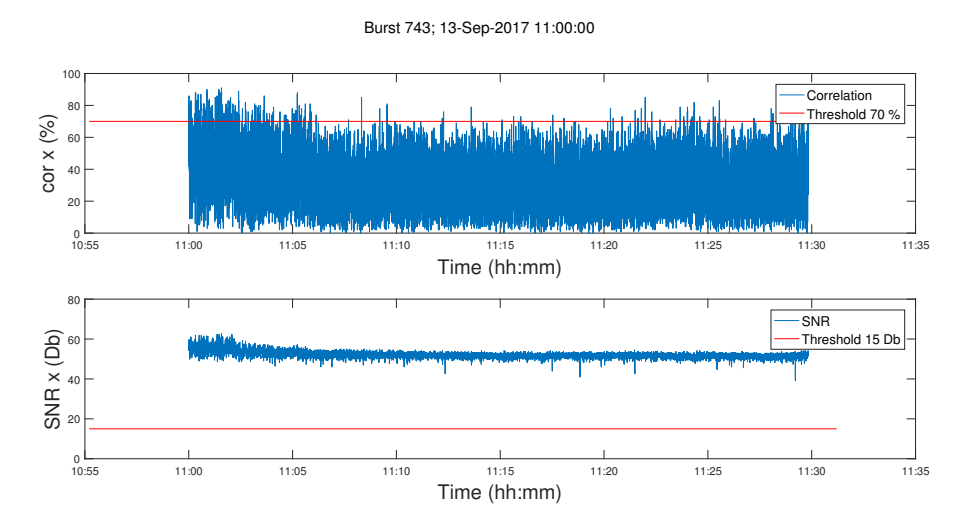


Figure C.1: Correlation and Signal to Noise ratio of burst 743

## C.2. Validity of the bursts after correction

The velocity signal is corrected with the signal to noise ratio, correlation and despiking. However, the interpolation of the removed spikes can also cause errors in the signal. In Table C.1 the amount of bursts removed in the analysis is shown. In this case there are two ways in removing the bursts. The first one is depending on a percentage of the total points in a burst, 28640 points per burst. If the percentage of points removed in the signal is higher than 5% the burst is neglected. However, another method is possible by considering the maximum amount of consecutive point which are removed. This limit is chosen on 16 consecutive points. The 16 point limit chosen because this is exactly 1 HZ, by increasing this limit the waves are not visible in the velocity signal anymore. In Figure C.2 other limits with the corresponding number of burst are shown. In further analysis the criteria of consecutive points is used, since the velocity signal would not represent the wave signal. At shown in Figure C.2 after the correlation check and the despiking the signal still looks good and does not show any unnatural behavior.

68 C.

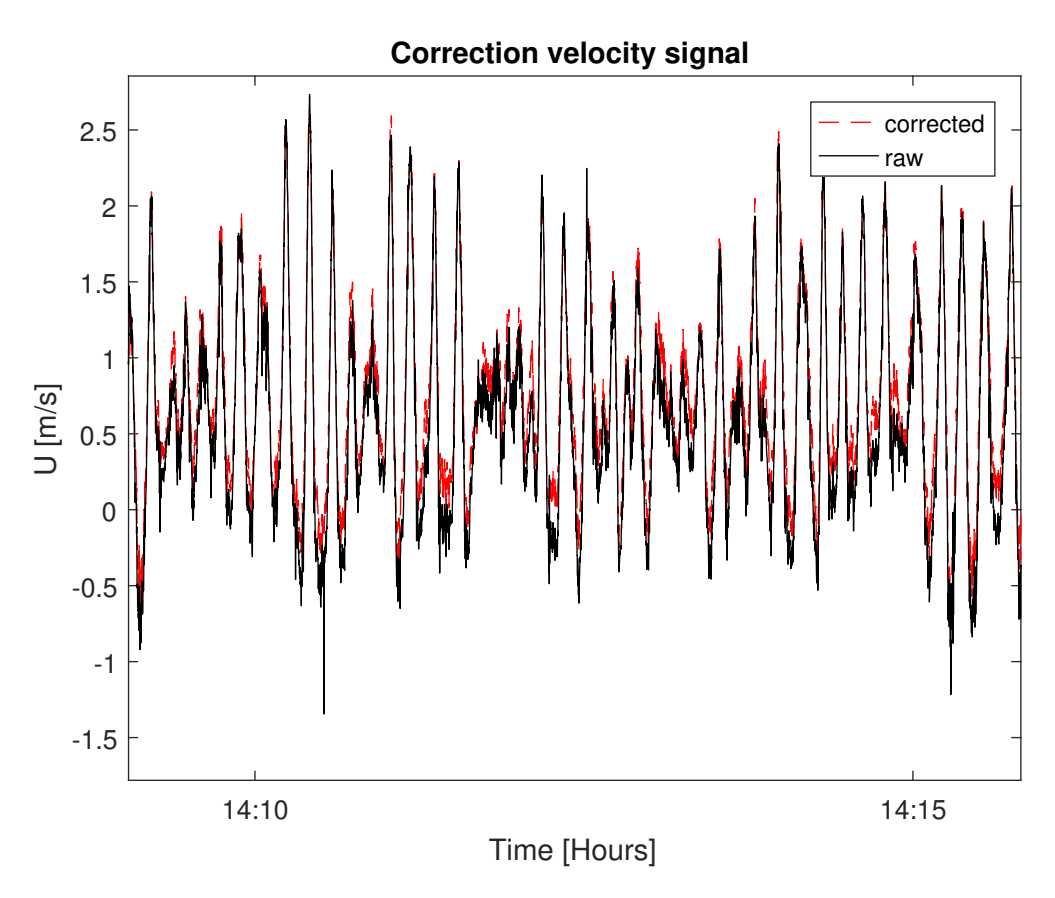


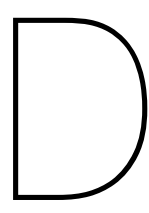
Figure C.2: Raw (black) and corrected (red) velocity signal of burst 749

Table C.1: The amount of points removed by despiking and SNR/ correlation. The distinction is between the consecutive point or a % of the total amount of points.

ADV	total amount of remaining bursts	amount of burst removed by >5 % of the total amount points	amount of burst removed by 15 consecutive point removal
1	1785	505	558
2	2002	193	290
3	1050	597	358

Table C.2: The amount of points removed by despiking and SNR/ correlation. The distinction is between the consecutive point or a % of the total amount of points.

ADV	amount of burst removed by 10 % of the total amount	amount of burst removed by 32 consecutive point removal
1	23	34
2	24	17
3	147	161



In Chapter 4 the pressure signal is obtained with linear wave theory. Linear wave theory assumes that waves are small and constant. However, as waves become more non-linear, steeper and asymmetric linear wave theory is not applicable anymore. In this Chapter the non-linear wave theory developed by Bonneton and Lannes (2017a) is considered. The drawbacks and major influences on the reconstruction of the sea surface elevation are described. First the linear part of the equation is discussed and the wave spectra for the hydrostatic-, the fully dispersive- and the weakly dispersive method are compared. Then after the influence of the cut-off frequency on the wave spectra on the linear and non linear method is elaborated on. In both Sections D.1 and D.2 bursts with without currents. In Section ?? the influence of the currents on the reconstruction is discussed.

## D.1. Linear reconstruction of the surface elevation

In this part the general linear method for reconstruction of the surface elevation is evaluated. This method is distinguished in a fully dispersive approach for intermediate waters and a weakly approach for shallow waters. First the spectra of the approaches will be discussed. Secondly the considerations in using the fully dispersive method are explained.

The weakly dispersive is applicable on shallow waters with  $\mu$  << 1. As explained in Chapter 2, in the weakly dispersive method the linear part depends on the hydrostatic elevation plus a corrected hydrostatic surface elevation for the shallowness parameters. The fully dispersive method shows an other behavior in the wave spectra. In the linear part of this method the hydrostatic surface elevation is corrected with the pressure correction factor K, see Equation 2.13, to take into account the pressure attenuation. The fully dispersive spectra of the linear part shows a gradual increase at higher frequencies, as shown in Figure D.1.

To investigate the limitations in the application of the different methods 6 cases are selected with different peak periods. The duration of the chosen periods are 6 second, 8 seconds and 11 seconds. The peak period of 11 seconds is the largest period present in the measurement, the peak period of 6 seconds is chosen because this period would probably lie close to the cut-off frequency. In Table D.1 the 6 bursts are presented with their corresponding wave parameters and the flow velocity in the direction of the waves. The flow velocity is determined from ADV 1, 0.8m above the seabed.

First, distinction between the method for the selected cases should be made, since the behavior of the two methods is rather different as shown in Figure D.1 In order to do that the shallowness parameter  $\mu=2\pi h^2/L^2$  is used. The shallowness parameter is a measure to determine in which method to apply. If  $\mu$  « 1 the weakly dispersive method is applied, on the contrary if  $\mu$  —1 the fully dispersive method should be applied. In this case the  $\mu$  lies between the 0.36 and 1.4. Therefore, it can be assumed intermediate waters. If the threshold for intermediate waters 1/20 < h/L < 0.5 is applied, the results are shown in Table D.1. Concluding, the fully dispersive method will be used and further explained in this section.

72 D.

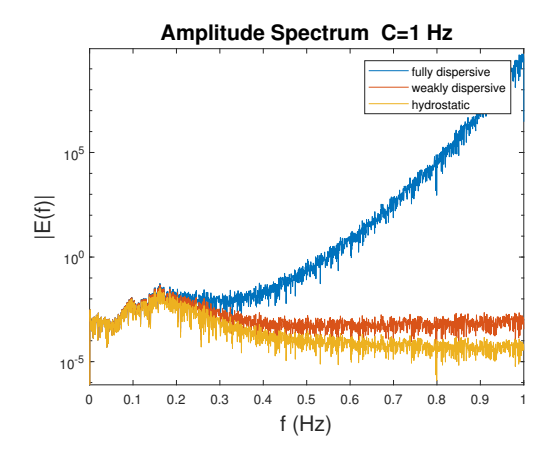


Figure D.1: The wave spectra of burst 545 with a very high cut-off frequency is used to estimate the surface spectra from linear wave theory.

Table D.1: Overview cases

Burst-number	$T_p$ [s]	$H_s$ [m]	$ar{u}_{dir}$ [m/s]		h/L	μ
1757	11	3,19	0,0145	9.0	0.116	0.531
1712	11	3,07	0,0228	10.1	0.096	0.365
910	8	1,22	0,0034	9.1	0.116	0.535
1561	8	0,32	0,0017	9.7	0.152	0.908
545	6	0,75	0.0011	10.0	0.189	1.404
417	6	1,96	0.0025	8.7	0.172	1.169

From Figure D.1 it can be concluded that pressure attenuation correction has a major influence on the shape of the wave spectra. Factor *K* amplifies higher frequencies more strongly in the signal. The signal for high frequency waves is small because the period of the wave is too low for the instrument to measure it. Therefore, *K* is used to amplify those higher frequencies, which adds extra energy to the spectrum.

In practice a cut-off frequency is used to avoid unrealistic amplification of the spectrum in the high frequencies. K is truncated above a certain frequency. Different methods are used to compute K. In Figure D.2 different methods of how to compute K are shown. Method 1 K reaches a certain frequency and from that frequency on the K value is constant. In this method the higher harmonics are equally amplified in the spectra. Method 2, as Bonneton used, computed the K factor as follows: before the cut-off frequency the correction increases with  $cosh(kh)/cosh(z_pk)$  after the frequency the factor returns to 1. This method only amplifies the harmonics until the cut-off frequency. After this threshold, the higher harmonics are not amplified, but are the same as the hydrostatic surface elevation. In method 2 only a small part of the higher frequencies is amplified. Method 3, as shown in Figure D.2, is that if K reaches a certain value K, from that value on K will be constant up to a certain frequency. After that frequency the K value decays to 1. It can be concluded that for all linear surface reconstructions the cut-off frequency is an important factor. If the cut-off frequencies is too high wrong parts of the signal are amplified. If too low, the recovered signal does not represents the real surface elevation.

Concluding from Figure D.2, the cut-off frequency is important in the fully dispersive method. First of all the cut-off frequency can be determined by the ratio h/L. This ratio determines whether the pressure signal reaches the ocean floor. The chosen threshold for this ratio is normally between 0.3 and 0.5. In the following, it is chosen to use the intermediate water condition to be 0.4. The peak frequency of the wave spectra should be below the cut-off frequency. The second criteria is that two times the peak frequency should be below the cut-off frequency, to limit the influence of the cut-off frequency on the first harmonics which play a role in the skewness and asymmetry. Moreover, the number of bursts should remain substantial for further analysis.

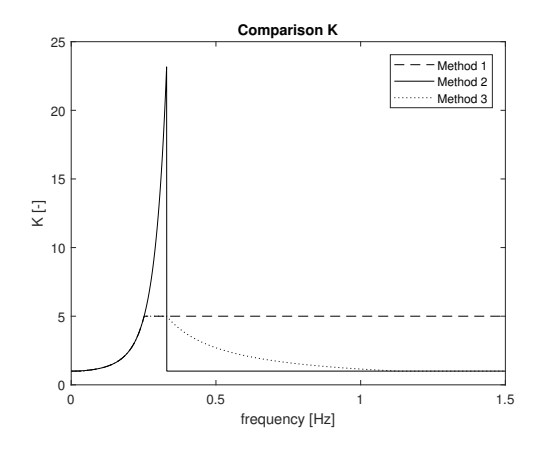


Figure D.2: Attenuation correction factor with h=8.8 m and  $f_c$ =0.33

The cut-off frequency is sometimes determined visually. When the linear part of the spectrum does not follow the hydrostatic spectra anymore. As shown in Figure D.1, the moment when the spectra does not follow the hydrostatic spectra anymore is close to the peak frequency. In the following Figures D.3, D.4 and D.5 the spectra are shown with different cut-off frequencies. The Figures show that it is not a straightforward exercise to chose a cut-off frequency. Especially for spectra with the same period there is not a clear identical spot where the spectra deviates from the hydrostatic spectra.

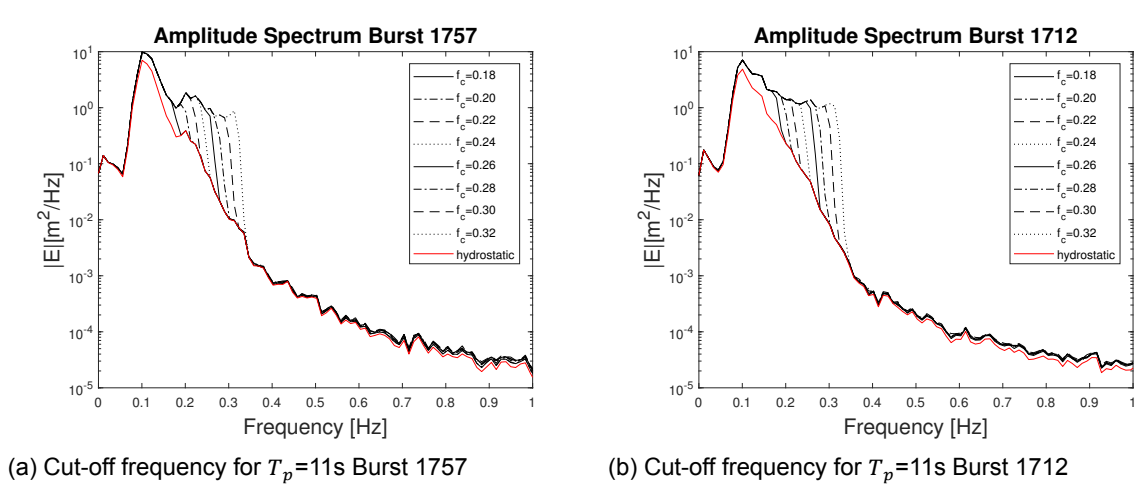


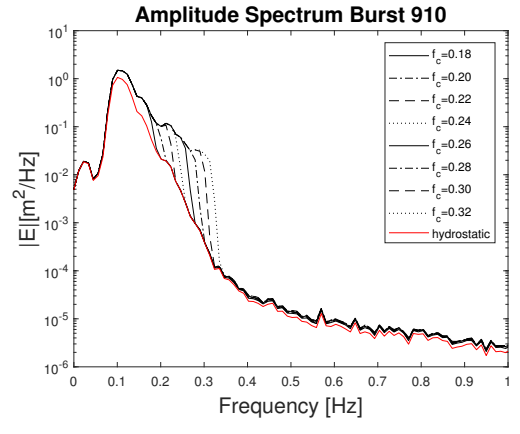
Figure D.3: Cut-off frequency for  $T_p$ =11s

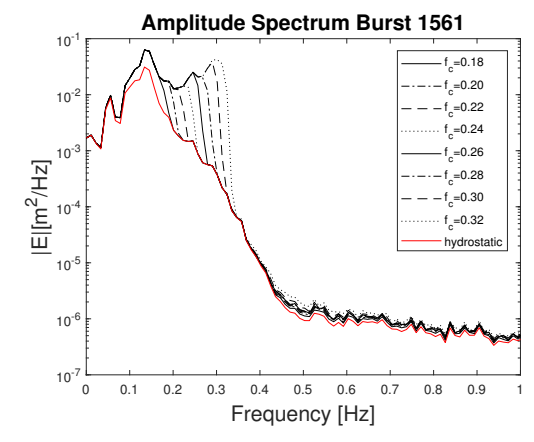
This will result in an upper limit of 0.4 for the criteria h/L for burst with a peak period higher then 8 seconds. From now a cut-off frequency of 0.25 will be used.

Table D.2: Upper limit cut frequencies per burst defined as such h/L<0.4 and  $2f_p < f_c$ 

Burstnumber	$f_c$ [Hz]
1757	0,26
1712	0,25
910	0,26
1561	0,25
545	0,25
417	0,27

74 D.

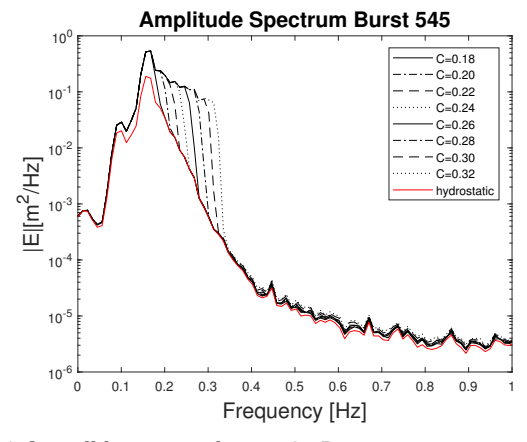


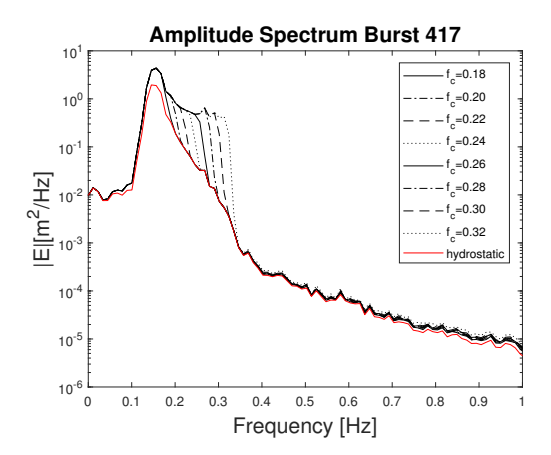


(a) Cut-off frequency for  $T_n$ =8s Burst 910

(b) Cut-off frequency for  $T_n$ =8s Burst 1561

Figure D.4: Cut-off frequency for  $T_p$ =8s





(a) Cut-off frequency for  $T_p$ =6s Burst 545

(b) Cut-off frequency for  $T_p$ =6s Burst 417

Figure D.5: Cut-off frequency for  $T_p$ =6s

### D.2. Non-linear reconstruction of the surface elevation

After introducing the linear part of the fully and weakly dispersive equation of Bonneton, this section will further discuss on the non-linear part. In this section the wave spectra of the fully dispersive method and the influence of the cut-off frequencies on the parameters like skewness and asymmetry will be shown.

#### D.2.1. Influence on the wave spectra

In this part the non-linear part of the calculation is introduced. This non-linear part add a factor that takes into account the wave extrema, by reducing the troughs and amplifying the peak. Moreover it enhances the skewness and asymmetry of the signal.

Bursts 1712, 1757, 1561 and 910 will be discussed here, since it was already noted that the wave spectra with peak period of 6 second were not within the frequency ranges. In the Figure D.11b and Figure D.7 the results of the non linear reconstruction with different cutoff frequencies are shown. After the cut-off frequency there is an additional energy added to the spectra. This complies with the statement from Bonneton and Lannes (2017a). The formula involves the quadratic interaction between the linear part that fills the elevation spectra beyond the cut-off frequency.

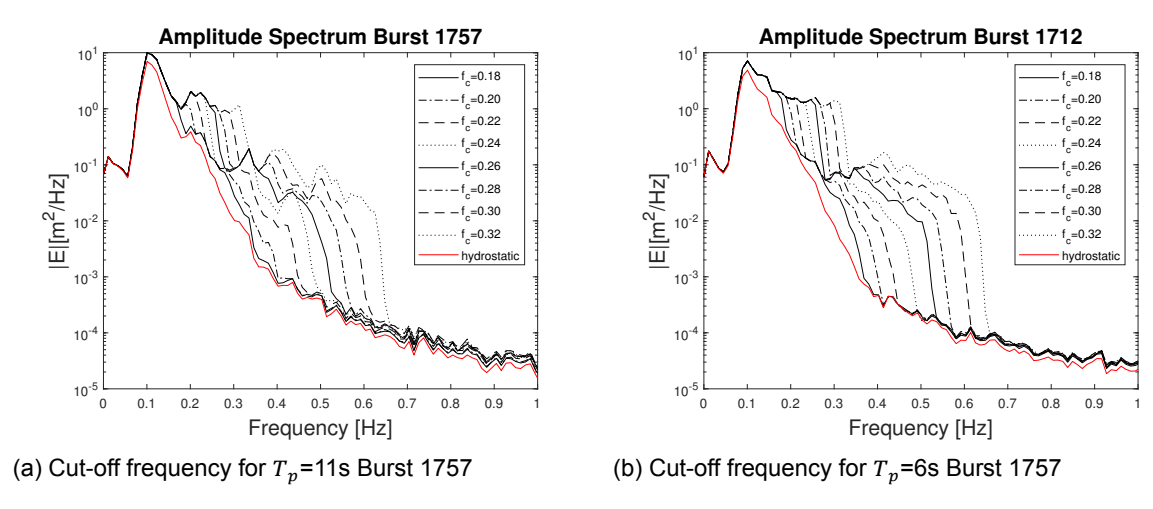


Figure D.6: Results of the non linear reconstruction with different cut-off frequency for  $T_p$ =11s

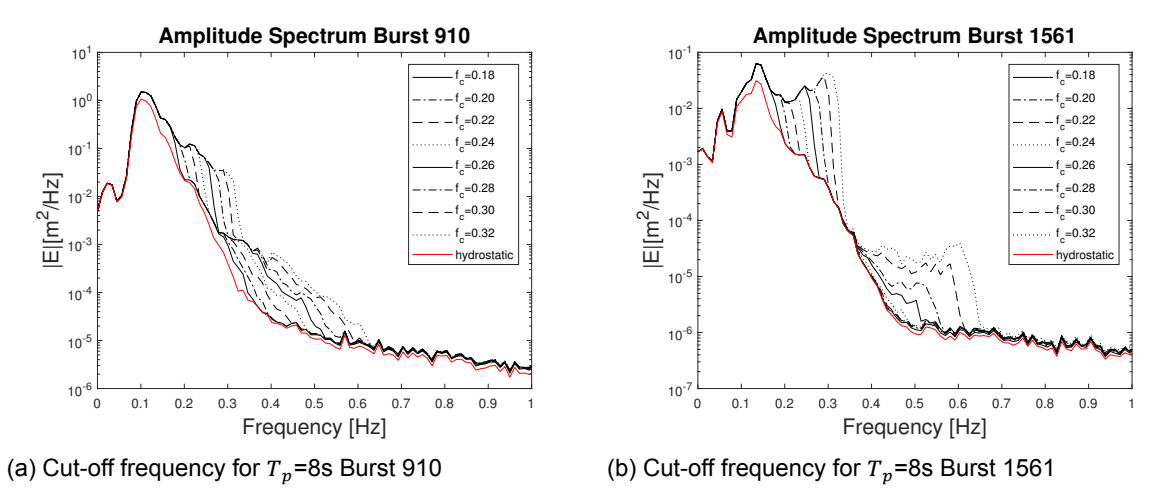


Figure D.7: Results of the non linear reconstruction with different cut-off frequency for  $T_p$ =8s

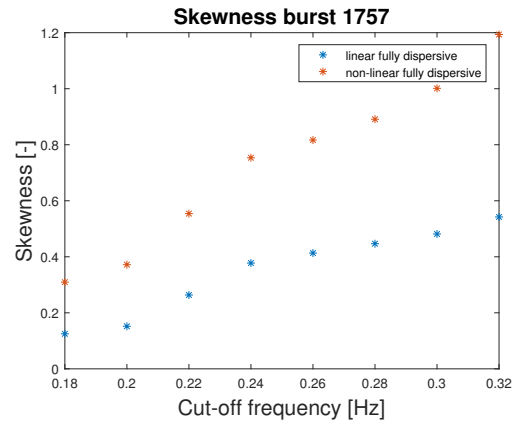
#### D.2.2. Influence on skewness and asymmetry

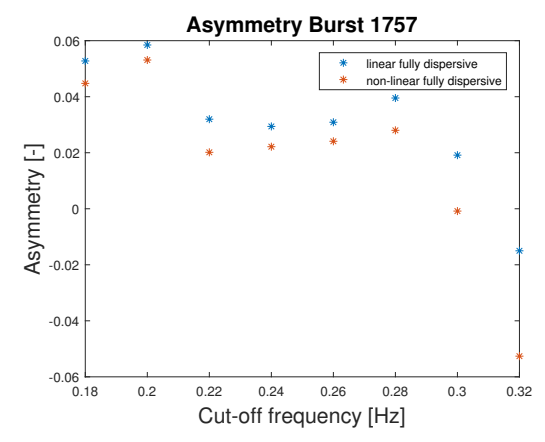
In this section Figures are shown of the cut-off frequency and the corresponding skewness and asymmetry. Earlier, as shown in Table D.2, the ratio d/h < 0.4 is used to determine the cut-off frequency.

In the left panel Figures D.8 to D.11 showing wave skewness, the non-linear part of the fully dispersive method gives a higher skewness than for the linear part. Especially for the higher frequencies the skewness increases faster than skewness for the linear part.

Asymmetry shows a different behavior. Especially for the lower cut-off frequencies the asymmetry for the linear and non-linear part is in the same range. Moreover with increasing cut-off frequencies the asymmetry tends to deviate. Especially case 1561 shows some strange behavior. With increasing frequencies the asymmetry decreases first, but after a cut-off frequency of 0.28 Hz the asymmetry starts to rise again.

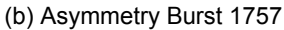
76 D.

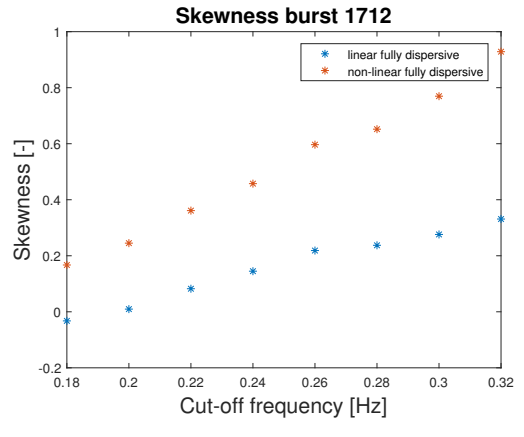


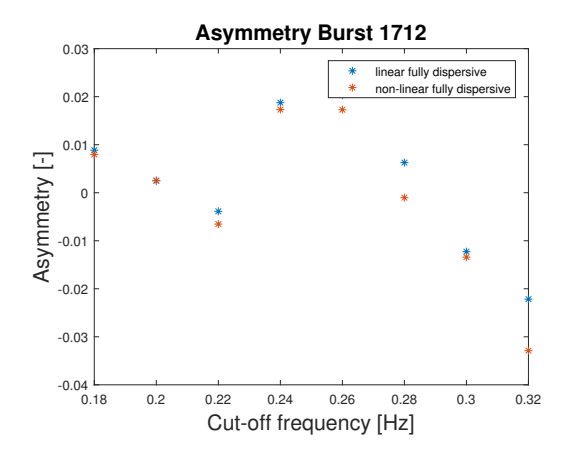


(a) Skewness Burst 1757

Figure D.8: Cut-off frequency for T=11

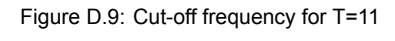


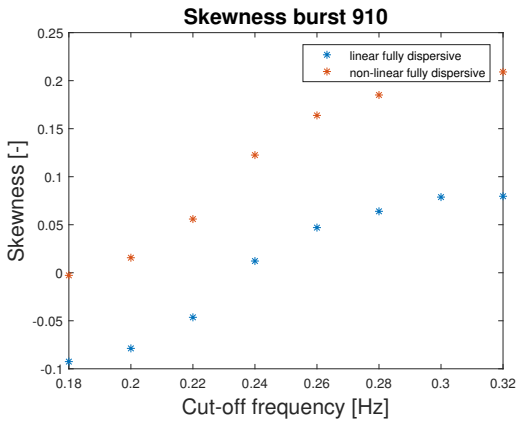


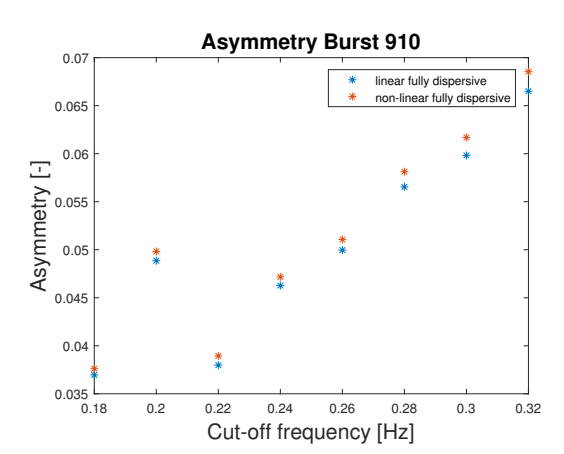


(a) Skewness Burst 1712

(b) Asymmetry Burst 1712







(a) Skewness Burst 910

(b) Asymmetry Burst 910

Figure D.10: Cut-off frequency for T=8

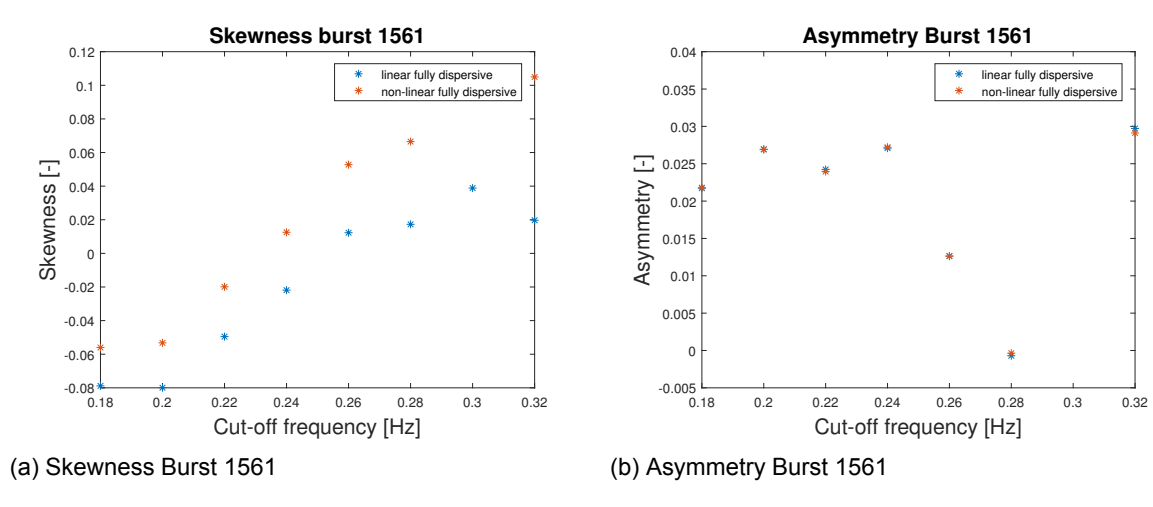


Figure D.11: Cut-off frequency for T=8

## D.3. Influence of current on wave spectra

In the above section the theory is applied in cases with negligible currents. However, the current has a major influence on the wave number. In Chapter 2 the influence of a current on the absolute and intrinsic frequency is explained. Not only has the wave number influence on the wave, also on the orbital velocity profile. The wave height is underestimated when linear wave theory is applied without current, for an opposing flow and overestimated for a following flow.

As discussed earlier, the focus is on cases with a peak period higher than 8 second and to not interfere with the cut-off frequency which is 0.25 Hz. The velocity profile is considered uniform over the depth. The flow velocity is determined by averaging the ADCP bins over the depth. The dispersion relation with currents is used, Equation 2.4. By iteration the corresponding wave number is calculated, thereafter the wave spectra are computed.

5 Bursts are considered under influence of a currents. Two burst have a following flow, while 3 bursts have an opposing flow. In table D.3 the results clearly shows that the wave height strongly increases if the magnitude of the current rises. In contrary, opposing currents tend to decrease the significant wave height. With very high opposing flows the spectra tend to shift to higher frequencies. But, in case of a flow in the wave propagation direction the spectra loses energy and the peak shifts to the lower frequencies. Burst 1725 and burst 749 illustrate this effect in Figure D.12. As observed, the spectra has the tendency to shift from the higher to lower frequencies.

In Table D.3 wave parameters calculated with linear wave theory are shown. U is the depth averaged velocity of the ADCP. The parameters with lower-bar c indicate the current is taken into account in linear wave theory. The minus sign in flow velocity stands for an opposing flow, while the plus is for a flow in the direction of the waves. Table D.3 shows that the significant wave height under influence of a current has a big variability, while the dimensionless wave parameters has limited variability. Under influence of a high current, for example burst number 755, the significant wave height increases up to 90%, albeit the increase of significant wave height with low flow, burst number 1725, only decreases with 3%.

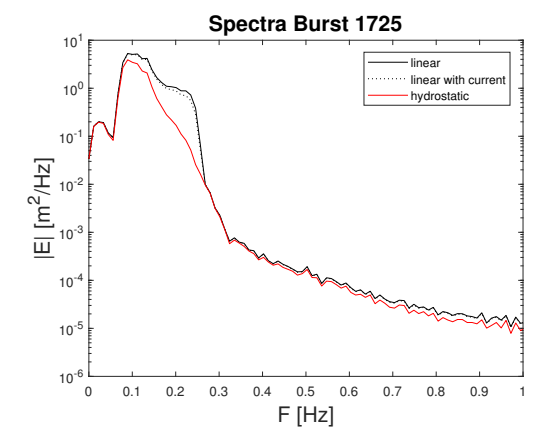
The variability of those wave parameters can be explained by the pressure attenuation factor K again, since the pressure attenuation factor K is related to the wave number. The change in wave number can be significant especially for flows against the direction of the waves for which k decreases, leading to a stronger increase in K. In Section D.1 it was shown that the shape of the linear part of the wave spectra is mostly determined by K in the higher frequencies. This explains why at the high frequencies at Burst 749 an increase in energy emerges. In the case of burst 755, as shown in Figure D.14, most of the energy is centered at the high frequency part below the cutoff frequency. Since there is a major change in the wave number induced by the flow of -1.32m/s, the pressure attenuation factor amplifies the

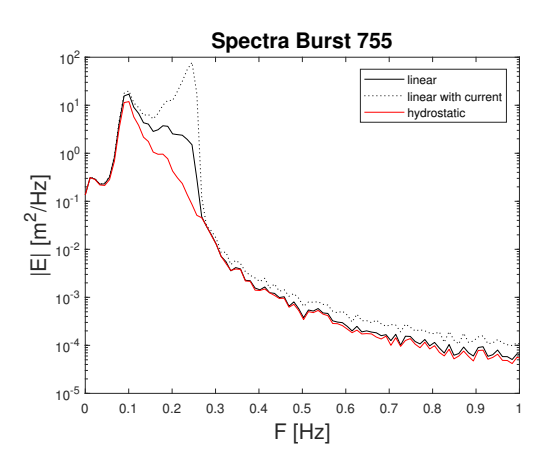
78 D.

spectra even more at high frequencies.

Table D.3: Results on the wave parameters using linear wave theory reconstruction with and without current. -c denotes the cases with current, U is the depth averaged velocity of the ADVP in the direction of the waves.

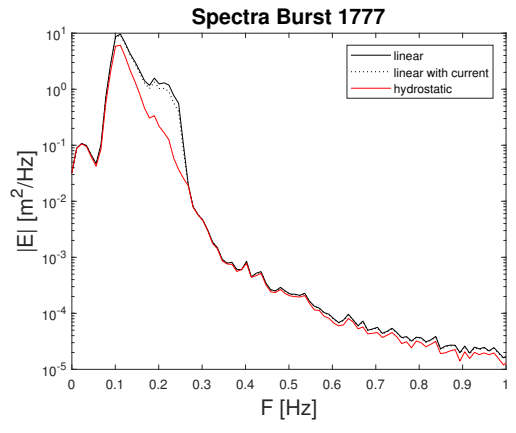
Burstnumber	1725	1777	1675	749	755
U [m/s]	0,28	0,34	-0,57	-0,91	-1,32
Sk [-]	0,19	0,30	0,04	0,59	0,34
$Sk_c$ [-]	0,16	0,27	0,09	0,50	0,19
As [-]	-0,10	0,07	0,01	-0,11	-0,07
$As_c$ [-]	-0,09	0,07	0,01	-0,09	-0,02
<i>Hs</i> [m]	2,70	2,96	2,67	4,59	3,97
$Hs_c$ [m]	2,63	2,85	2,98	6,08	7,58

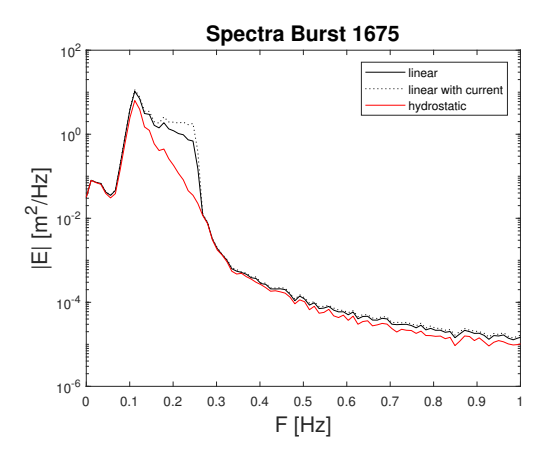




- (a) Spectra for 1725 with a following flow of 0.3m/s
- (b) Spectra for 1725 with an opposing flow of 1.332m/s

Figure D.12: The change in spectra for opposing and following flow





- (a) Spectra for 1777 with a following flow of 0.34m/s
- (b) Spectra for 1675 with an opposing flow of 0.57m/s

Figure D.13: The change in spectra for opposing and following flow

D.4. Conclusion 79

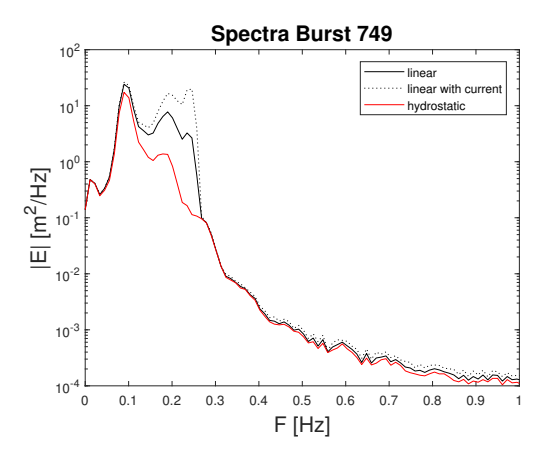


Figure D.14: Spectra for burst 749 with an opposing current of 0.91 m/s

#### D.4. Conclusion

The conclusion consists of three parts. The first parts discusses the results of the linear reconstruction of the surface elevation. The second part concludes on the non-linear reconstruction, while the third part presents the finding on including the currents on the linear surface reconstruction.

Linear reconstruction shows that the pressure attenuation correction K has a major influence on the wave spectra. The shape and the cut-off frequency determine how the hydrostatic spectra is amplified in the higher frequencies. The selection criteria for the cut-off frequencies are 1) the case should be in intermediate water h/L<0.5 and 2) two times the peak frequency should be lower than the cut-off frequencies. This results in a cut-off frequency of 0.25Hz.

The non linear reconstruction shows an increase in energy beyond the cut-off frequency. This is caused by the quadratic interaction between the linear part of the spectra. As a result of this increase in energy in the higher parts of the spectra, this leads to an major increase in skewness. By varying the cut-off frequency it is shown that the skewness is very depended on the choice of the cut-off frequency. However, if the asymmetry is compared for the linear and non linear reconstruction shows a small asymmetry and little variability. Also the increase in asymmetry is limited with an increasing frequency. Concluding from above results outcome of the non linear reconstruction the dependence on a chosen cut-off frequency is too high. This could lead to over or underestimation of the actual wave parameters. Since there is not real representation of the surface elevation, this can not be verified.

If currents are involved in linear wave theory the spectra show a shift toward higher or lower frequencies depending on the flow direction. This shift is caused by the change in wavenumber due to the flow. Stronger flow in the direction of the waves cause a lower wave number. This has influence on the pressure attenuation correction, as discussed earlier in Section D.1. In the results is shown that with very high flow velocities the peak tends to shift towards the cut-off frequency. Concluding from these results by applying a flow in the linear wave theory leads to an overestimation of the wave height for high flow velocities, while it does not have major effect on the wave skewness and asymmetry. So this method will not be used in further analysis.



### E.1. Overall results

This section discusses the variation of the tide and the correlation between the asymmetry, and wave height and period.

The skewness varies with the tide, as shown in Table E.1. It presents the peak of the velocity skewness, tidal velocity and the tidal elevation of frame 4. It it shown, case 1 the peak of the skewness is just after the peak of the tidal velocity and just before the tidal elevation. Case 2 shows that the peak of the skewness is 1.5 hours before the peak of the tidal velocity and around low water.

Asymmetry values are negatively correlated to the significant wave height and the peak period. The correlation for the significant wave height  $R^2 = 0.03$  and peak period  $R^2 = 0.032$  is weak but significant. This negative correlation means that the asymmetry increases, waves have steeper fronts and longer tails.

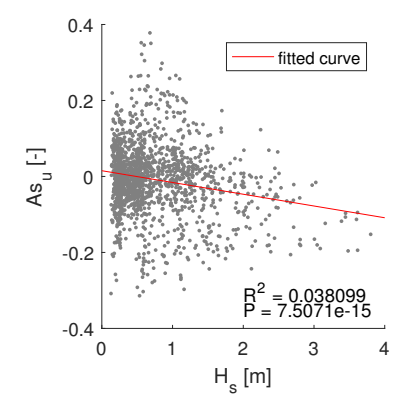
Table E.1: Peaks of the plot in Figure 5.4 and 5.5. With the velocity skewness  $Sk_u$ , depth-averaged flow u and the tide  $\eta_{tide}$ .

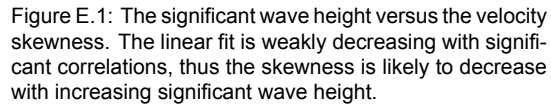
#### Peak of the parameters case1

$Sk_u$	u	$\eta_{tide}$
02-Sep-2017 05:00	-	02-Sep-2017 05:00
02-Sep-2017 16:30	02-Sep-2017 15:00	02-Sep-2017 18:30
03-Sep-2017 05:30	03-Sep-2017 03:30	03-Sep-2017 07:00
03-Sep-2017 18:30	03-Sep-2017 16:00	03-Sep-2017 19:30
04-Sep-2017 07:00	04-Sep-2017 06:00	04-Sep-2017 08:00

#### Peak of the parameter case 2

$Sk_u$	u	$\eta_{tide}$
16-Sep-2017 00:00	16-Sep-2017 01:30	16-Sep-2017 05:00
16-Sep-2017 12:30	16-Sep-2017 15:00	16-Sep-2017 18:00
17-Sep-2017 01:00	16-Sep-2017 21:30	17-Sep-2017 06:30
17-Sep-2017 14:00	17-Sep-2017 15:30	17-Sep-2017 19:00
18-Sep-2017 02:00	18-Sep-2017 04:30	18-Sep-2017 07:30





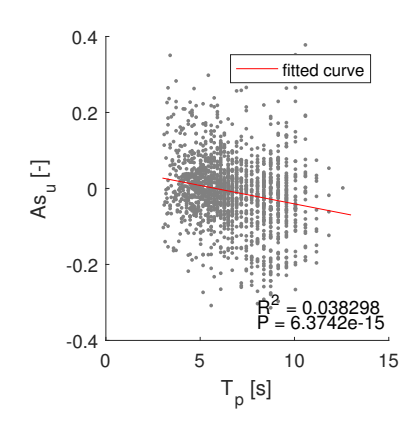


Figure E.2: The peak period versus the velocity skewness. The linear fit is weakly decreasing with significant correlations, thus the skewness is likely to decrease with increasing wave period.

## E.2. Parameterization of the pressure sensors

In this section the asymmetry for the pressure sensors are shown. The parameterization of Ruessink et al. (2012) is

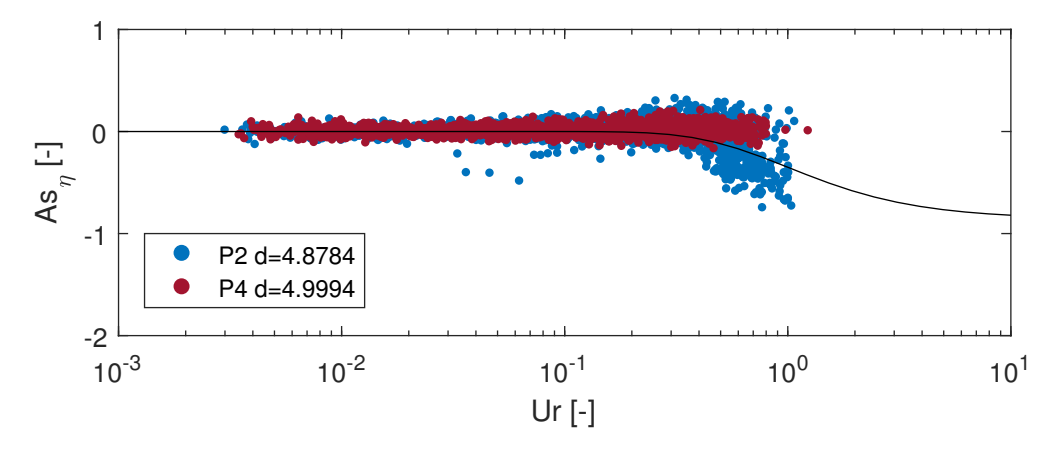


Figure E.3: Parameterization for pressure sensor 2 and 4. The black line represents the Ruessink (2012) parametrization.

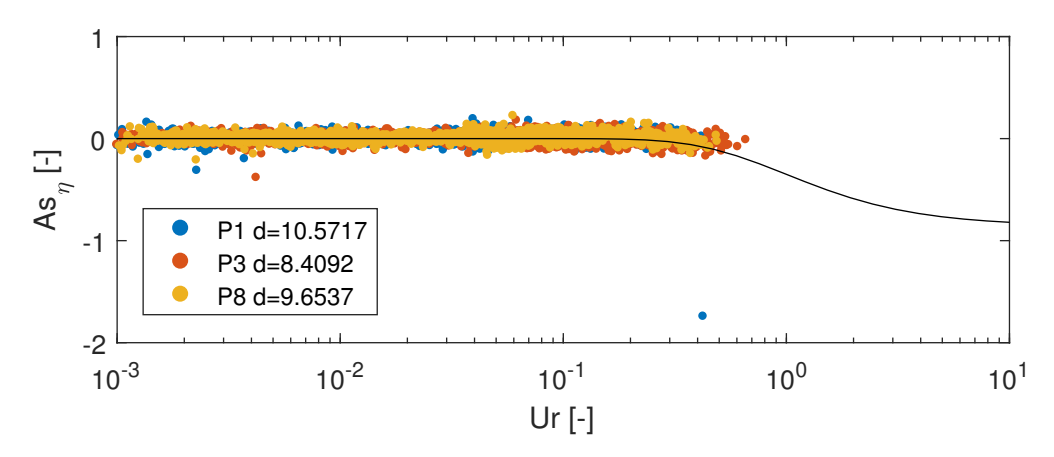


Figure E.4: Parameterization for pressure sensor 3 and 8. The black line represents the Ruessink (2012) parametrization.

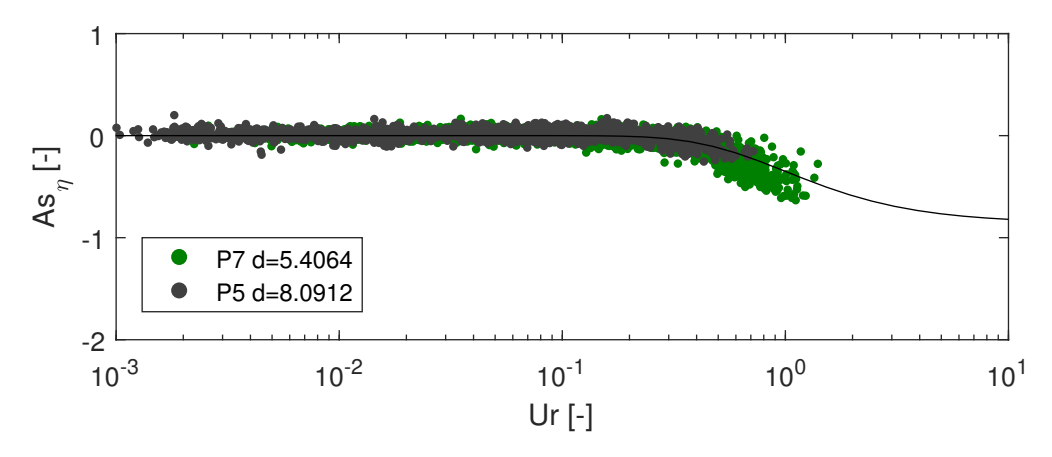


Figure E.5: Parameterization for pressure sensor 5 and 7. The black line represents the Ruessink (2012) parametrization.

# E.3. Sea surface asymmetry under influence of flow

Figures 5.19 and E.7 show the mean and standard deviation per block. The Usrell number is divided in 50 blocks, the mean and standard deviation is calculated for the points within the block. The flow direction is determined with the flow velocities of ADV 9 on frame 5. If the flow velocity over the burst was positive a following flow is assumed over all the pressure sensors. A negative flow would relate to an opposing flow.

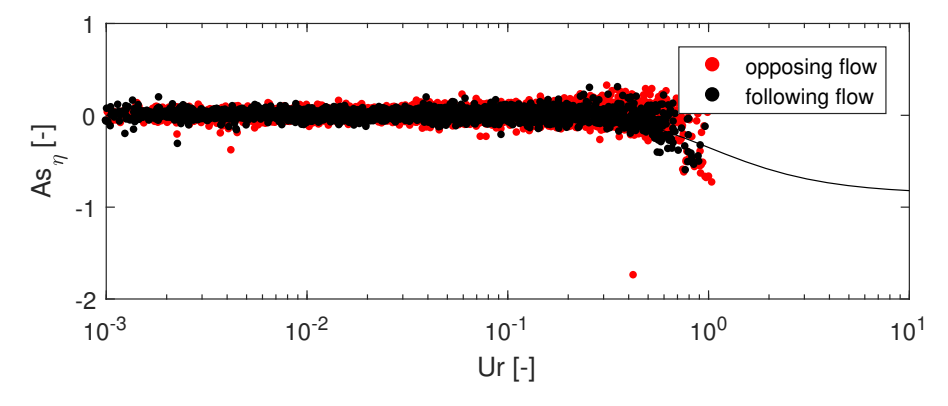


Figure E.6: The wave asymmetry of the opposing and following flow. The red dots represent the opposing flow, while the black dots represent the following flow.

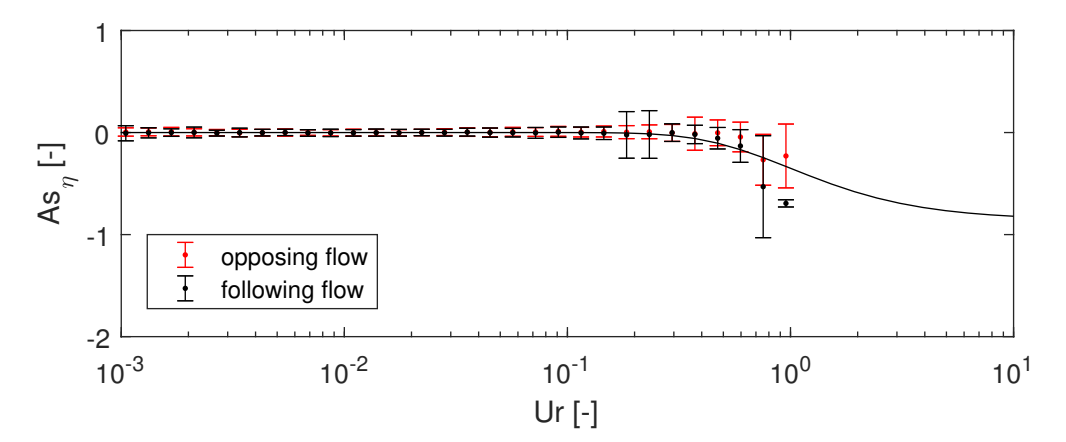


Figure E.7: Ursell number versus the wave asymmetry in an opposing (red) and following (black) current

## E.4. Velocity asymmetry under influence of flow

Figures E.8 shows the mean and standard deviation per block. The Usrell number is divided in 50 blocks, the mean and standard deviation is calculated for the points within the block.

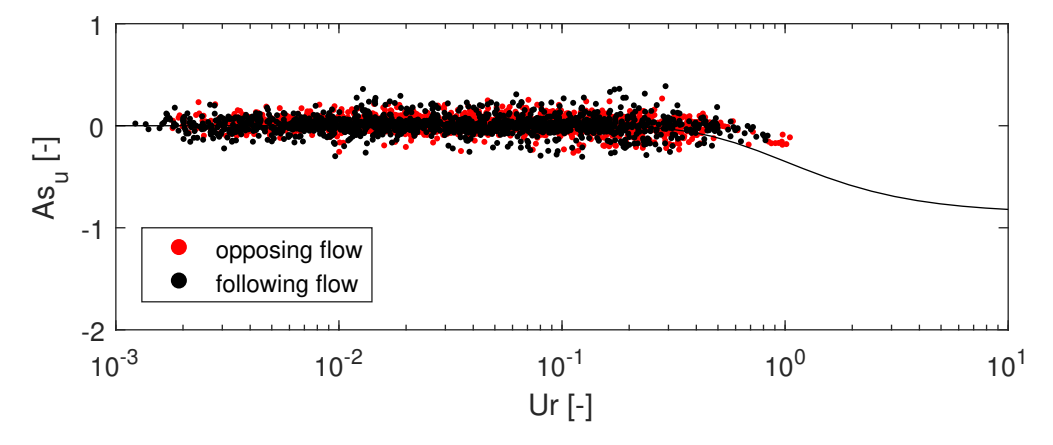


Figure E.8: Ursell number versus the velocity asymmetry in an opposing (red) and following (black) current

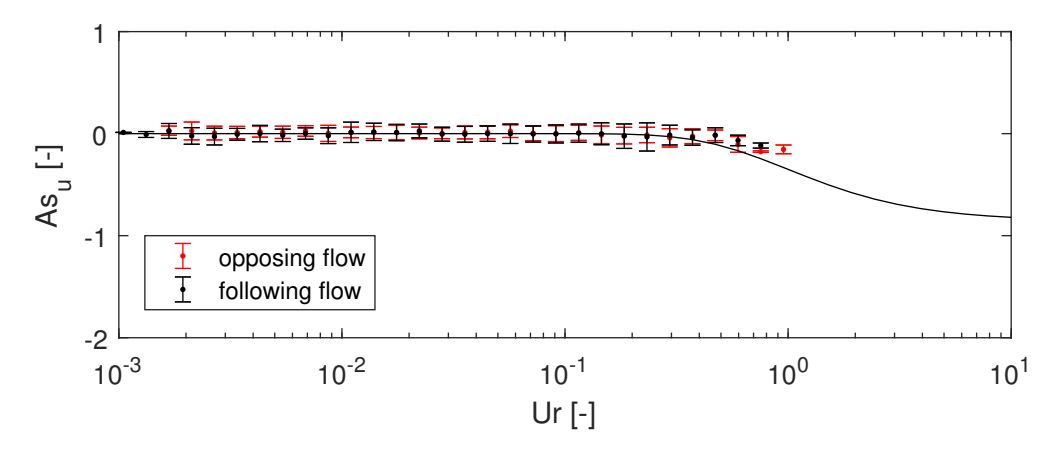


Figure E.9: Ursell number versus the velocity asymmetry in an opposing (red) and following (black) current. The 50 blocks with the mean and standard deviation.

## E.5. Correlation sea surface elevation- and velocity skewness

This section shows the correlation for the sea surface elevation skewness and velocity skewness, with a filter. The filter only includes bursts with periods higher than 8 seconds. As discussed earlier, Chapter 5, the correlation increases with respect to the case without this filter. The correlation for the sea surface elevation skewness and velocity skewness is  $R^2 = 0.69$  and  $R^2 = 0.62$ , respectively.

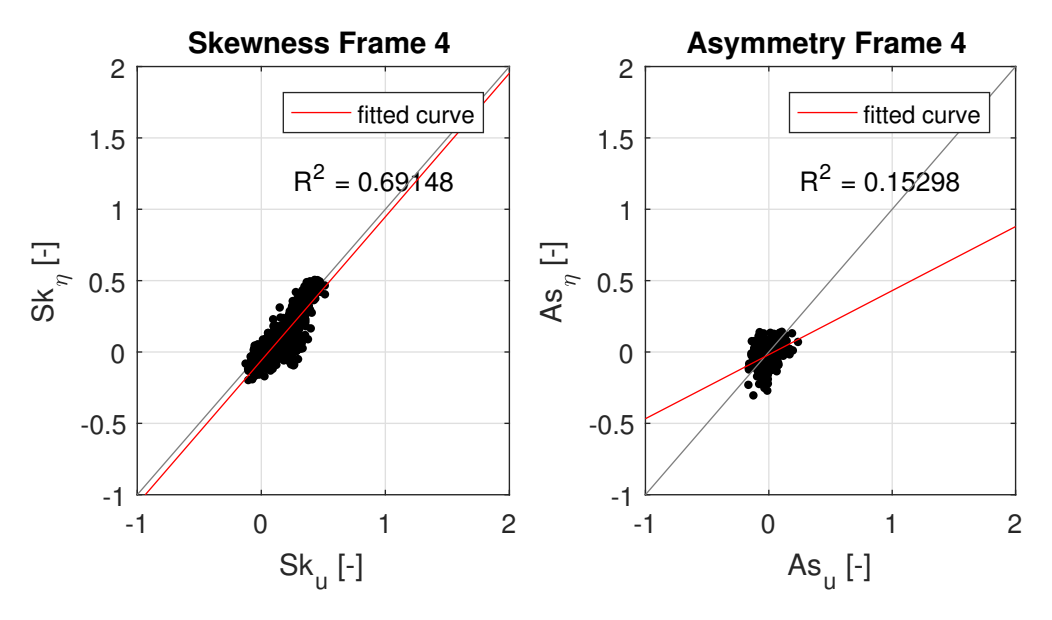


Figure E.10: Correlation of the wave and velocity skewness of frame 4for bursts with a  $T_P > 8s$ 

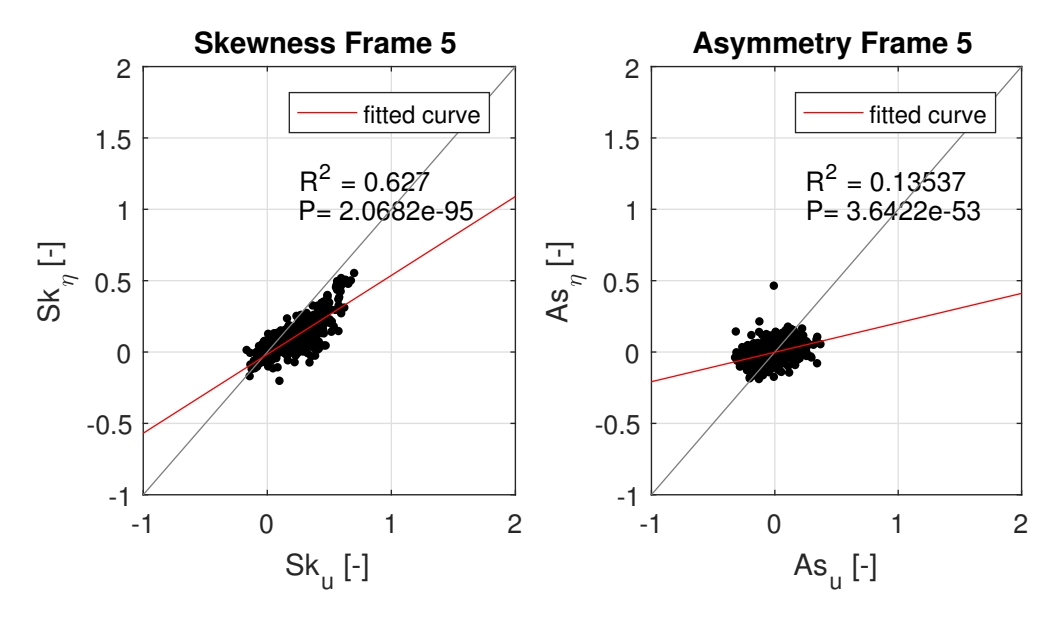


Figure E.11: Correlation of the wave and velocity skewness of frame 5 for bursts with a  $T_P > 8$ s

### E.6. Ursell number versus current

In this section the influence of wave height and period on the Ursell number is investigated. The Ursell number is depended on the local wave height, depth, peak period and therefore also on the wave number. Since a current modulates the absolute frequency and thereby the wave number, it affects the Ursell number. In Appendix D the influence of the current on wave height is discussed. It concluded that under influence of relatively high currents the significant wave heights shows unrealistically high values and therefor not further used. Only to capture the current in the Ursell number the intrinsic period has been changed. First of all the wave number under influence of a current is discussed. Afterward, the response of the wave height and peak period is investigated.

To investigate the influence of the flow on wave number a case is picked with peak period of T = 8s and water depth h = 5m. The flow is ranged from -1 m/s and 1 m/s. An opposing flow -1 m/s and the following flow is 1 m/s. It can be concluded that the wave number increases with an opposing flow, while decreases in following flow, as shown in Figure E.12.

In the same way the influence of changing wave height and period is investigated. The flow is ranged between -2 m/s and 2 m/s. Thereby the wave height is ranged from 0.5m up to 5m with a peak period of 8s and water depth of 5m. The absolute period is changed from 6 s up to 12 s with a significant wave height of 1m and water depth of 5m. The result show that Ursell number for opposing flows is smaller than Ursell number under following flow. Thereby with an increasing wave height the Ursell number also rises, as shown in Figure E.13. The peak period influences the Ursell number in the same way. An opposing flow causes lower Ursell numbers than following flow and with increasing period the Ursell number increases as well, as shown in Figure E.14.

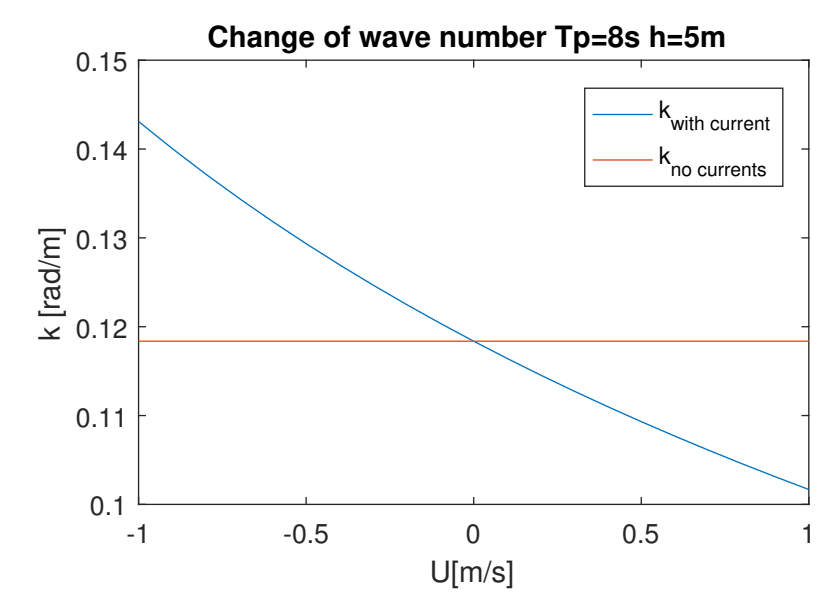


Figure E.12: Wave number under influence of flow (blue) and wave number with no background flow (red).

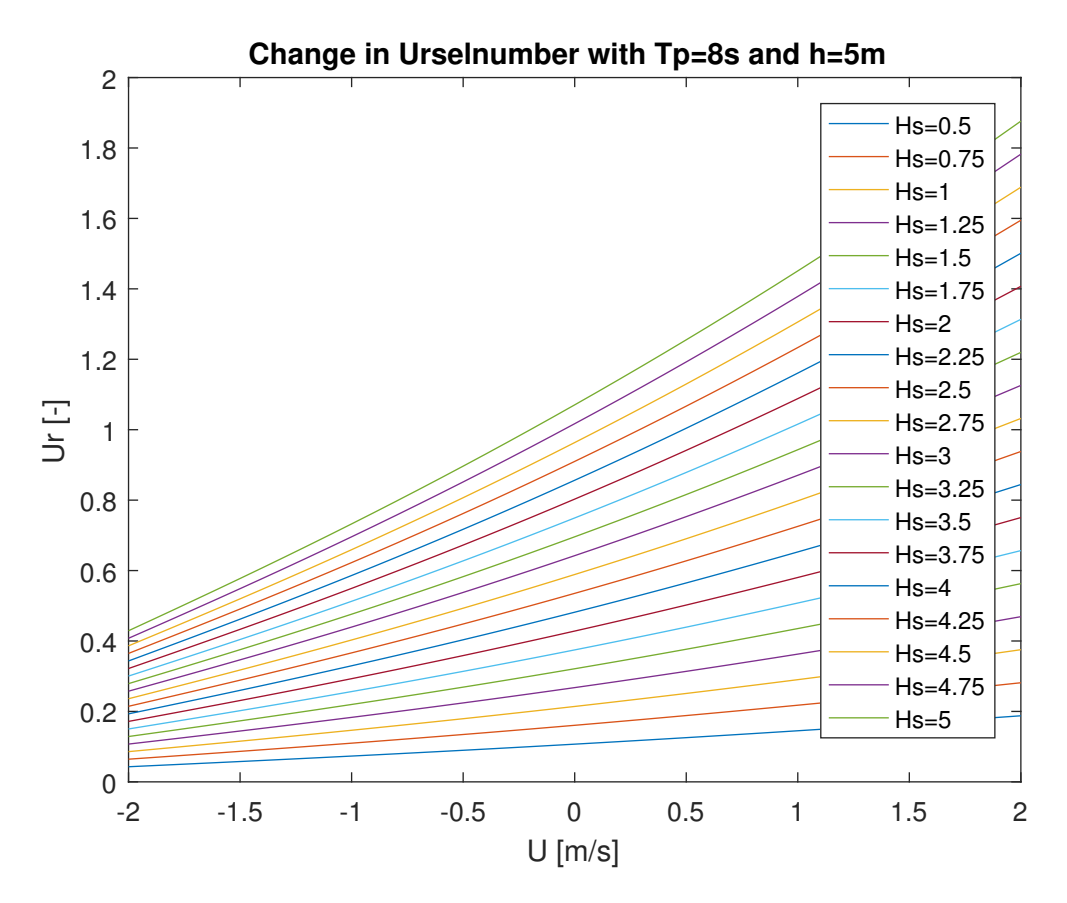


Figure E.13: Ursell number under influence of flow with changing significant wave height. Constant peak period of 8s and water depth of 5m.

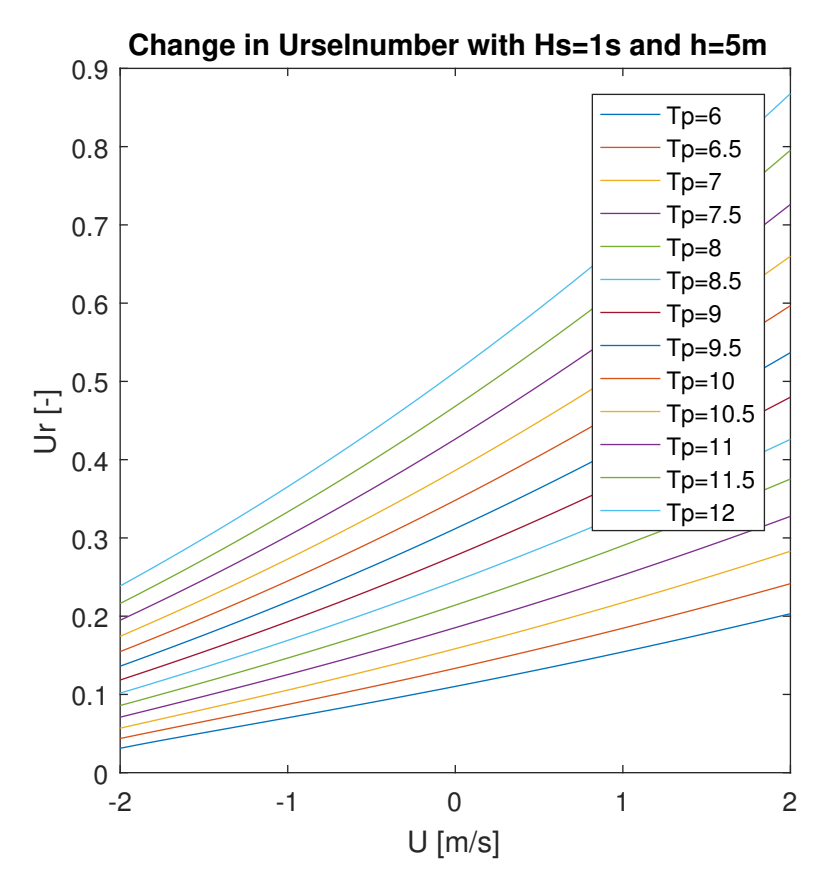


Figure E.14: Ursell number under influence of flow with changing significant wave height. Constant significant wave height of 8s and water depth of 5m.

### E.7. Deviation of the fit

This section shows the deviation of the asymmetry for the Ruessink (2012) parameterization. A threshold is applied for the depth-averaged flow of |u| > 0.1. As shown shown in Figures E.15 and E.16, the threshold has little influence.

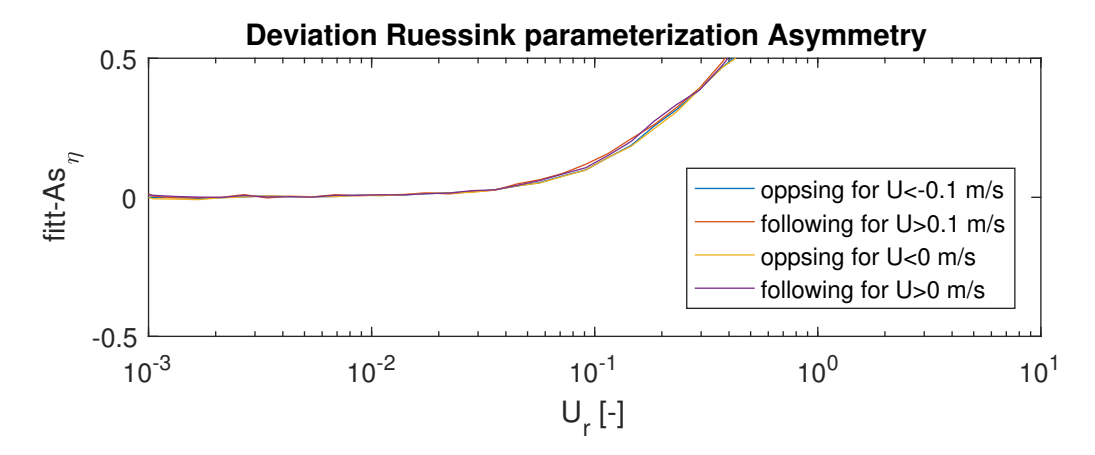


Figure E.15: The deviation of the measured sea surface elevation skewness for opposing flow. The applied threshold influences the mean limited.

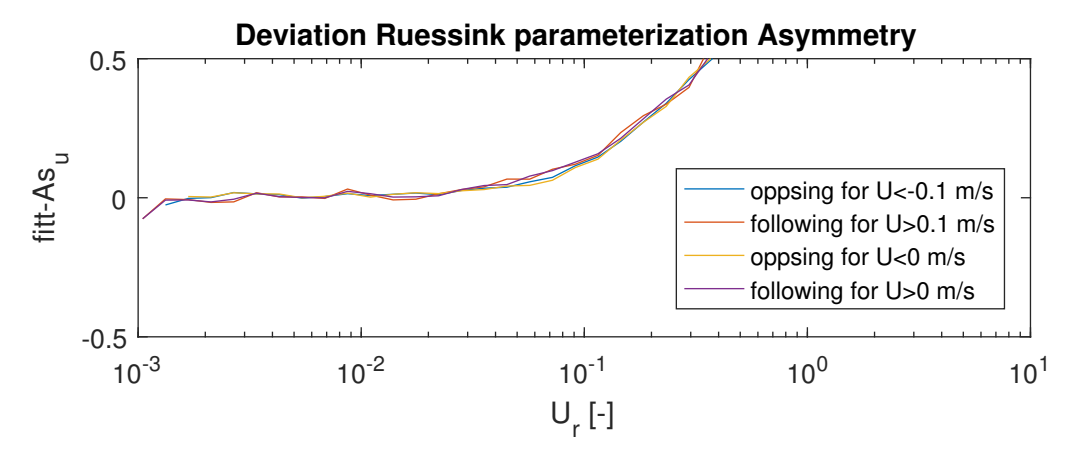


Figure E.16: The deviation of the measured velocity skewness for opposing flow. The applied threshold influences the mean limited.

# E.8. Adapting Ursell number

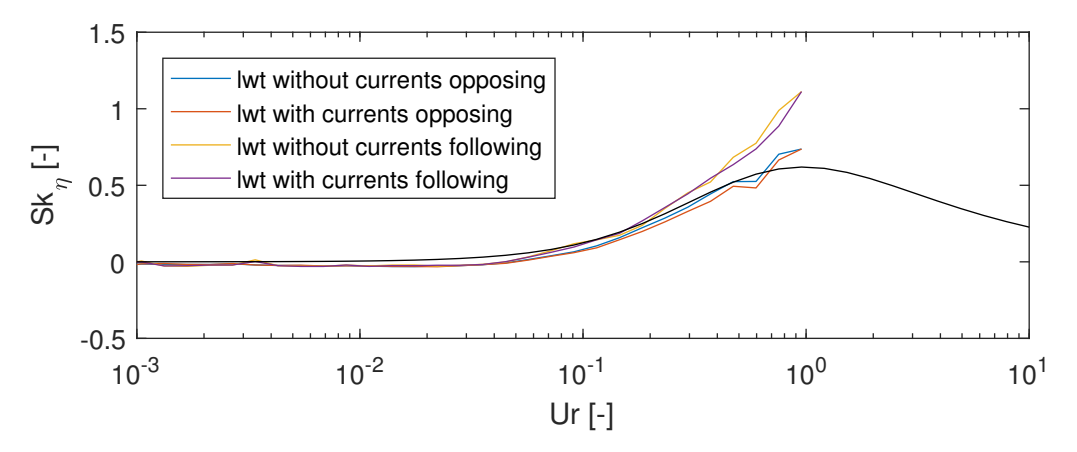


Figure E.17: Sea surface elevation skewness for opposing and following flow. Ursell number calculated with linear wave theory (lwt) with and without currents included.

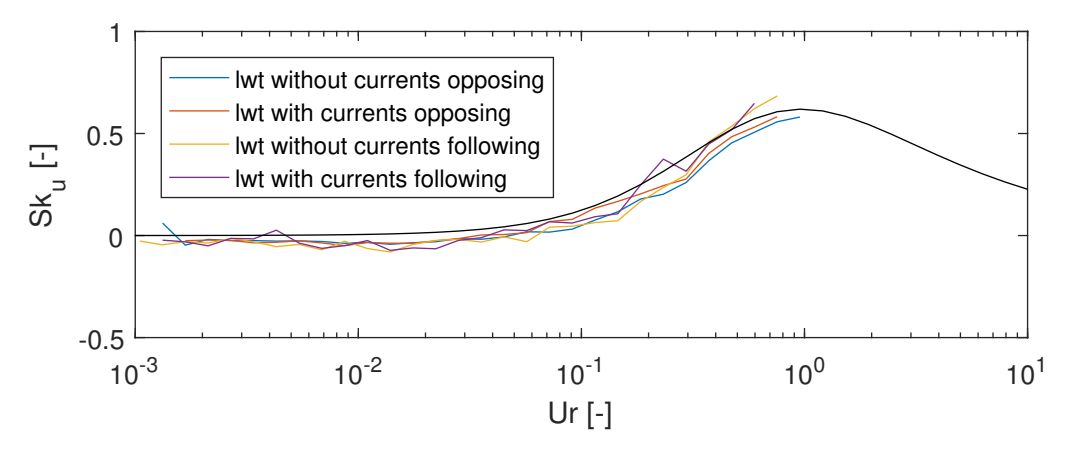


Figure E.18: Velocity skewness for opposing and following flow. Ursell number calculated with linear wave theory (lwt) with and without currents included